河北工業大学
HEBEI UNIVERSITY OF TECHNOLOGY

博士学位论文
DOCTORAL DISSERTATION

学　　院：电气工程学院
学科专业：电气工程
论文作者：Cyprien NSENGIMANA
指导教师：李玲玲　教授

河北工业大学研究生院　　2024 年　06 月

编号： 201840000004

河北工业大学博士学位论文
DOCTORAL DISSERTATION OF HEBEI UNIVERSITY OF TECHNOLOGY

论文题目

Research on Power system dispatching and operation optimization including distributed power sources

论文作者:	Nsengimana Cyprien	学生类别：	全日制
学科门类：	工学	学科专业：	Electrical Engineering
指导教师：	李玲玲	职称:	教授

2024年06月

资助基金项目： 河北省自然科学基金（E2018202282）
天津市自然科学基金重点项目（19JCZDJC32100）
Funds: Natural Science Foundation of Hebei Province (E2018202282)
and the key project of Tianjin Natural Science Foundation (19JCZDJC32100).

Dissertation Submitted to
Hebei University of Technology
for
The Doctor Degree of Electrical Engineering

Power system dispatching and operation optimization including distributed power sources

By
NSENGIMANA Cyprien

Supervisor: Prof. Li Lingling

June, 2024

This work was supported by the Natural Science Foundation of Hebei Province (E2018202282) and the key project of Tianjin Natural Science Foundation (19JCZDJC32100).

原创性声明

本人郑重声明：所呈交的学位论文，是本人在导师指导下，进行研究工作所取得的成果。除文中已经注明引用的内容外，本学位论文不包含任何他人或集体已经发表的作品内容，也不包含本人为获得其他学位而使用过的材料。对本论文所涉及的研究工作做出贡献的其他个人或集体，均已在文中以明确方式标明。本学位论文原创性声明的法律责任由本人承担。

学位论文作者签名： 日期：2024.06.12

关于学位论文版权使用授权的说明

本人完全了解河北工业大学关于收集、保存、使用学位论文的以下规定：学校有权采用影印、缩印、扫描、数字化或其它手段保存论文；学校有权提供本学位论文全文或者部分内容的阅览服务；学校有权将学位论文的全部或部分内容编入有关数据库进行检索、交流；学校有权向国家有关部门或者机构送交论文的复印件和电子版。

（保密的学位论文在解密后适用本授权说明）

学位论文作者签名： 日期：2024.06.12

导师签名：李玲玲 日期：2024.06.12

博士毕业论文答辩委员会决议书

论文题目	Power system dispatching and operation optimization including distribution power sources

决议书内容（就基础知识、创新性及论文价值、科研能力、写作规范性及答辩情况等做出评价）（600字以内）

该论文以含分布式电源的配电网系统为研究对象，从模型构建和算法求解两方面展开了研究。选题具有较重要的理论意义和应用价值。论文主要研究工作如下：

（1）设计了基于混合策略的多目标萤火虫算法（MOFSA），引入了三阶混沌映射策略和非线性种群比例递减因子来提高算法的有效性；

（2）基于静态重构和无功补偿两种优化方法，构建了含分布式电源电力系统的静态综合优化模型，提高了系统的能效和电能质量。

（3）给出了含分布式电源电力系统的一种动态综合优化方法，结合储能协调、动态重构和无功补偿，实现了系统经济效益、能源效率和电能质量均衡优化。

论文写作结构合理，层次清楚，内容详实，符合学位论文写作规范。学生在答辩过程条理清晰，回答问题正确，较好掌握了本学科的基础理论知识，具有从事科学研究和承担专业技术工作的能力。

综上，答辩委员会认为这是一篇 合格 水平的博士毕业论文。

答辩委员会主席签字：

答辩委员会委员签字：

2024 年 6月 8 日

摘要

随着能源短缺和环境污染问题的日益严重，以风电、光伏为代表的分布式电源受到广泛关注。然而分布式电源的接入电网改变了配电网原有的运行方式和系统结构，影响了电力系统运行的稳定性和经济性。因此，本论文以分布式电源系统为研究对象，利用风电功率预测，结合网络重构和无功补偿两种优化方法，从模型构建和算法求解等方面对含分布式电源的配电网运行进行优化研究，以改善含分布式电源系统的运行，实现含分布式电源的配电网运行优化，提高配电网的经济性、能源效率和电能质量。研究的具体内容和结果如下：

（1）针对含分布式电源的配电网运行优化模型求解问题，设计了基于混合策略的多目标萤火虫算法（MOFSA）。首先，在萤火虫算法的基础上，通过引入三阶混沌映射策略和非线性递减种群比例因子提高种群多样性，利用柯西变分策略和位置扰动策略提高算法跳出局部最优解的能力，再利用非支配排序机制和外部归档机制实现多目标优化，提出了 MOFSA 算法。其次，通过测试函数验证了算法的求解性能，结果表明，MOFSA 算法相比其他算法具有更好的收敛精度，且得到的解集分布更均匀。

（2）针对分布式电源电力系统的经济效益、能源效益和电能质量问题，结合静态重构和无功补偿两种优化方法，构建了分布式电源电力系统静态综合优化模型。首先，以电力系统经济成本、节点电压偏差和功率损耗最小化为目标，考虑电力系统运行约束，结合静态重构和无功补偿，建立了含分布式电源电力系统静态综合优化模型。其次，采用 MOFSA 算法对模型进行求解，基于理想解相似度排序技术选取最优折衷解。结果表明，与其他算法相比，MOFSA 算法得到的 Pareto 前沿覆盖范围更广、分布更均匀、完备程度更高，静态综合优化模型在保证系统经济性的同时，能够显著提高系统的能效和电能质量。

（3）针对考虑时段划分的含分布式电源电力系统动态综合优化问题，提出了一种基于欧氏距离的时段划分方法，并在静态综合优化模型的基础上构建了含分布式电源电力系统动态综合优化模型。首先，在静态综合优化模型的基础上，考虑开关动作次数约束和不同时段间的耦合性，结合动态重构和无功补偿两种优化方法，建立含分布式电源电力系统动态综合优化模型。其次，提出一种基于欧氏距离的时间段划分方法，对优化时间段进行动态划分。最后，采用 MOFSA 算法对考虑时段划分的动态综合优化模型进行求解，并在测试系统中验证了所提算法、模型及时段划分方法的有效性与先进性。结果表明：MOFSA 算法得到的优化方案比其他算法更具竞争力；动态综合优化模型能有效提高电力系统经济效率、能源效率和电能质量；采用所提时间划分方法动态划分优化时段，可显著减少开关操作次数 78.72%。算例分析验证了该模型的有效性。

关键词：分布式电源电力系统；网络重构；无功补偿；萤火虫算法；多目标优化

ABSTRACT

The increasing severity of energy shortage and environmental pollution issues has led to widespread attention being given to distributed power sources, such as wind and photovoltaic power. However, the integration of these sources into the grid has resulted in changes to the original operation mode and system structure of the distribution network, which has impacted the stability and economic efficiency of power system operation. This thesis has focused on distributed power systems as the subject of research. The wind and photovoltaic power predictions have been utilized as distributed power sources. Two optimization methods, network reconfiguration and reactive power compensation, have been combined and the operation of the distribution network with distributed power has been optimized from the perspectives of model construction and algorithm solving, with the aim of enhancing the performance of the distributed power system.

The operation optimization of distribution grids containing distributed power sources has been achieved, leading to improvements in the economic efficiency, energy efficiency, and power quality of these grids. The specific content and outcomes of the research are as follows:

(1) A multi-objective firefly algorithm (MOFSA) based on a hybrid strategy was designed to address the optimization model of the distribution network operation with distributed power sources. Initially, the MOFSA was proposed by incorporating a third-order chaotic mapping strategy and a nonlinear decreasing population proportion factor to enhance population diversity. It also utilized a Cauchy variation strategy and a positional perturbation strategy to improve the algorithm's ability to escape local optima. Subsequently, a non-dominated sorting mechanism and an external archiving mechanism were employed to achieve multi-objective optimization. The solution performance of the algorithm was then verified using test functions. The results demonstrated that the MOFSA algorithm had superior convergence accuracy to other tested algorithms, and the resulting solution set was more uniformly distributed.

（2） In response to the economic, energy, and power quality issues of power systems with distributed power supply, a static integrated optimization model for power systems with distributed power supply was constructed by combining static reconfiguration and reactive power compensation. The model was established with the objective of minimizing the economic cost of the power system, node voltage deviation, and power loss, while considering the operational constraints of the power system. The MOFSA algorithm was then used to solve the model, and the optimal compromise solution was selected based on the similarity ranking technique's ideal solution. The results indicated that the Pareto front obtained by the MOFSA algorithm had broader coverage, a more uniform distribution, and a higher degree of completeness compared to other algorithms. The static integrated optimization model was shown to significantly improve the energy efficiency and power quality of the system while ensuring its economic efficiency.

（3）For the dynamic integrated optimization problem of the power system with distributed power supply considering time slot division, a time slot division method based on Euclidean distance was proposed. A dynamic integrated optimization model of the power system with distributed power supply was constructed on the basis of the static integrated optimization model. The dynamic comprehensive optimization model was established by considering constraints on the number of switching actions and the coupling between different time sections, and by combining dynamic reconfiguration and reactive power compensation. A time period division method based on Euclidean distance was proposed to dynamically divide the optimization time periods. Finally, the MOFSA algorithm was used to solve the dynamic integrated optimization model with time slot division, and the effectiveness and advancement of the proposed algorithm on the model with the time slot division method were verified in the test system. The results confirmed that the optimization scheme obtained by the MOFSA algorithm was more competitive than other algorithms. The dynamic integrated optimization model was capable of effectively improving the economic efficiency, energy efficiency, and power quality of the power system. Additionally, the dynamic division of optimization periods using the proposed time division method significantly reduced the number of switching operations by 78.72%. Example analyses have verified the effectiveness of the proposed algorithm, model, and time slot division method, providing a reasonable optimization scheme for the operation optimization of power systems with distributed power sources.

Keywords: power system with distributed power sources; network reconfiguration; reactive power compensation; firefly algorithm; multi-objective optimisation

目 录

TABLE OF CONTENTS

List of Figures

List of Tables

List of Notes

$\mathbf{C_p}$:	power coefficient of wind turbine
$\mathbf{E_g}$:	band gap energy of the semiconductor material
$\mathbf{F_{Vdev}(t)}$:	node voltage deviation objective function
$\mathbf{G_{stc}}$:	irradiance under standard test condition
$\mathbf{I_{SC}}$:	Short circuit current of solar cell/ PV module
$\mathbf{I_m}$:	Module current
$\mathbf{I_{ph}}$:	current generated by the PV cell
$\mathbf{I_{s(stc)}}$:	nominal saturation current
$\mathbf{I_{sc(stc)}}$:	short circuit current per cell at stc conditions
$\mathbf{N_n}$:	total number of nodes
$\mathbf{P_m}$:	Power of module
$\mathbf{P_w(t)}$:	output power of wind turbine
$\mathbf{T_{amb}}$:	air temperature of the location
$\mathbf{T_{ax}}$:	axial wind thrust
$\mathbf{T_{stc}}$:	Temperature of the cell at stc $\mathrm{T_{stc}} = 25℃$
$\mathbf{V_{OC}}$:	open circuit of PV cell or module
$\mathbf{V_{i,t}}$:	Voltage magnitude at node (i) in period(t)
$\mathbf{V_m}$:	Module voltage
$\mathbf{V_r}$:	reference voltage
$\mathbf{p_i}$:	incoming wind pressure
$\mathbf{p_r}$:	wind pressure at rotor position know as a rated wind power
$\mathbf{p_{rf}}$:	Outgoing wind pressure just after the rotor
$\mathbf{v_w}$:	wind turbine speed
$\mathbf{v_{wf}(t)}$:	downstream wind velocity
$\mathbf{v_{wi}(t)}$:	upstream wind velocity
$\boldsymbol{N_p}$:	Number of parallel cells in a PV module
$\boldsymbol{N_s}$:	Number of cells in series in a PV module
$\boldsymbol{P_{pv}^a}$:	actual power generation of the PV power station
$\boldsymbol{P_{pv}^r}$:	rated power of the PV power generator
$\boldsymbol{V_{dev}^t}$:	node voltage deviation
$\boldsymbol{f_{cost}}$:	Objective function for economic cost
$\boldsymbol{f_{dev}}$:	Objective function for node voltage deviation
$\boldsymbol{k_{pv}^h}$:	penalty coefficient for overestimating the output of PV power.
$\boldsymbol{p_{DG}}$:	Active output power of DGs
$\boldsymbol{p_{load}}$:	active power demand of the load
$\boldsymbol{q_{DG}}$:	reactive output power of DGs
$\boldsymbol{q_{loss}}$:	Reactive power demand of the load
$\boldsymbol{\rho_w}$:	air density in the wind turbine location
A:	swept area of the wind turbine
AI:	Artificial intelligence
AMI:	Advanced metering infrastructure
BPNN:	Backpropagation Neural Network algorithm
DERs:	Distributed energy resources
DG:	Distributed Generator
DKASC:	Desert Knowledge Australia Solar Center
ELM:	Extreme learning machine algorithm
FA:	Firefly algorithm
FOA:	Fruit Fly Optimization Algorithm
G:	is the surface irradiance of the cell under general conditions($\mathrm{W/m^2}$)
GASVR:	Genetic Algorithm Support Vector Regression
HV:	hypervolume
I:	output current of the PV cell

IEEE-33/69	IEEE33/69-bus system, a standard test feeder
IGD:	Inverted Generational Distance
MOFSVR:	Multi-objective Firefly optimized by support vector regression
JSSVR:	Jellyfish search support vector regression
K	Kelvin Temperature or absolute temperature.
MAE:	Mean Absolute Error
MAPE:	Mean Absolute Percentage Error
MaxGen:	Maximum iterations
MOFSA:	Multi-Objective Firefly Algorithm based on hybrid strategy
MOMVO:	Multi-objective Multi-verse Optimizer
MOPSO:	Multi-objective Particle Swarm Optimization
MSE:	Mean Squared Error
NOCT:	Nominal Operating Cell Temperature (800 W/m^2 irradiance and 20℃)
NSGA-II:	Non-dominated Sorting Genetic Algorithm with Elite Strategy-II
NSMFO:	Non-dominated Sorting Moth Flame Optimizer
P:	Active power
PSOSVR:	Particle Swarm Optimization SVR.
PV:	Photovoltaic power
Q:	Reactive power
R^2:	Resolvability Coefficient
RMSE:	Root Mean Square Error
S:	switches
SC:	Parallel connected (shunt) capacitor banks
SCADA:	Supervisory Control and Data Acquisition
SP:	Spacing evaluation
STATCOMs:	Static Synchronous Compensators
SVR:	Support vector regression
V:	output voltage of the PV cell
VAR:	Volt-Ampere Reactive compensator
WOASVR:	Whale Optimization Algorithm SVR
WT:	Wind turbine power
Z:	set of optimization variables: S, SVC, and SC
Stc:	standard test condition
***k*:**	Boltzmann’s constant (1.380649×10^{-2} J/K)

Chapter 1 Introduction

1.1 Research background and significance of the study

Power dispatching and operation optimization, with a focus on distributed power sources, is a critical research area aiming to enhance the efficiency, reliability, and sustainability of electrical grids.

1.1.1 Research background

This field addresses the challenges posed by the integration of diverse energy resources, such as renewable energy, storage systems, and distributed generators[1].

Researchers explore advanced algorithms, control strategies, and decision-making tools to optimize the dispatch of power generation, considering factors like load demand, network constraints, and environmental impact[2][3][4]. The goal is to achieve economic operation while ensuring grid stability and minimizing environmental impact. Key aspects include demand response, grid flexibility, and the incorporation of smart grid technologies. The integration of distributed energy resources introduces complexities that require innovative solutions to balance supply and demand dynamically[5][6]. Researchers also leverage optimization techniques, artificial intelligence, and data analytics to develop real-time decision support systems for power system operators.

1.1.2 Research significance

The integration of renewable energy sources is considered of paramount importance by researchers, aiming to enhance the sustainability and efficiency of distribution network operations. This initiative seeks to address the environmental impact of traditional energy sources and mitigate the challenges associated with their intermittency[7]. By incorporating renewable sources such as solar and wind power, the energy landscape becomes more diverse and resilient[8]. Advanced technologies, including artificial intelligence, play a pivotal role in optimizing the integration of renewables, enabling predictive maintenance, efficient energy storage, and smart grid management[9]. This paradigm shift not only fosters environmental sustainability but also contributes to the economic viability of energy systems by reducing reliance on finite resources and promoting a more balanced and stable distribution network[10].

Research in economic power distribution network, with a focus on optimization and the integration of distributed energy sources, brings about a more efficient, reliable, and sustainable energy infrastructure[10]. It encompasses economic, environmental, and technological considerations, paving the way for a smarter and greener future in the energy sector. Indeed, power system dispatching optimization enhances the efficiency of energy utilization. This is done by strategically managing the distribution of power from various sources whereby power system is operated to minimize the energy losses, reduce fuel consumption, and overall improves operational efficiency.

The research study is focusing on seamlessly integrating renewable energy sources, such as wind and solar, into the power grid. Dispatch optimization accounts for the intermittent nature of these sources, ensuring their effective utilization and contribution to the overall grid without compromising the overall reliability of the system[11]. To ensure the grid resilience and reliability of the system, both terms are crucial for maintaining a stable and secure power supply, especially in the face of challenges such as extreme weather events, equipment failures, or other unforeseen circumstances in distribution placements[12][13]. Robust planning, efficient operational strategies, and the integration of advanced technologies contribute to enhancing both resilience and reliability in power systems.

The research study is also taking consideration economic factors while implementing the optimization algorithms. The results consider both short-term and long-term economic implications, aiming to minimize operational costs, investment costs, and overall expenses associated with power system operation[11]. Research in power system optimization not only fosters environmental sustainability through the integration of renewable energy sources, reducing greenhouse gas emissions, but also propels smart grid development. By leveraging advanced technologies and communication systems, smart grids enhance efficiency, adaptability, and overall environmental responsibility in the power sector, contributing to a greener and more intelligent energy infrastructure. The pursuit of optimized power system dispatching drives technological innovation whereby researchers explore and develop advanced algorithms, machine learning techniques, and control strategies to address the evolving dynamics of power systems, especially with the integration of distributed energy resources. This innovation contributes to the ongoing transformation of the energy landscape. The energy landscape in a power system refers to the overall structure and dynamics of the sources, generation technologies, and distribution networks that collectively provide electrical power to consumers. This landscape has been undergoing significant transformations driven by technological advancements, environmental concerns, and changing of world’s economic factors.

1.2 Current trends in distributed power optimization

Distributed power in power system network reconstruction typically involves the integration of decentralized or distributed energy resources (DERs) into the existing power grid. The process includes renewable energy sources, energy storage systems, and other small-scale power generation units.

1.2.1 Progress in distributed power for network reconstruction

The goal is often to enhance the reliability, efficiency, and resilience of the power system. Researchers are often focusing on the challenges and opportunities associated with integrating DERs, such as solar panels, wind turbines, and energy storage, into the power grid to make the smart grid network. To achieve their target, smart grid technologies are playing a crucial role in managing the distributed power. To explore the efficiency of smart grid operation they use the advanced metering infrastructure (AMI), communication systems, and control algorithms. A significant focus lies on decentralized control and optimization strategies to coordinate and manage the diverse DERs efficiently. Simultaneously, resilience and reliability studies investigate the system's ability to withstand disruptions, ensuring continuous operation even in the presence of uncertainties and disturbances[14].

This holistic approach aims to enhance the overall reliability, efficiency, and resilience of power systems in the face of evolving energy landscapes. This strategy considers the power system in its entirety rather than focusing on individual components in isolation. It involves integrating various elements such as energy production, distribution, storage, and consumption, alongside considering environmental impacts, technological advancements, and socio-economic factors. The goal is to ensure that decisions and improvements in one area do not adversely affect others and that the system operates optimally on all fronts.

1.2.2 Research status of power system reactive power compensation optimization

Reactive power compensation is crucial in power systems in terms of maintaining voltage stability, improving the power factor of the system, and enhancing the overall system efficiency[15]. Optimization of reactive power compensation involves determining the optimal locations, sizing, and control strategies for reactive power devices such as capacitors and reactors[16]. To pin point to the target, researchers are employing various optimization techniques, including mathematical programming, artificial intelligence (AI), and heuristic algorithms, to find the optimal settings for reactive power compensation devices[17].

AI methods such as genetic algorithms, particle swarm optimization, and machine learning are increasingly being applied for their ability to handle complex, nonlinear power system models[18].With the increasing integration of renewable energy sources like wind and solar, reactive power compensation becomes crucial for maintaining voltage stability and addressing the intermittent nature of these sources[19].

Research study is also focusing on incorporating smart grid technologies, such as advanced sensors, communication systems, and control algorithms, to enhance the efficiency and responsiveness of reactive power compensation. In order to meet the challenges, researchers study the dynamic nature of power systems and work on the possible uncertainties in the load demand, and the evolving nature of grid configurations by providing the robust optimization techniques to address these challenges for reactive power compensation[20].

1.2.3 Research status of wind and photovoltaic power generation and power prediction

The current state of research in wind and photovoltaic power generation reflects a multifaceted approach aimed at optimizing efficiency, reliability, and grid integration. For wind power, ongoing investigations are directed towards the development of advanced materials for turbine blades, improved aerodynamic designs, and innovative control strategies[21]. Concurrently, research in photovoltaics emphasizes the exploration of novel materials, such as perovskite-based solar cells, and the enhancement of PV system architectures to boost overall energy conversion efficiency[22].

Efforts to tackle the intermittent nature of renewable energy sources have led to increased focus on energy storage solutions. This includes the investigation of advanced battery technologies and the development of smart grid systems to efficiently manage the variable output from wind and solar installations. Grid integration studies are exploring ways to seamlessly incorporate large-scale wind and PV systems into existing power infrastructures, ensuring stability and reliability.

Power prediction remains a critical aspect of renewable energy research, particularly for wind and solar sources. Researchers are deploying advanced machine learning techniques, such as artificial neural networks and data-driven algorithms, to improve the accuracy of forecasting models[23]. These models enable better anticipation of energy production patterns, aiding grid operators in managing the variability associated with renewable sources.

1.2.4 Research status on integration of power system network reconstruction and economic reactive power compensation.

The integration of power system network reconstruction and economic reactive power compensation is a critical area of research aimed at enhancing the efficiency and reliability of electrical grids. Network reconstruction involves the identification and modeling of power system components, such as generators, transformers, and transmission lines, to accurately represent the system's topology[24]. Reactive power compensation optimization focuses on improving voltage stability and minimizing power losses by strategically placing reactive power devices like capacitors and reactors.

Researchers have made significant strides in developing algorithms and methodologies for simultaneous network reconstruction and economic reactive power optimization. Advanced optimization techniques, including metaheuristic algorithms and artificial intelligence approaches, have been applied to address the complexity of large-scale power systems. The integration of real-time data, such as synchro-phasor measurements and SCADA information, enhances the accuracy of the reconstruction and optimization processes[25].

Moreover, the research emphasizes the importance of considering uncertainties and dynamic conditions in power systems, such as variations in demand and renewable energy sources. The goal is to design resilient and adaptive strategies that can respond to changing operating conditions. Integration of these approaches aids in maintaining optimal voltage levels, reducing power losses, and ensuring the overall stability of the power grid[26].

Despite progress, challenges remain, including the need for standardized frameworks, scalability, and the incorporation of cybersecurity measures to protect the integrity of the reconstructed network. Interdisciplinary collaboration between power system engineers, computer scientists, and control theorists is crucial for advancing this field[25].

1.2.5 Research status of wind and solar energy power systems with contribution of energy storage

Research on wind and solar energy power systems, coupled with energy storage, has gained significant traction in recent years. The integration of wind and solar into the power grid are posing challenges due to their intermittent nature[27]. Both energy sources are characterized by their variability, signifying the fluctuations and irregularities in their power generation based on changing weather conditions and environmental factors[28]. Energy storage systems, such as batteries and pumped hydro storage, play a crucial role in addressing these challenges by storing excess energy during periods of high generation and releasing it when demand is high or generation is low[2][29][30].

Studies focus on enhancing the reliability and efficiency of wind and solar power systems through advanced control algorithms, forecasting techniques, and optimized energy management strategies[31][32]. Additionally, research explores the techno-economic aspects of energy storage integration, evaluating the cost-effectiveness and environmental impact[30][33]. The synergistic combination of wind and solar with energy storage is seen as a key solution for achieving a more sustainable and resilient power infrastructure[34]. Researchers are also investigating new materials and technologies for energy storage devices to improve their performance, durability, and environmental sustainability[16]. Challenges remain, such as the need for standardization, policy support, and improved grid management tools. Interdisciplinary approaches involving engineering, economics, and policy analysis are essential to address these challenges and facilitate the widespread adoption of renewable energy systems with energy storage[35].

Thesis structure and research

In the context of sustainable development, distributed power sources, such as wind power and photovoltaic, have been connected to the grid on a large scale. This connection has altered the original mode of operation and system structure of the power system, posing significant challenges to its stable and economic operation. Network reconfiguration and reactive power compensation, as two optimization methods for power system operation, have been implemented to improve the system's performance. However, the individual impact of each optimization method on enhancing power system operation is limited. This thesis integrates the two optimization methods of network reconfiguration and reactive power compensation to construct a power system operation optimization model and algorithm solution for systems with distributed power supply. The main research content is detailed as follows:

Chapter 1 was written to describe the background and significance of studying power system operation optimization with distributed power supply. It discussed the current status of power system network reconfiguration and reactive power optimization, summarized the current state of research on comprehensive optimization combining network reconfiguration and reactive power compensation, and concluded with a summary of the main research content of the thesis.

A mathematical model of distributed power supply was established in Chapter 2, with simulation analysis conducted in a test system to analyze the impact of distributed power supply grid connection on power system operation. This analysis considered grid connection type and capacity and verified the validity of the forward back generation method. The modeling and grid-connected analysis of Chapter 2 laid the research foundation for the comprehensive optimization of power systems containing distributed power in Chapters 4 and 5.

Chapter 3 proposed a Multi-Objective Firefly Algorithm based on a hybrid strategy (MOFSA). It introduced a non-linear decreasing population proportion factor, third-order chaotic mapping strategy, Cauchy variation strategy, and positional perturbation strategy into the firefly search algorithm to enhance its optimization capability. Additionally, a non-dominated sorting mechanism and external archiving mechanism were adopted to achieve multi-objective optimization. The MOFSA algorithm was then compared with other optimization algorithms, and its solution performance was verified using test functions. Chapter 3 provided a high-performance solution algorithm for solving the integrated static and dynamic optimization model of power systems containing distributed power sources in Chapters 5 and 6.

The proposed MOFSVR model in Chapter 4 investigated photovoltaic power (PV) and wind power (WT) prediction. The effectiveness of the model's predictions was verified using seven comparative prediction models with four evaluation metrics. The chapter detailed the sources of data used in the study, the preprocessing methodology, and performed PV power prediction under various weather conditions and wind power prediction across different seasons.

A static integrated optimization model for distributed power systems containing distributed power sources was established in Chapter 5. This model aimed to minimize system economic cost, node voltage deviation, and power loss, combining static reconfiguration and reactive power compensation as optimization methods. The MOFSA algorithm, introduced in Chapter 3, was utilized to solve the static integrated optimization model, with the optimal compromise solution selected using the ideal solution and similarity ranking technique. The effectiveness of the MOFSA algorithm was verified by comparing it with other multi-objective optimization algorithms, and the validity of the constructed model was confirmed in a designed comparison scenario. The static integrated optimization model of Chapter 5 served as the basis for constructing the dynamic integrated optimization model in Chapter 6.

Chapter 6 established a dynamic integrated optimization model for distributed power systems, taking into account the constraints of the number of switching actions and the coupling between different time sections based on the static model from Chapter 5. It combined dynamic reconfiguration and reactive power compensation as optimization modes. The MOFSA algorithm was used to solve the dynamic comprehensive optimization model considering time division, and its effectiveness and advancement were verified by comparing it with other algorithms. The effectiveness of the proposed time slot division method and the constructed model were verified in the test system through a designed comparison model and scenario.

Chapter 7 summarized the main research work of the dissertation, highlighted the important conclusions, and provided an outlook on future research directions.

Chapter 2 Impact of distributed power sources on the power system network

2.1 Introduction

A wind turbine is a device that converts the kinetic energy of the wind into mechanical energy, which can then be used to generate electricity. Wind turbines are a type of renewable energy technology and play a significant role in harnessing wind power for electricity generation. The basic overview of the process of wind power generation is summarized as follows: The process starts from the wind captivity where the turbines consisting of blades attached to a rotor. When the wind blows, the propeller blades capture the kinetic energy from the moving air which then causes the rotor to spin. This rotational motion is a result of the pressure difference on the windward and leeward sides of the blades. The rotating rotor is connected to a generator housed in the nacelle. As the rotor turns, it drives the generator, converting mechanical energy into electrical energy through electromagnetic induction. The generator produces alternating current electricity. This electrical energy is then transmitted through cables down the tower.

2.1.1 Distributed power from the wind output model

The electricity generated by the wind turbine is typically fed into the power grid[3][36]-[42]. It becomes part of the overall electrical supply and can be distributed for various uses. To increase the wind power output generation, there are keys factors to consider such as wind speed, site selection, turbine size, and proper maintenance.

The relationship between the output power of a wind turbine and the wind speed is typically described by the power curve as shown in Figure 2.1. The power curve illustrates how the electrical power output of a wind turbine varies with different wind speeds. The output power of wind turbine $P_w(t)$ is given below.

$$P_w(t) = \frac{C_{p*}\rho_w * A * v_w(t)^3}{2} \tag{2.1}$$

Where C_p is the power coefficient, a dimensionless parameter that represents the efficiency of the wind turbine in converting the kinetic energy of the wind into electrical power. C_p is determined by the upstream wind velocity $v_{wi}(t)$ and down stream velocity $v_{wf}(t)$. When $\frac{v_{wi}(t)}{v_{wf}(t)} = \frac{1}{3}$.This stream-tube expansion shows that C_p has a physical limit called Betz limit such that $C_p \leq 16/27 \approx 0.593$ Regardless of its design, a wind turbine can thus extract at most 59.3% of the wind energy[43][44][45]. The blades of wind turbine can be adjusted to a proper angle to achieve the maximum power output at different wind speeds[46]. ρ_w represents the wind air density in the wind turbine location; A is the swept area of the wind turbine; v_w is the wind turbine speed.

It noted the large turbines will sweep more area and resulting in more wind energy. The high wind speed with the optimal site location will contribute to the increased power output. The wind velocity is an important parameter and significantly influences the power per unit area available from the wind[3][47][48]-[50]. Short-term variations in wind direction and the associated motion affect the fatigue life of components such as blades and yaw drives.

The equation (2.1) reveals the following three points in wind power energy generation.

(i) The wind power density is proportional to the density of the air. For standard conditions (At sea level i.e. at 15°C, the density of uniform air is 1.225kg/m^3[51].

(ii) Power from the wind is proportional to the area swept by the rotor or the rotor diameter squared for a conventional horizontal axis wind machine.

(iii)The wind power density is proportional to the cube of the wind velocity. This mean that if the wind speed doubles, the wind energy will increase eight times.

2.1.2 Derivation of wind power coefficient

We consider a rotor which does not possess a hub, in a steady and uniform wind field and assume the rotor extracts a fraction of the extreme kinetic energy from the wind. The downstream wind speed will be smaller than the upstream wind speed ($v_{wf}<v_{wi}$). Thus, according to the conservation of mass[45], the cross-section area of the upstream should be smaller than the downstream ($A_i < A_f$). A control surface corresponding to a set of streamlines bounds a controlled volume and there is no flow crossing the surface. The air is assumed to be non-compressible and the density remains constant, and there is no heat transfer. The volumetric flow rate, Q, is given.

$$Q = v_{wi}A_i = v_{wf}A_f = v_wA \tag{2.2}$$

Where v_{wi} is the wind speed in the front of the rotor, v_{wf} is the wind speed downstream of the rotor and v_w is the wind speed by the rotor, A_i and A_f are the area of the wind before and after reaching the rotor while A is the area at the rotor.

Applying Bernoulli's equation separately before and after the rotor position, since it can be applied exactly on the rotor position due to energy losses, we get the following:

The incoming wind pressure from P_i to the wind pressure at rotor position P_r are the important parameters before the rotor. After the rotor, the wind pressure P_{rf} to P_f where $P_f = P_i$ give us the following identity.

$$\frac{P_i}{\rho}+\frac{1}{2}{v_{wi}}^2=\frac{P_r}{\rho}+\frac{1}{2}{v_w}^2 \tag{2.3}$$

This is the equation before the rotor position. After the rotor position, it comes the following equation,

$$\frac{P_{rf}}{\rho}+\frac{1}{2}{v_w}^2=\frac{P_i}{\rho}+\frac{1}{2}{v_{wf}}^2 \tag{2.4}$$

The pressure drop by the rotor can be expressed by:

$$\frac{P_r}{\rho}-\frac{P_{rf}}{\rho}=\left(\frac{P_i}{\rho}+\frac{1}{2}{v_{wi}}^2\right)-\left(\frac{P_i}{\rho}+\frac{1}{2}{v_{wf}}^2\right) \tag{2.5}$$

Where we assume $P_i=P_o$;

$$P_r-P_{rf}=\frac{1}{2}\rho({v_{wi}}^2-{v_{wf}}^2) \tag{2.6}$$

The pressure drop induced by the rotor is directly proportional to the axial thrust (T_a) exerted by the flow on the rotor and is equal to the deficit in the momentum flux from the upstream to the downstream area.

$$T_a=\frac{1}{2}A\rho({v_{wi}}^2-{v_{wf}}^2)=\rho Q(v_{wi}-v_{wf}) \tag{2.7}$$

The wind speed by the rotor is the average of the upstream and the downstream velocities, given as:

$$v_w=\frac{1}{2}(v_{wi}+v_{wf}) \tag{2.8}$$

Now consider the kinetic power extracted by the turbine. It is the kinetic energy difference between the upstream and the downstream. Kinetic power at one location can be expressed as,

$$E=\frac{1}{2}Q\rho{v_w}^2=\frac{1}{2}\rho A{v_w}^3 \tag{2.9}$$

Power extracted by the rotor will be given by the following expression

$$\Delta E=\frac{1}{2}\rho Q({v_{wi}}^2-{v_{wf}}^2)=\frac{1}{2}\rho A v_w({v_{wi}}^2-{v_{wf}}^2) \tag{2.10}$$

To calculate the turbine efficiency, Betz suggests to divide the power extracted at the rotor by a reference power. The power coefficient (Cp) is the ratio of the power generated by turbine over the reference power. The reference power is the power of air upstream moving at v_{wi} contained in a cylinder with the area of the rotor (A).

$$C_p=\frac{\Delta E}{E_{ref}}=\frac{\Delta E}{\frac{1}{2}\rho A({v_{wi}}^3)} \tag{2.11}$$

Because C_p only depends on the upstream (v_{wi}) and the downstream (v_{wf}) velocities, the power coefficient (C_p) can now be written as:

$$C_p=\frac{\frac{1}{2}\rho A v_w({v_{wi}}^2-{v_{wf}}^2)}{\frac{1}{2}\rho A {v_w}^3} \tag{2.12}$$

$$C_p=\frac{\frac{1}{2}\rho A(\frac{1}{2})(v_{wi}+v_{wf})({v_{wi}}^2-{v_{wf}}^2)}{\frac{1}{2}\rho A {v_{wi}}^3} \tag{2.13}$$

Substituting $\alpha=\frac{v_{wf}}{v_{wi}}$ (2.14)

$$C_p = \frac{1}{2}(1+\alpha)(1-\alpha^2) \tag{2.15}$$

$$\text{Where } \alpha_{max} = \frac{1}{3} \ and \ C_{pmax} = \frac{16}{27} = 0.5926 \tag{2.16}$$

The peak power that could be extracted from a wind stream is given by:

$$P_p = \Delta E = C_p \frac{1}{2}\rho A({v_{wi}}^3) \tag{2.17}$$

$$P_p = \Delta E = (\frac{16}{27})(\frac{1}{2})\rho A({v_{wi}}^3) \tag{2.18}$$

Equation (2.16) demonstrates that the power coefficient reaches a maximum value of 0.5926 when α is equal to one third. This is referred to be as the Betz's Limit. This theoretical value means that no turbine can capture more than $\frac{16}{27}$ of the kinetic energy of the upstream wind when the outlet velocity is equal to one-third the wind speed[52][53][54]. In practical applications, the power coefficients (Cp) of modern wind turbines typically reach peaks ranging from 0.45 to 0.50. This represents approximately 75% to 85% of the theoretical maximum. However, the overall efficiency of the wind turbine system is considerably lower, with only 10% – 30% of wind power effectively converted into usable energy. This reduced efficiency is attributed to various inefficiencies within the entire wind turbine system, including aspects like the generator, blade surface roughness, power transmission, gearbox, bearings and mechanical flaws[55].

The wind turbine output relationship used in actual wind turbine power generation research is different from the above equation. When modeling the wind farm output directly with wind speed, a linear relationship is observed between wind power and wind speed within a specific range. The specific curve illustrating the wind turbine output relationship is presented in Figure 2.1.

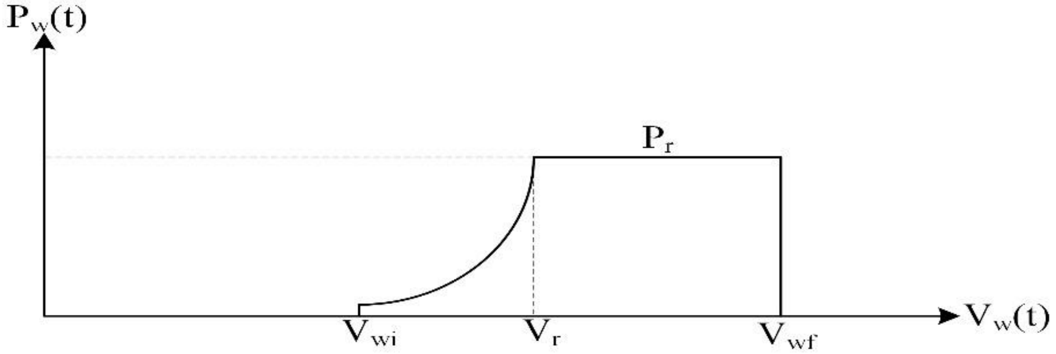

图 2.1 风力涡轮机的输出功率

Figure 2.1 Power output of wind turbine

The relationship between wind power output and wind velocity in Figure 2.1 as were described in[2][56],is given by the following equation :

$$P_w(t)=\begin{cases}0 & v_w(t)<v_{wi}\\ \frac{v_w(t)-v_{wi}}{v_r-v_{wi}}P_r & v_{wi}\le v_w(t)<v_r\\ P_r & v_r\le v_w(t)<v_{wf}\\ 0 & v_w(t)>v_{wf}\end{cases} \tag{2.19}$$

Where $v_w(\mathrm{t})$ is the average wind speed at time t; v_{wi} is the cut-in wind speed of the wind turbine; v_r is the rated wind speed of the fan; P_r is the rated output of the wind turbine. To ensure the safety of the device, the wind turbine stops producing power when the wind speed at time t is either more than the cut-out wind speed or less than the cut-in wind speed. The wind turbine will only produce power in accordance with the wind turbine output formula when the wind speed is between the wind turbine's cut-in and cut-out wind speeds.

2.1.3 Construction of photovoltaic power station output model

The output of a photovoltaic (PV) power station, which generates electricity from sunlight using solar panels, is influenced by various factors. The following are the key factors that affect the performance of a PV power generation system in power system energy generation. These include solar irradiance level, where the amount of sunlight (solar irradiance) reaching the solar panels is a major critical factor affecting the PV power generation directly. The severity of solar irradiance on solar panel depends on geographic location, time of day, and weather conditions. Cloud cover, shading, and atmospheric conditions can also affect the intensity of sunlight. Other important factor includes Temperature of the solar panels. It also affects solar panel’s efficiency. Higher temperatures can lead to a decrease in the efficiency of solar cells. Most solar panels perform best at moderate temperatures. There are none negligeable impacts due to angle and orientation of the panels, dust, dirtiness, shading and inverter efficiency. They need to be handled properly in order to contribute to the efficacity and performance of the photovoltaic power generation system.

In this instance, to maximize the harnessing of solar energy resources, it is essential to forecast the precise rate of photovoltaic power generation. Accurately predicting this power value can significantly enhance the efficiency of utilizing photovoltaic resources. To address the unpredictable nature of solar radiation, the probability density function is employed. Photovoltaic power generation devices are composed of many photovoltaic power generation units of the same type. The equivalent circuit diagram of a single photovoltaic unit is as follows in Figure 2.2:

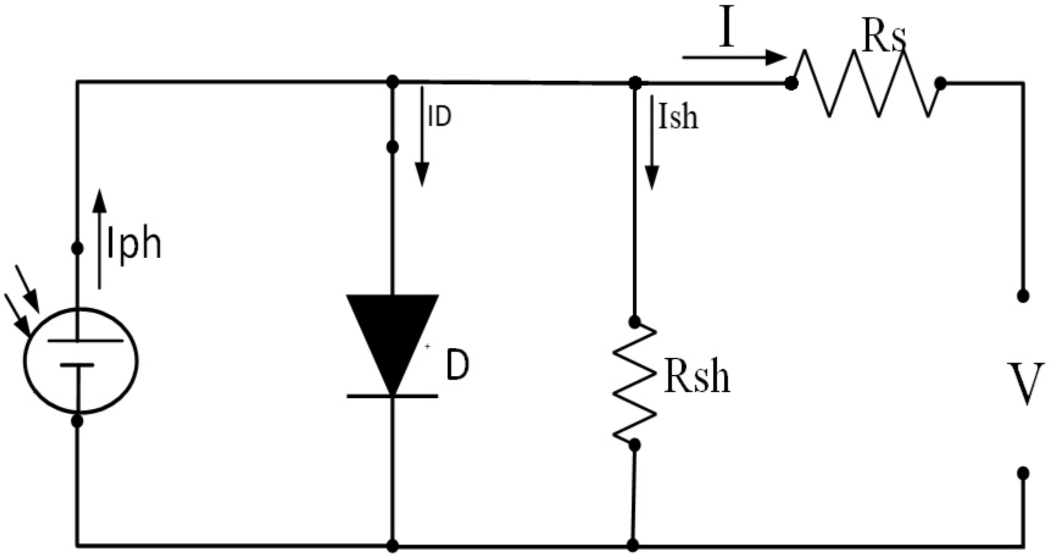

图 2.2 太阳能电池的等效电路

Figure 2.2 Equivalent circuit of solar cell

In Figure 2.2, I_{ph} is the current generated by the PV cell, I and V are the output current and voltage of the PV cell. Using Kirchoff's current law and replacing I_D and I_{sh} by their respective equivalent equations, it is possible to compute the PV cell current (I) as follows:

$$I = I_{ph} - I_D - I_{sh} \tag{2.20}$$

$$I = I_{ph} - I_s\left[e\left(\frac{q(V+IR_S)}{nkT_{cell}}\right) - 1\right] - [\frac{V+IR_S}{R_{Sh}}] \tag{2.21}$$

Where the following equations are summed up concerning whether they are entering or leaving a common node in the circuit diagram of Figure 2.1. The photocurrent I_{ph} is proportional to the incident flux and independent of V (or Rs). I_{ph} is linearly dependent on the solar radiation and is influenced by the outdoor temperature as described in equation (2.22). K_{isc} (A/°C) is the temperature coefficient of the cell's short circuit current and is given by solar PV manufacturer and the naturally occurring unit of electric charge is q of 1.602 E^{-19} Coulomb.

$$I_{ph} = \frac{G}{G_{stc}}[I_{sc(stc)} + K_{isc}(T_{cell} - T_{stc})] \tag{2.22}$$

$$I_d = I_s\, e\left(\frac{q(V+IR_S)}{nkT_{cell}}\right) - 1 \tag{2.23}$$

$$I_{Rsh} = \frac{V+IR_S}{R_{Sh}} \tag{2.24}$$

The summary of mathematical equations of solar Photovoltaic cell or PV module design is given below[43][57].The open circuit of PV module is herewith derived as follows:

$$V_{OC} = V_{OC(stc)} + K_{voc} * (T_{cell} - T_{stc}) \tag{2.25}$$

$$I_s = I_{s(stc)} * \left(\frac{T_{cell}}{T_{stc}}\right)^3 * e^{-\left(\frac{qE_g}{nk}\right)\left(\frac{1}{T_{cell}}-\frac{1}{T_{stc}}\right)} \tag{2.26}$$

$$I_{s(stc)} = \frac{I_{sc(stc)}}{e^{\left[\frac{qV_{oc(stc)}}{nkT_{stc}}\right]}-1} \tag{2.27}$$

Where E_g is the band gap energy of the semiconductor material used to make photovoltaic module; G is the surface irradiance of the cell under general conditions(W/m^2); G_{stc} is the irradiance under standard test conditions (G_{stc} = 1,000W/m^2); $I_{s(stc)}$ is the nominal saturation current; $I_{sc(stc)}$is the short circuit current per cell at T_{stc}; k is the Boltzmann's constant; K_{isc} is the temperature coefficient of short circuit current; K_{voc} is the temperature coefficient of open-circuit voltage;n is the diode ideality factor ; The standard test conditions($T_{stc} = 25$°C); T_{cell} is the cell absolute temperature in Kelvin and it may be given by the following relation when considering the nominal operating cell temperature. NOCT is the rate providing information about a module's temperature and gives a more precise estimate of PV power in the field on sunny days at solar noontime. NOCT refers to the expected temperature at which solar cells function under specific weather conditions and thus make it possible to accurately do better predictions of solar energy yield. It thus plays a crucial role in system sizing, designing and optimization of PV systems while maximizing energy production and its return on investment.

$$T_{cell} = T_{amb} + \frac{G}{800} * (NOCT - 20) \tag{2.28}$$

Where T_{amb} is the air temperature of the location, NOCT is provided by the solar PV manufacturer (°C) and is defined as the nominal operating condition of the solar cell at 800 W/m^2 irradiance and 20°C of air temperature[58]. The equation (2.28) highlights that the performance of PV module depends on both the solar irradiance at the site and the cell temperature.

In most PV uses, voltages and currents with higher values are needed at the scaled solar cell limited area. This brings us to scale up their magnitude produced by a PV generator with respect to the specific application. For this case, Solar cells are connected in series to increase the voltage and in parallel to match to load current in PV module. To form a PV module with many cells, the following equations holds:

$$I_m = N_p I \tag{2.29}$$

$$V_m = N_s V \tag{2.30}$$

$$P_m = N_s N_p V I \tag{2.31}$$

Every solar cell technology has a different temperature coefficient specified within module datasheet. The temperature coefficient is significant because it directly affects the power output of a solar panel. As the temperature of a solar module rises, its power output falls.

2.1.4 Temperature Coefficient of Solar Cells: Impact and Mitigation Strategies.

The temperature coefficient of solar cells plays a pivotal role in determining the efficiency and performance of photovoltaic systems. Due to the significance of temperature coefficients in solar cells and their impact on energy conversion process, manufacturers are notably indicating their parameters for each solar panel produced for both $\mathrm{I_{SC}}$ and $\mathrm{V_{OC}}$. The recent research studies and authoritative sources in the field have noted that solar cells are widely recognized as a sustainable and renewable energy source, contributing significantly to the global shift towards cleaner energy. However, the efficiency of solar cells is influenced by various factors, with temperature being a critical parameter. The temperature coefficient of solar cells measures how their performance is affected by changes in temperature, and understanding this phenomenon is a crucial for optimizing photovoltaic energy output[59].

The temperature coefficients of solar panels are parameters that describe how the performance of a solar panel changes with variations in temperature[39]. These are:

(1) Temperature Coefficient of Short Circuit Current (I_{SC})

This coefficient represents the percentage change in the short circuit current (I_{SC}) for a 1°C change in temperature. If the temperature increases, the short circuit current tends to increase, and vice versa. A substantial increase in solar irradiation has much influence on I_{SC} where a sudden increase has been observed in both laboratory and practical environment[60].The equation(2.22) derives the expression of the short-circuit current temperature coefficient.

(2) Temperature Coefficient of Open Circuit Voltage (V_{OC})

This coefficient indicates the percentage change in the open circuit voltage (V_{OC}) for a 1°C change in temperature. An increase in temperature usually leads to a decrease in the open circuit voltage, and vice versa. The equation (2.25) and the reading from [61] result in voltage temperature coefficient, $\mathrm{K_{voc}}$ equivalent to $\frac{\mathrm{d}V_{OC}}{\mathrm{d}T_{cell}}$. This value is negative and is depending on the solar cell material. For crystalline silicon cell it is -2.3mV/°C[61].

(3) Temperature Coefficient of Maximum Power Output (P_{max})

This coefficient reflects the percentage change in the maximum power output (P_{max}) for a 1°C change in temperature. It combines the effects of temperature on both the short circuit current and the open circuit voltage. It helps to predict how the overall power output of the solar panel will change with temperature variations.

The fill factor (FF) is a measure of the squareness of the I –V characteristic and is always less than one. It is the ratio of the areas of the two rectangles, one obtained from the maximum point values of current and voltage of solar cell/module and other from the values I_{SC} and V_{OC}.

$$FF = \frac{P_{max}}{V_{oc}I_{SC}} = \frac{V_{mp}I_{mp}}{V_{oc}I_{SC}} \tag{2.32}$$

An empirical expression of fill factor as it was given by [61] is an important figure of merit for solar cell efficiency.

$$FF = \frac{V_{oc} - \frac{kT_{cell}}{q} ln[\frac{qV_{oc}}{kT_{cell}}+0.72]}{V_{oc}+kT_{cell}/q} \tag{2.33}$$

The efficiency of solar cell is thus obtained from[61] by the following expression.

$$\eta_{cell} = \frac{P_{mp}}{P_{in}} = \frac{V_{oc}I_{SC}FF}{P_{in}} \tag{2.34}$$

2.2 Risk coefficient analysis

The real output of wind turbines differs from the ideal dispatch output, or the dispatch output of wind power, because wind power output is unpredictable, volatile, and uncontrollable, making it difficult to obtain accurate wind power generation in advance of the actual dispatch process.

2.2.1 Risk analysis of wind turbine output

There is some degree of both overestimation and underestimating.

When the wind turbine's actual generated power exceeds the ideal dispatch output, extra generated power enters the power network. To keep the system frequency from growing, the power system must discard some of the wind output that exceeds the power load demand. As a result, it is required to assess the system operation time.
The effects of underestimating wind power output on grid operations.

Wind power's underestimated production can be expressed by the penalty cost C_w^l and the underestimation power deviation P_w^l of wind power.

$$C_w^l = \sum_{i=1}^{n_w} k_w^l \,(P_w^a - P_w) = \sum_{i=1}^{n_w} k_w^l \int_{P_w}^{P_r}(\mathrm{P} - P_w)\, f_w(P)dP \tag{2.35}$$

$$P_w^l = \sum_{i=1}^{n_w}(P_w^a - P_w) = \sum_{i=1}^{n_w} \int_{P_w}^{P_r}(\mathrm{P} - P_w)\, f_w(P)dP \tag{2.36}$$

2.2.2 Risk analysis of photovoltaic power station output

Wind power generation exhibits high randomness and instability. Photovoltaic power plants, which are also renewable energy technologies, exhibit clear randomness and uncertainty when generating electricity. Access to large-scale photovoltaic power stations has posed issues to the functioning of the electricity grid. This unpredictable output power produces a difference between the solar power station's actual output power and the ideal dispatched output. As a result, the risk coefficient of the photovoltaic power station output can be turned into an analysis of overestimation and underestimating of the photovoltaic power station output. When a photovoltaic power station's real power generation surpasses the ideal photovoltaic dispatch output, excess power is generated in the power network, forcing the power system to reject some of the photovoltaic power that surpasses the power load need.

Underestimating a solar power station’s output can be indicated by the photovoltaic underestimation output penalty cost C_{pv}^{l} and the photovoltaic underestimation power deviation P_{pv}^{l}:

$$C_{pv}^{l}=\sum_{i=1}^{n_{pv}}k_{pv}^{l}\left(P_{pv}^{a}-P_{pv}\right)=\sum_{i=1}^{n_{pv}}k_{pv}^{l}\int_{P_{pv}}^{P_{pv}^{r}}\left(\mathrm{P}-\mathrm{P_{pv}}\right)f_{pv}(P)\mathrm{d}P \tag{2.37}$$

$$P_{pv}^{l}=\sum_{i=1}^{n_{pv}}\left(P_{pv}^{a}-P_{pv}\right)=\sum_{i=1}^{n_{pv}}\int_{P_{pv}}^{P_{pv}^{r}}\left(\mathrm{P}-P_{pv}\right)f_{pv}(P)\mathrm{d}P \tag{2.38}$$

Where k_{pv}^{l} is the penalty coefficient for underestimating the output of the photovoltaic power station; n_{pv} is the number of photovoltaic units; P_{pv}^{a} is the actual power generation of the photovoltaic power station; P_{pv} is the planned output of the photovoltaic power station; P_{pv}^{r} is the rated power of the photovoltaic power plant.

When the actual power generation of the photovoltaic power station does not reach the ideal wind turbine dispatching output, there will be a shortage of available power in the power network. At this time, it is necessary to generate electricity through the spinning reserve of the heat power unit to make up for the lack of photovoltaic power.

The indicator of photovoltaic power station overestimation output can be represented by the penalty cost of its output and the deviation of photovoltaic overestimation power.

$$C_{pv}^{h}=\sum_{i=1}^{n_{pv}}k_{pv}^{h}\left(P_{pv}-P_{pv}^{a}\right)=\sum_{i=1}^{n_{pv}}k_{pv}^{h}\int_{0}^{P_{pv}}\left(P_{pv}-P\right)f_{pv}(P)dP \tag{2.39}$$

$$P_{pv}^{h}=\sum_{i=1}^{n_{pv}}\left(P_{pv}-P_{pv}^{a}\right)=\sum_{i=1}^{n_{pv}}\int_{P_{pv}}^{P_{pv}^{r}}\left(P_{pv}-\mathrm{P}\right)f_{pv}(P)dP \tag{2.40}$$

Where k_{pv}^{h} is the penalty coefficient for overestimating the output of PV power plants.

2.3 Case analysis of the impact of distributed power on power system

The IEEE 33-node system is connected to various distributed generation (DG) types independently. The effects of these DG connections on the distribution network's functionality are compared and evaluated.

2.3.1 Case analysis of the impact of distributed power supply on the power system

Different types of DGs are connected to the 14th,22nd, and 30th nodes, and the convergence accuracy of power flow calculation is set to 10^{-4}. The parameters of different types of distributed power sources are shown in Table 2.1

表 2.1 不同类型分布式电源的参数

Table 2.1 Parameters of different types of distributed power sources

Distributed power supply	Equivalent node type	Parameter
Fuel cells	PI	P = 300kW& I=50A
Microgas turbine	PV	P = 300kW，Q_{max}=500kVar &V=0.98 p.u.
Wind power	PQ	P = 300kW& cos θ = 0.9
Solar PV power	PQ(V)	P = 300kW

Table 2.1shows that the various DG types' active outputs are all set to 300 kW. A PV node's corresponding node's DG reactive output has a 500 kVar maximum limit. In the event that the distributed power source's reactive power output above the upper limit, it will be transformed into a PQ node for computation purposes, with the reactive output taking the maximum value.

The forward-backward substitution approach is used to compute the power flow, which yields the active power loss, number of iterations, and distribution of each type of DG linked to the grid. Table 2.2 displays the distributed power supply's active and reactive power outputs, as well as the voltage at the grid-connected nodes.

表 2.2 四种分布式电源并网的计算结果

Table 2.2 Calculation results of four types of distributed power grid connection

Index/target	Equivalent node type				
	PI	PV	PQ	PV	No DG
Active power loss (kW)	141.49	141.44	151.43	147.44	202.65
Number of iterations (times)	4	4	4	4	4
Active power output DG (kW)	300	300	300	300	0
Reactive power output DG (kVar)	534	500	145	225	0
Grid-connected V node (p.u.)	0.9671	0.9652	0.9447	0.9495	0.9133

Table 2.2 demonstrates that the forward-backward substitution method converges in the power flow calculation of four types of DG grid connection, and the number of iterations is 4, indicating that the number of iterations of the algorithm does not change with different DG types, and it has better stability. After the DG whose equivalent node is a PV node is connected to the grid, its grid-connected node voltage does not achieve the preset 0.98 p.u. because its reactive power output approaches the top limit and cannot meet the node's reactive power requirement. The grid-connected node voltage of each DG has increased as compared to the system without DG access, with the DG with equivalent nodes of PI and PV type showing the biggest improvement. At the same time, the power loss indicators of the distribution network have improved after each DG is connected to the grid, indicating that connecting different types of DG to the distribution network can reduce the system's active power loss while also improving its energy efficiency. The system node voltage distribution after different types of DG is

connected to the grid is shown in Figure 2.3.

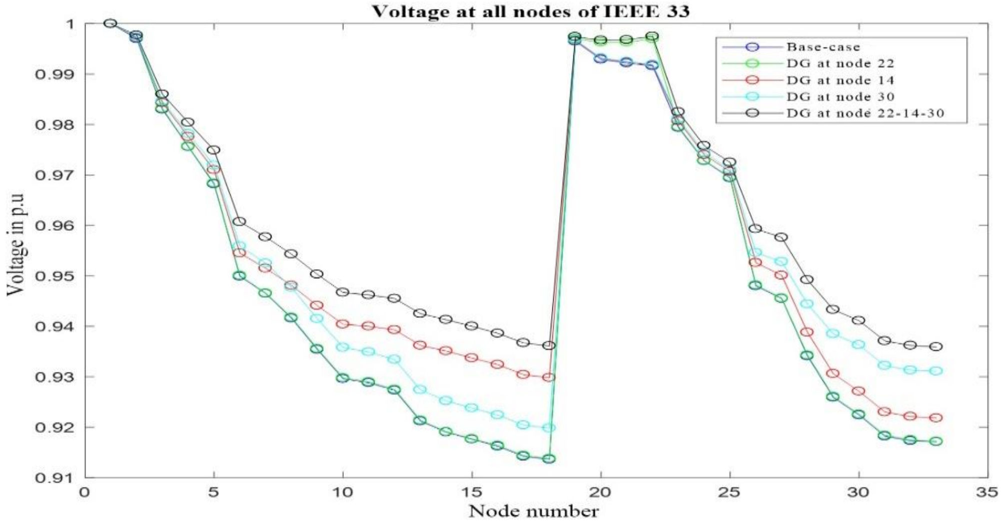

图 2.3 连接到配电网的不同类型分布式电源的系统电压分布图

Figure 2.3 System voltage distribution of different types of distributed power sources on the distribution network

Figure 2.3 shows that, when different forms of DG are connected to the distribution network, the system's performance improves in comparison to the system without DG access shown as base case in Figure 2.3

Although node voltage variations have been reduced, the majority of node voltages remain lower than 0.96 p.u., indicating that the voltage is below the lower limit. It demonstrates that, while connecting dispersed power sources to the grid helps reduce system voltage fluctuations, it does not meet the system's power quality criteria. The three DGs are connected to the grid at the 14th, 22nd, and 30th nodes. The voltage rise is greatest at the grid-connected node, and the voltage rise decreases as distance from the node increases.

2.3.2 Case analysis of the impact of distributed power supply capacity on the power system

In the IEEE 33-node system, a distributed power supply whose equivalent node is a PQ node is connected to the 14th node. Next, the DG capacity connected to the distribution network is changed, so that DG with different capacities can be analyzed for their effects on the distribution network's operation. Based on the system load, the active output amounts to 0%, 20%, 40%, 60%, and 80%, in that order. The power flow calculation convergence accuracy of the DG, whose equivalent node is a PQ-type node, is 10^{-4}. It uses constant power factor management with a power factor of 0.9. Table 2.3 displays the distribution network's active power loss, number of iterations, active power output, and reactive power output after the power flow is calculated using the forward-backward substitution method.

表 2.3 不同容量的分布式电源并网计算结果

Table 2.3 Calculation results of grid connection of distributed power sources with different capacities

Index/target	Distributed power generation active output to total load				
	0%	20%	40%	60%	80%
Active power loss (kW)	202.65	119.52	136.57	219.09	350.67
Active power output DG (kW)	0	743	1486	2229	2972
Reactive power output DG (kVar)	0	359.85	719.70	1079.55	1439.41
Number of iterations(times)	4	4	4	5	6

Table 2.3 illustrates that the system with DG active output accounting for 20% of the total load has an 83.13 kW reduction in active power loss when compared to the system with DG active output of 0. When the DG output makes up more than 40%, the distribution network's active power loss rises as the DG active output does as well. It demonstrates that when the DG grid-connected capacity surpasses the grid-connected node's absorption capacity, the node will not be able to completely absorb its output, leading to a reversal in the power flow where power moves from the DG grid-connected node to the balance node, increasing the distribution network's power loss.

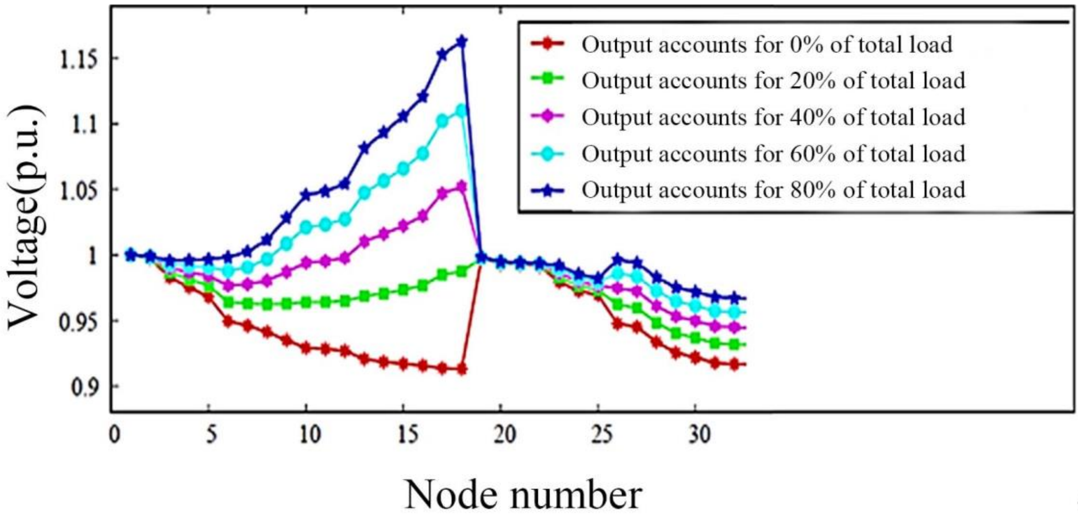

图 2.4 配电网连接不同容量分布式发电的系统电压分布图

Figure 2.4 System voltage distribution of different capacity of distributed generation connected to distribution network

Figure 2.4 shows that when the DG output is zero, the voltages of several nodes in the system are less than 0.95 p.u., indicating that the voltages exceed the lower limit. When the DG output accounts for 20% of the total load, the system node voltage rises, suggesting that system power quality can be enhanced even when the grid-connected DG output is minimal. When the DG output represents 40%, 60%, or 80% of the total load, the node voltage appears to be greater than 1.05 p.u., indicating that when the DG output exceeds the node's absorption capacity, a reverse power flow occurs, and the voltage of some nodes in the system exceeds the voltage upper limit which affect the distribution network's safety and stability[42],[62]–[65].

2.4 Summary

This chapter constructs two typical distributed power generation (DG) mathematical models, introduces the forward-backward substitution method to calculate the power flow of the distribution network containing DG, and then simulates and analyzes the impact of DG grid connection on the operation of the distribution network in the test system, and verified the effectiveness of the forward-backward substitution method. The specific summary is as follows:

First, based on the operating principles of photovoltaic power generation systems and wind power generation systems, mathematical models of photovoltaic power generation and wind power generation are constructed.

Secondly, in the power flow calculation of distribution network containing DG, the processing methods of different types of DG equivalent nodes are explained, and the forward and backward generation power flow algorithm is introduced.

Finally, the impact of different types and capacities of DG connected to the grid on the operation of the distribution network was simulated and analyzed in the test system, and the effectiveness of the forward-backward substitution method was verified. The results show that different types of DG grid connection can reduce system active power loss and increase node voltage. However, when the DG grid connection capacity exceeds the node absorption capacity, it will lead to an increase in power loss and a decrease in power quality in the distribution network; the forward-backward substitution method is the number of iterations in the power flow calculation of different types of DG grid connection is 4, and all can converge reliably, verifying its effectiveness.

The distributed power generation modeling and grid connection analysis in Chapter 2, as well as the forward-backward power flow algorithm introduced, lay the research foundation for the operation optimization of the distribution network containing DG in subsequent chapters.

Chapter 3 Optimizing Power System Operations with Distributed Supplies

The optimization of distributed power supply, inclusive of distribution network operation, represents a multifaceted nonlinear optimization challenge characterized by numerous objectives, variables, and constraints. Addressing such complexity necessitates a multi-objective optimization approach endowed with robust optimization capabilities. Traditional mathematical techniques often fall short in efficiently resolving these intricate optimization issues. In contrast, artificial intelligence (AI) algorithms confront difficulties in addressing the nonlinearity and diversity of these challenges. Consequently, there is a pressing need for the development of high-performance, realistic solutions tailored to optimizing power systems operation processes. The utilization of AI algorithms for multi-objective optimization presents a promising avenue for addressing multi-objective, multi-constraint, multivariate, and nonlinear aspects with notable efficiency. Specifically, the application of the Firefly Algorithm (FA) for the optimization of hybrid solar and wind energy systems at the power distribution level, as demonstrated through a case study on the IEEE 33-bus system, emerges as an innovative strategy to enhance the integration and operation of renewable energy within electrical networks. This discussion elucidates the potential advantages, challenges, and considerations inherent in employing FA for such purposes.

Potential Benefits:

(1) Optimal Sizing and Placement: FA's capability to ascertain the optimal size and placement of solar and wind energy resources within the distribution network is instrumental in maximizing efficiency, minimizing losses, and enhancing voltage profiles.

(2) Handling Nonlinear Objectives and Constraints: The algorithm's adeptness at navigating nonlinear optimization challenges aligns well with the complex dynamics of power systems, encompassing nonlinear load flows, fluctuating renewable outputs, and technical constraints (e.g., voltage limits, line capacities).

(3) Adaptability to Variable Conditions: FA's flexibility in dynamically optimizing hybrid system operations in response to changing weather conditions and load demands caters to the variability of solar and wind energy.

(4) Multi-objective Optimization: When tailored for multi-objective optimization, FA can concurrently optimize multiple objectives, reducing energy losses, costs, and environmental impacts while enhancing reliability and renewable energy integration.

Challenges and Considerations:

(1) Computational Complexity: The computational demands of optimizing hybrid solar and wind systems within an IEEE 33-bus distribution network, given its high-dimensional problem space and multiple load flow analyses requirements, necessitate consideration of FA's computational efficiency.

(2) Integration with Power Flow Models: Effective optimization mandates FA's integration with precise power flow models (e.g., AC load flow) to assess different configurations' impacts on network performance, adding complexity to the optimization endeavor.

(3) Dynamic and Stochastic Nature of Renewables: The algorithm must accommodate the unpredictable nature of solar and wind generation, potentially through probabilistic models or scenarios, to ensure robust solutions.

(4) Scalability: The adaptability of FA to larger or more intricate networks with greater renewable penetration merits evaluation.

(5) Practical Implementation Issues: Real-time data availability, control capabilities, and integration with existing distribution management systems are crucial for the practical deployment of FA-derived optimization solutions.

In summary, the Firefly Algorithm offers a promising tool for optimizing the integration and operation of hybrid solar and wind energy systems at the distribution level. It adeptly addresses the complex, nonlinear, and multi-constraint nature of such challenges. However, its successful application hinges on careful consideration of computational efficiency, integration with power system models, and the management of variability and uncertainty in renewable energy sources. Future investigations and pilot implementations of FA in real-world contexts, such as the IEEE 33-bus system, will yield valuable insights into its efficacy and practical challenges in optimizing hybrid renewable energy systems.

3.1 Analysis and Improvement of Multi-objective Firefly Algorithm

The Firefly Algorithm (), conceived by Dr. Xin-She Yang in 2008, is a metaheuristic optimization technique inspired by the luminescent signals of fireflies[66].

3.1.1 Principle of Firefly Algorithm

Its operational foundation rests on three primary principles reflecting firefly behavior:

(1) Attractiveness: A firefly's appeal is directly linked to its luminosity, diminishing with increasing distance. In optimization, this luminosity corresponds to the value of the objective function, guiding fireflies (solutions) toward those with

superior outcomes.

(2) Distance: The algorithm employs the concept of distance to modulate the attractiveness between fireflies, promoting movement towards more luminous peers, with proximity enhancing this attractive force.

(3) Randomness: Integrating a stochastic component, the algorithm facilitates exploration beyond immediate attractions, aiding in the evasion of local optima and the discovery of superior solutions across the broader search landscape.

The operation of the Firefly Algorithm can be summarized in the following four steps:

(i) Initialization: Generate an initial population of fireflies (solutions) randomly distributed throughout the search space.

(ii) Evaluation: Calculate the brightness (objective function value) of each firefly.

(iii) Movement: Update the position of fireflies based on their attractiveness and distance to other fireflies, moving less bright fireflies towards brighter ones, with an element of randomness to avoid local optima.

(iv) Iteration: Repeat the evaluation and movement steps until a termination criterion is met (such as a maximum number of iterations or a satisfactory objective function value).

The movement of a firefly i towards a more attractive (brighter) firefly j is typically modeled using the following equation.

$$x_i^{(k+1)} = x_i^{k} + \beta_0 e^{-\gamma r_{ij}^2}\left(x_j^{(k)} - x_i^{(k)}\right) + \alpha\epsilon_i \tag{3.1}$$

Where x_i^{k} and x_j^{k} are the positions of fireflies i and j at iteration k, β_0 is the attractiveness at distance 0, γ is the light absorption coefficient, r_{ij} is the distance between fireflies i and j, α is a randomness factor, and ϵ_i is a vector of random numbers drawn from a Gaussian distribution or other distributions.

The Firefly Algorithm's simplicity, coupled with its effective exploration and exploitation capabilities, makes it suitable for a wide range of optimization problems, including those with complex, multimodal landscapes. Research studies have found the global optima of various test functions and suggest that particle swarm often outperforms traditional algorithms such as genetic algorithms, while the new firefly algorithm is superior to both PSO and GA in terms of both efficiency and success rate[66].

3.1.2 Firefly Algorithm Improvement Strategy

The Firefly Algorithm (FA), since its inception, has been subject to various improvement strategies aimed at enhancing its efficiency, convergence speed, and ability to navigate complex optimization landscapes. Improvement strategies typically focus on modifying the algorithm's core components, such as attractiveness, distance measurement, and the randomness factor, to optimize performance across diverse problem sets. Here, we outline key strategies and incorporate equations that are central to these enhancements.

(1) Adaptive Attractiveness Modification

To address the standard FA's limitation in balancing exploration and exploitation, the attractiveness function can be adapted to change dynamically with iterations. This ensures that the algorithm can maintain diversity in early stages (exploration) and intensify focus on promising regions as it converges (exploitation)[67]. The modified attractiveness function can be represented as:

$$\beta(r) = \beta_0 e^{-\gamma r^2} \tag{3.2}$$

Where β(r) is the attractiveness at a distance r, β_0 is the attractiveness at zero distance, and γ is a light absorption coefficient that can be adjusted adaptively based on the iteration count or the diversity of solutions.

(2) Enhanced Distance Measurement

Improvements in calculating the distance between fireflies can significantly influence the FA's ability to explore the search space effectively. A generalized form of an enhanced distance metric could be represented as follows:

$$d_{ij} = \sqrt{\sum_{k=1}^{n} \omega_k * \left(x_{i,k} - x_{j,k}\right)^2} \tag{3.3}$$

Where d_{ij} represents the distance between firefly i and firefly j, $x_{i,k}$ and $x_{j,k}$ denote the k^{th} dimensional component of the position vectors of fireflies I and j respectively; n is the number of the dimension in the search space, and w_k is an adjustable weight factor that shows the importance or scale of the k^{th} dimension in the distance measurement.

(3) Controlled Randomness

The strategy in the Firefly Algorithm enhances its search efficiency by dynamically tuning the randomness factor (α). The approach varies α or introduces additional stochastic elements according to the optimization stage, facilitating broader exploration early on and concentrating on exploitation as the search progresses. The formula governing a firefly “i” movement toward a more luminous firefly j incorporates this controlled randomness, described as follows:

$$x_i^{(k+1)} = x_i^{k} + \beta(r) * \left(x_j^{k} - x_i^{k}\right) + \alpha * (rand - 0.5) \tag{3.4}$$

Where $x_i^{(k+1)}$ denotes the new position of firefly i; $x_i^{k}\ and\ \ x_j^{k}$ are the current positions of fireflies i and j, respectively. $\beta(r)$ signifies attractiveness function dependent on their distance r, and Rand is a random number between 0 and 1. The term $\alpha * (rand - 0.5)$ introduces a controlled random step, allowing the algorithm to escape local optima and thoroughly explore the search space.

3.1.3 FA in Power Systems: Scheduling, Dispatch, and Renewables

The integration of renewable energy sources, alongside traditional power generation methods, necessitates advanced optimization techniques to manage the complexity and variability inherent in power systems. The Firefly Algorithm (FA), inspired by the natural behavior of fireflies, offers a promising approach to multi-objective optimization challenges in power systems, including generation scheduling, economic dispatch, and renewable energy integration[68][69]. This thesis explores the application of FA to these critical areas, emphasizing the algorithm's adaptability, efficiency, and effectiveness in balancing conflicting objectives such as cost minimization, emission reduction, and system reliability[70]**.**This thesis will focus on power loss minimization, maximizing the voltage stability margin or minimize the voltage deviation while ensuring high renewable distribution integration in the power system[69]. FA with its core mechanisms such as attraction based on brightness (solution quality) and movement towards brighter fireflies (better solutions)—are particularly suited to multi-objective optimization, where the goal is to find a set of optimal solutions that represent the best trade-offs among competing objectives[71].The fundamental concepts in the operation of electric power systems while focusing on the optimizations of generation and distribution of electricity in order to meet demand efficiently are known as economic dispatch and generation scheduling[72].

(1) Economic load Dispatch

Economic load dispatch (ELD) concerns the allocation of generation resources i.e. optimal placement to meet the power demand at the lowest possible cost, subject to operational and system constraints. Incorporating renewable energy sources into the ELD problem introduces variability and uncertainty, making the optimization problem more complex. MOFA is employed to obtain optimum solution for both the generation cost and the deviation from planned renewable energy usage, ensuring a cost-effective and reliable power supply[71]. The MOFSA-based ELD model considers multiple objectives, such as cost minimization and maximization of renewable energy utilization, and applies the algorithm's movement and attractiveness mechanisms to find the optimal generation mix across different sources. Since the purpose of ELD is to minimize the total generation cost while fulfilling the demand and operating within the technical limits of the generators, its objective function is defined as follows[73]:

$$Min \sum_{i=1}^{N} C_i \left(P_i\right) \tag{3.5}$$

Where N is the number of generating units, $C_i(P_i)$ is the cost function of generating unit i, typically expressed as quadratic function:

$$C_i(P_i) = C_i P_i^2 + b_i P_i + a_i \tag{3.6}$$

Where P_i is the power output of generating unit i that is subjected to the following constraints:

$$\sum_{i=1}^{N} P_i = D_k + P_{loss} \tag{3.7}$$

Where "D_k" is the total system demand at time k, also known as P_{load} and P_{loss} represents the total transmission losses, which can be calculated using various methods, such as the bi-coefficient methods. Another constraint is given such that,

$$P_{i,min} \leq P_i \leq P_{i,max} \tag{3.8}$$

Where $P_{i,min}$ and $P_{i,max}$ are the minimum and maximum output levels for generating unit i.

(2) Generation Scheduling

Generation scheduling involves determining the optimal start-up and shut-down times of power generation units to meet demand while minimizing costs and emissions. The multi-objective firefly search algorithm (MOFSA) can be adapted to address this problem by defining the objectives as minimizing fuel costs and emissions simultaneously. MOFSA's ability to explore the solution space efficiently helps in identifying the Pareto optimal schedule that balances generation and demand with minimum unavoidable losses. MOFSA can dynamically adjust its parameters to enhance the exploration and exploitation capabilities throughout the optimization process, leading to improved scheduling strategies that accommodate the inherent uncertainties in power demand and generation capabilities. The formation of generating scheduling objective equation includes an additional term for start-up and shut-down costs and extends over multiple time periods.

$$Min \sum_{k=1}^{T} \sum_{i=1}^{N} (C_i(P_{i,k}) + S_{i,k} + U_{i,k}) \tag{3.9}$$

Where T is the number of times periods in the scheduling horizon, $P_{i,k}$ is the power output of generating unit i at time k. $S_{i,k}$ and $U_{i,k}$ are the start-up and shut-down costs for generating unit i at time k.

The generation scheduling is subject to the following constraints:

(i) Power balance for each time period:

$$\sum_{i=1}^{N} P_{i,k} = D_k + P_{loss,k} \textit{ for all values of times, k.} \tag{3.10}$$

(ii) Generation capacity and ramp rate constraints for each unit 'i' and time period k.

$$P_{i,min} \leq P_{i,k} \leq P_{i,max} \qquad (\forall i, k) \tag{3.11}$$

$$R_{i,\downarrow} \leq P_{i,k} - P_{i,k-1} \leq R_{i,\uparrow} \quad (\forall i, k) \tag{3.12}$$

Where $R_{i,\downarrow}$ and$R_{i,\uparrow}$ are the ramp-up and ramp-down rates for generating unit 'i'.

(iii) Unit minimum up and down time constraints, ensuring that once a unit is started, it remains ON for a minimum period and vice versa.

(iv) The other operational constraints such as reserve requirements, transmission constraints, and environmental regulations may also be included.

the economic dispatch and generation scheduling are complex optimization problems in power systems that are typically solved using various mathematical programming techniques, including linear programming (LP), mixed-integer linear programming (MILP), dynamic programming (DP), and heuristic or metaheuristic algorithms. The specific formulation and solution approach depend on the system characteristics, available generation resources, and the particular objectives and constraints of the utility or system operator.

(3) Renewable Energy Integration

The integration of renewable energy sources into the power grid presents challenges related to variability, uncertainty, and grid stability. MOFSA is utilized to optimize the integration process, focusing on objectives like maximizing the penetration of renewable energy, minimizing balancing costs, and ensuring grid stability, and efficiency. The complete computational derivation covering all aspects of renewable integration may be extensive and complex.

However, a summary of critical points and key notations often involved in the process is herewith given:

(i) Power flow equations.

At the center of grid integration, the power flow equations that ensure the balance between generation and load while accounting for the physical constraints of the network are given by:

$$P_i = V_i \sum_{j=1}^{N} V_j \left(G_{ij} cos\theta_{ij} + B_{ij} sin\theta_{ij}\right) \quad (3.13)$$

$$Q_i = V_i \sum_{j=1}^{N} V_j \left(G_{ij} sin\theta_{ij} - B_{ij} cos\theta_{ij}\right) \quad (3.14)$$

Where P_i and Q_i define the active and reactive power injection at bus i. V_i and V_j are the voltage magnitude at bus i and j respectively. θ_{ij} is the phase angle distance between buses i & j. G_{ij} & B_{ij} are the conductance & susceptance of the line connecting buses i and j. N is the total number of buses in the system.

(ii) Generation and Load Balancing

Renewable energy sources, such as wind and solar, are variable and somewhat unpredictable. The generation from these sources must be balanced with the load and other forms of generation, often requiring advanced forecasting techniques and flexibility in the operation of conventional generators. The balance equation is given by:

$$\sum_{i \in RES} P_{Gi} + \sum_{i \in conv} P_{Gi} = P_{load} + P_{loss} \tag{3.15}$$

Where P_{Gi} is the power generation from source i, P_{load} is the total load demand and P_{loss} represents the system losses.

(iii) Voltage Stability and Control

Integrating RES impacts the voltage profile across the network bus. Voltage stability can be analyzed using the Jacobian matrix derived from the power flow equations, and control requires appropriate reactive power support, which can be mathematically represented as:

$$\Delta Q = -[J_{QQ}]^{-1} Q_{mis} \tag{3.16}$$

Where ΔQ is the vector of reactive power adjustments, J_{QQ} is the reactive power Jacobian matrix, and Q_{mis} is the vector of reactive power mismatches.

3.2 Pseudocode representation of the standard firefly Algorithm

The firefly algorithm is a nature-inspired optimization technique that simulates the flashing behavior of fireflies, seeking the brightest (optimal) solution in a search space. It begins by initializing parameters such as gamma for light absorption, beta0 for initial attractiveness, alpha for step size, and MaxGen for the maximum iterations. A population of fireflies is then initialized with random positions, and their fitness is evaluated. The algorithm enters a loop where each firefly moves toward brighter ones, with attractiveness diminishing with distance. This is calculated using an exponential decay function. Fireflies update their positions based on the attractiveness and a random step. Fitness is re-evaluated after each movement.

This pseudocode has been meticulously crafted to serve as an exhaustive roadmap of the firefly algorithm's architecture. It elucidates the sequence of operations and decision points in a coherent and logical sequence. The subsequent depiction, presented in the form of Table 3.1, is not merely an outline; it is a testament to the structured approach that is required to grasp the intricacies of the firefly algorithm's execution.

Table 3.1 not only enumerates the algorithm's steps but also elucidates the underlying rationale that governs each phase of the process. From the initialization of parameters that establish the context for the algorithm's operation to the iterative refinement of potential solutions, the table encapsulates the essence of the firefly algorithm's traversal of the search space. This pseudocode and the accompanying table are designed to serve as an educational tool, rather than a mere guide, for those seeking to understand or apply the firefly algorithm. The pseudocode and table aim to demystify the algorithm's process, offering clarity and depth to those who may be unfamiliar with it.

表 3.1 萤火虫算法工作原理代码

Table 3.1 Pseudocode explaining the working principle of firefly algorithm

```
Algorithm: Firefly Algorithm
Input: Objective function f(x), number of fireflies N, light absorption coefficient gamma, attractiveness beta0, step size alpha, maximum generations MaxGen
Output: Best solution found
Initialize algorithm parameters:
    - gamma (light absorption coefficient)
    - beta0 (attractiveness at distance = 0)
    - alpha (step size for random movement)
    - MaxGen (maximum number of generations)
Initialize firefly population:
    For i = 1 to N do:
        Initialize position xi randomly within the search space
        Evaluate fitness: fi = f(xi)
Define the best solution found so far as the one with the highest fitness
For gen = 1 to MaxGen do:
    For i = 1 to N do:
        For j = 1 to N do:
            If $f(xi) < f(x_j)$ then:
                Calculate distance $r_{ij} = ||x_i - x_j||$
                Calculate attractiveness beta = beta0 * exp (-gamma * $r_{ij}^2$)
                Move firefly i towards j:
                    $x_i = x_i$ + beta * ($x_j - x_i$) + alpha * (rand - 0.5) * epsilon
                Evaluate new solution $f_i = f(x_i)$
                If fi is better than the best solution found so far, update the best solution
Optionally, update alpha (step size) if necessary, depending on the algorithm variant
Display the best solution and its fitness value found in this generation
Output the best solution and its fitness value found after MaxGen generations
```

The working principle of firefly algorithm is hereby explained as follow:

Step1: Initialize algorithm parameters.

gamma: The light absorption coefficient, affecting how the attractiveness of firefly decreases with distance.

beta0: The attractiveness of a firefly at zero distance, indicating how appealing a firefly is before distance effects are considered.

alpha: the step size for random movements, controlling the extend of exploration in the search space.

MaxGen: The maximum number of generations, or iteration, the algorithm will run to search for the best solution.

Step 2: Initialize firefly population.

For each firefly ‘i’ (where “i=1 to ‘N’):

Randomly initialize position x_i within the search space.

Evaluate fitness $f(x_i)$ using the objective function f, where x_i is the position of firefly ‘i’.

Step3: Define the best solution.

Identify the firefly with the highest fitness value as the best solution found so far.

Step4: Algorithm’s main loop.

For each generation ‘Gen’ i.e. (from 1 to ’MaxGen’):

For each firefly ‘i’ in the population:

For each other firefly ‘j’:

If $f(x_i) < f(x_j)$:This means firefly ‘i’ is less bright than firefly ‘j’, and thus, it should move towards ‘j’.

Calculate distance $r_{ij}=\|x_i - x_j\|$,using Euclidean distance formula.

Calculate attractiveness $\beta= \beta_0.\exp(-\gamma.\ r_{ij}^2)$. This formula demonstrates how the attractiveness decreases exponentially with the square of the distance between fireflies, modulated by γ.

Move firefly ‘i’ towards ‘j’ using the movement formula:

$$x_i = x_i + \beta.\left(x_j - x_i\right) + \alpha.(\mathrm{rand} - 0.5).\epsilon$$

Where rand is random number between 0 and 1, and ϵ is a small constant to ensure movement.

Re-evaluate fitness $f(x_i)$ for the new position of firefly ‘i’.

Update the best solution if the new fitness $f(x_i)$ is better than the current best solution.

Optionally, adjust the step size ‘α’ based on the algorithm variant.

Step5: Display and output the best solution.

At the end of the ‘MaxGen’ generations, display and output the best solution found along with its fitness value.

By following the prescribed methodology, the Firefly Algorithm effectively emulates the natural phenomenon of fireflies, where each individual firefly represents a potential solution traversing the multidimensional search space. This bio-inspired metaheuristic leverages the inherent principle of fireflies being attracted to one another based on their relative brightness, which, in the context of the algorithm, corresponds to the quality of the solution they represent.

The algorithm's core mechanism is the dynamic interaction between fireflies, where their attractiveness is governed by the inverse square law. This implies that the allure diminishes as the distance between them increases.

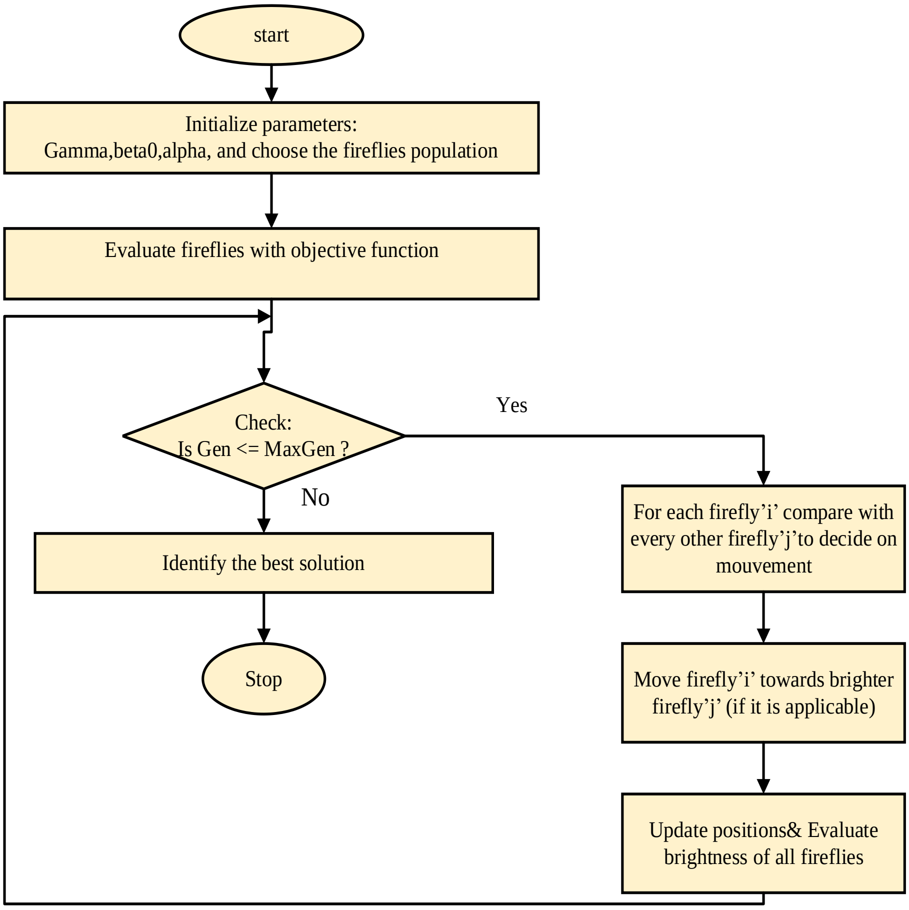

图 3.1 标准萤火虫算法流程图

Figure 3.1 Standard flowchart of the firefly algorithm

As can be seen from Figure 3.1, the specific steps of the Firefly Algorithm (FA) algorithm to solve the static comprehensive optimization model of distribution networks containing distributed power sources are:

Step 1: Problem Definition

(a) Objective Function Definition: Clearly define the objective function that needs to be optimized. This could involve minimizing the network's total energy losses, improving voltage stability, or optimizing the cost-efficiency of operating distributed power sources within the distribution network.

(b) Constraint Identification: Enumerate all relevant constraints for the distribution network, including power flow constraints, voltage limits at different nodes, maximum and minimum power output levels of distributed sources, and any regulatory or operational constraints.

Step 2: Parameters Initialization of Firefly algorithm

(a) Initialization of Population: Determine the size of the firefly population (number of solutions) and generate initial positions for each firefly randomly. Each position corresponds to a possible solution for the distribution network optimization, encoding variables like distributed generator outputs, reactive power device settings, and network configuration changes.

(b) Light Intensity and Attractiveness: Define the relationship between a firefly's light intensity (objective function value) and its attractiveness to other fireflies, ensuring that better solutions have higher attractiveness.

(c) Absorption Coefficient: Set the value that dictates how the attractiveness decreases with distance, affecting the movement of fireflies towards each other.

(d) Randomness Factor: Establish the degree of randomness in firefly movement to ensure exploration of the solution space.

(e) Maximum Iterations: Specify the maximum number of iterations or other convergence criteria to terminate the algorithm.

Step 3: Evaluate Initial Population

For each firefly in the initial population, evaluate the objective function based on the encoded solution. This involves performing a simulation or calculation that determines how well the solution meets the optimization goals under the given constraints.

Step 4: Attraction-based Movement

(a) Movement Towards More Attractive Solutions: Compare the light intensity (objective function value) of each pair of fireflies and move the less attractive firefly towards the more attractive one, according to the FA's rules, which incorporate both the attractiveness (dependent on the objective function and absorption coefficient) and a randomness factor.

(b) Constraint Handling: Ensure that the movement respects the defined constraints, adjusting firefly positions if they move outside feasible solution space.

Step 5: Update Fireflies and Objective Function

After moving the fireflies, re-evaluate the objective function for each firefly in their new positions. Adjustments might be made to keep the solutions within the feasible region.

Step 6: Iterative Optimization

(a) Repeat Steps 4 and 5: Continue the process of comparing, moving, and updating fireflies based on their attractiveness and re-evaluating their objective function values.

(b) Check for Convergence: At each iteration, check if the algorithm has met the convergence criteria, such as a satisfactory improvement in the objective function or reaching the maximum number of iterations.

Step 7: Optimal Solution Extraction

Once the algorithm converges, identify the firefly (solution) with the best objective function value as the optimal solution for the distribution network's static comprehensive optimization problem.

Step 8: Validation and Analysis

(a) Validate the obtained optimal solution through additional simulations or analytical methods to ensure its feasibility and effectiveness in the real-world operation of the distribution network with distributed power sources.

(b) Analyze the solution to understand its impact on the network's performance, including energy savings, reliability improvements, and operational cost reductions.

By methodically following these steps, the Firefly Algorithm can effectively solve complex optimization problems in distribution networks, providing significant benefits in terms of operational efficiency, stability, and cost-effectiveness.

3.3 Multi-objective Firefly Algorithm Performance Test Analysis

3.3.1 Classical Multi-Objective Test Functions and Evaluation Metrics Selection

In order to verify the solution performance of the multi-objective firefly algorithm based on the hybrid strategy, six classical multi-objective test functions are selected in this section to test the performance of the multi-objective firefly search algorithm (MOFSA), and four evaluation metrics are chosen to assess the performance of the algorithm.

(i) Standardized test function selection

In order to provide a comprehensive evaluation of the efficacy and quality of the Multi-Objective Firefly Algorithm (MOFSA), this section presents a series of experiments utilizing benchmark test functions that encapsulate varying complexities and objectives. The evaluation process is conducted in two distinct phases, each designed to assess the algorithm's performance under different multi-objective scenarios.

Initially, a suite of test functions designed with two objectives is employed to examine the MOFSA's ability to navigate and optimize bi-objective optimization landscapes. These functions are selected for their diverse characteristics, including convex, non-convex, and mixed-Pareto frontiers, in order to provide a rigorous examination of the algorithm's convergence behavior and its capability to identify and trace the Pareto-optimal solutions effectively.

Subsequently, the complexity is increased by incorporating test functions that embody three objectives, with the objective of scrutinizing the MOFSA's proficiency in higher-dimensional solution spaces. The trivariate functions are designed to encompass a broader spectrum of challenges, including disconnected Pareto sets, irregularly shaped Pareto fronts, and complex interdependencies among objectives.

This phase is of paramount importance in evaluating the MOFSA's adaptability and robustness in the context of three-dimensional optimization problems.

Each test function possesses Pareto frontiers with different shapes, and the expressions, variable dimensions and search ranges of the test function containing two objectives are shown in Table 3.2

表 3.2 含两个目标的测试函数具体参数

Table 3.2 Specific parameters of the test function with two objectives

function	displayed formula	Search Scope	dimensionality of a variable
F1	$\begin{cases} min\, f_1(x) = x_1 \\ h(x) = 1 + 9 \times (\sum_{i=2}^{30} x_i)/29 \\ min\, f_2(x) = h(x) \times [1 - \sqrt{x_1/h(x)}] \end{cases}$	$x \in [0,1]$	30
F2	$\begin{cases} min\, f_1(x) = x_1 \\ h(x) = 1 + 9 \times (\sum_{i=2}^{30} x_i)/29 \\ min\, f_2(x) = h(x) \times [1 - (x_1/h(x))^2] \end{cases}$	$x \in [0,1]$	30
F3	$\begin{cases} min\, f_1(x) = x_1 \\ h(x) = 1 + 9 \times (\sum_{i=2}^{30} x_i)/29 \\ min\, f_2(x) = h(x) \times [1 - \sqrt{x_1/h(x)} - x_1/h(x) \times sin(10\pi x_1)] \end{cases}$	$x \in [0,1]$	30
F4	$\begin{cases} min\, f_1(x) = 1 - exp(-4x_1) \times sin^6(6\pi x_1) \\ h(x) = 1 + 9 \times (\sum_{i=2}^{30} x_i/9)^{0.25} \\ min\, f_2(x) = h(x) \times [1 - (x_1/h(x))^2] \end{cases}$	$x \in [0,1]$	10

Table 3.2 shows the specific parameters of the test function with two objectives, where: F1 and F2 have relatively low complexity, and the Pareto front of F1 is a continuous convex set, and the Pareto front of F2 is a continuous nonconvex set. F3 is a relatively high complexity test function with a discontinuous convex Pareto front, and F4 has the highest complexity, with a nonconvex Pareto front and an uneven distribution of densities and distribution is not uniform.

In order to test the solving ability of the MOFSA in the test function containing three objectives, the test function containing three objectives was used to test the algorithm's solving performance, and Table 3.2 demonstrates the expressions, variable dimensions, and search ranges of the test function containing three objectives.

表 3.3 含三个目标的测试函数具体参数

Table 3.3 Specific parameters of the test function with three objectives

function	displayed formula	Search Scope	dimensionality of a variable
F5	$\begin{cases} min\, f_1(x) = (1+\sum_{i=3}^{10}(x_i)^2) \times cos(0.5\pi x_1) \times cos(0.5\pi x_2 \\ min\, f_2(x) = (1+\sum_{i=3}^{10}(x_i)^2) \times cos(0.5\pi x_1) \times sin(0.5\pi x_2 \\ min\, f_3(x) = (1+\sum_{i=3}^{10}(x_i)^2) \times sin(0.5\pi x_1) \end{cases}$	$x \in [0,1]$	10
F6	$\begin{cases} min\, f_1(x) = (1+h(x)) \times cos(0.5\pi\theta_1) \times cos(0.5\pi\theta_2) \\ min\, f_2(x) = (1+h(x)) \times cos(0.5\pi\theta_1) \times sin(0.5\pi\theta_2) \\ min\, f_3(x) = (1+h(x)) \times sin(0.5\pi\theta_1) \\ \theta_1 = 0.5\pi x_1 \\ \theta_2 = \pi(1+2x_2h(x))/4(1+h(x)) \\ h(x) = \sum_{i=3}^{10}(x_i - 0.5)^2 \end{cases}$	$x \in [0,1]$	10

Table 3.3 shows the specific parameters of the test function containing three objectives, in which the Pareto front of test function F5 is a spatial surface, which is usually used to test the convergence performance of the algorithm in three-dimensional space. The test function F6 has a higher complexity and its Pareto front is a spatial curve, which is usually used to test the convergence accuracy and solving ability of the algorithm in three-dimensional space.

(ii) Algorithm performance evaluation index selection

The performance evaluation of the multi-objective optimization algorithm focuses on examining the convergence of the algorithm and the spatial distribution of the resulting Pareto front. For this reason, four metrics, namely, inverse generation distance, spatial evaluation, hypervolume, and average running time of the algorithm, are chosen in this section to comprehensively evaluate the solution performance of the algorithm.

1) Inverted Generational Distance (IGD)

The IGD metric is used to evaluate the convergence of the algorithm, the smaller the value indicates that the algorithm converges faster and with higher convergence accuracy[1]-[7], and its expression is given by:

$$IGD(P, P_T) = \frac{\sum_{x \in P_T, y \in P} min\{dis(x,y)\}}{N_T} \tag{3.17}$$

Where P_T , P and N_T represent the true Pareto front, the Pareto front obtained by the algorithm, and the number of solutions in P_T , respectively; and min { $dis(x,y)\}$

represents the minimum Euclidean distance between the solutions in P_T and the solutions in P.

(2) Spacing evaluation (SP)

SP index is the average distance between the solutions in the Pareto optimal solution set obtained by the algorithm to its neighboring solutions, reflecting the distribution of the Pareto optimal solution set obtained by the algorithm in the target space, and the smaller the value indicates that the spatial distribution of the Pareto optimal solution set obtained by the algorithm is better[80], and the SP expression is:

$$SP = \left(\frac{1}{N-1} \times \sum_{j=1}^{N} \left(d_j - \bar{d} \right)^2 \right)^{1/2} \tag{3.18}$$

Where d_j , N and $\bar{d}$ denote the minimum Euclidean distance from the j^{th} solution to the neighboring solutions in the set of Pareto-optimal solutions obtained by the algorithm, the number of solutions in the set of Pareto-optimal solutions obtained by the algorithm, and the average value of d_j, respectively.

(3) Hypervolume (HV)

HV index is the volume of the space surrounded by the Pareto optimal solution set and the reference point obtained by the algorithm, which can evaluate the convergence of the algorithm and the diversity of the solutions in the solution set obtained by the algorithm at the same time [1][2][5]-[7]. The larger the value of HV, the better the convergence of the algorithm, and the better the distribution of the solution set obtained by the algorithm and the better the diversity of solutions obtained by the algorithm, and its expression is:

$$HV = \chi \sum_{i=1}^{N} V_i \tag{3.19}$$

Where χ represents the Leberger measure, which is used to measure the volume; V_i represents the hypervolume formed by the i^{th} solution in the solution set obtained by the algorithm and the reference point; N represents the number of solutions in the solution set obtained by the algorithm.

(4) Average running time

The average value of the running time of 30 independent runs of the algorithm is selected as an evaluation index to measure the solution speed of the algorithm, and the smaller the value indicates that the algorithm solution speed is faster.

3.3.2 Comparison of Algorithm Selection and Parameter Settings

Non-dominated Sorting Moth Flame Optimizer (NSMFO), Multi-objective Particle Swarm Optimization (MOPSO) and Non-dominated Sorting Genetic Algorithm with Elite Strategy (NSGA-II) are all multi-objective optimization algorithms dominated Sorting Genetic Algorithm with Elite Strategy (NSGA-II) are all multi-objective optimization algorithms. The NSMFO algorithm is an excellent multi-objective optimization algorithm that mimics the life habits of moths, and it has a powerful spatial searching capability are classical multi-objective optimization algorithms, which are usually chosen as comparison algorithms. Therefore, NSMFO, NSGA-II and MOPSO algorithms are selected as comparison algorithms in this chapter to verify the effectiveness and advancement of the proposed firefly algorithm.

The parameter settings of NSMFO, NSGA-II, MOPSO and MOFSA algorithms are shown in Table 3.4

表 3.4 NSMFO、NSGA-II、MOMVO 和 MOFSA 算法的参数设置

Table 3.4 Parameter settings for NSMFO, NSGA-II, MOMVO and MOFSA algorithms

arithmetic	Parameterization		
	Main parameters	population size	Max. number of iterations
NSMFO	b=1, Archieve=100	100	100
NSGA-II	$P_C = 0.9$, $P_m = 0.15$, $m_s = 0.05$		
MOPSO	$C_1 =2$, $C_2 =2$, w=0.3, $U_p =0.5$, Archieve=100		
MOFSA	$W_p \in [0.2, 0.7]$, $R_2 = 0.7$, $SD = 0.1$, Archieve = 100		

As shown in Table 3.4, to ensure the objectivity and fairness of the experimental results, the population size and the maximum number of iterations are the same for all algorithms. In the NSMFO algorithm, b represents the spiral parameter and *Archieve* represents the external archive size. In NSGA-II algorithm, P_C, P_m and m_s represent crossover probability, variance probability and variance strength respectively. In MOPSO algorithm, C_1, C_2, w and U_p represent self-learning factor, social cognitive factor, inertia weight and uniform mutation rate respectively. In MOFSA algorithm, w_p, R^2 and SD represent population proportion factor, safety value and firefly proportion, respectively.

3.3.3 Algorithm simulation results and analysis

In addition, because the algorithm solution is a random optimization process, and there are random factors in the algorithm that lead to unstable final results, each algorithm is run independently for 30 times, and the value of each evaluation index is taken as the average of the results of the 30 runs. The IGD index values of each algorithm under different test functions are shown in Table 3.5

表 3.5 各算法 IGD 指标值

Table 3.5 IGD indicator values for each algorithm

arithmetic	F1	F2	F3	F4	F5	F6
NSMFO	1.66 x 10^{-2}	9.28 x 10^{-3}	3.15 x 10^{-2}	1.21	9.98 x 10^{-2}	5.92 x 10^{-3}
NSGA-II	1.71 x 10^{-2}	3.39 x 10^{-2}	2.31 x 10^{-2}	4.54 x 10^{-3}	9.93 x 10^{-2}	5.79 x 10^{-3}
MOPSO	1.74 x 10^{-2}	1.59 x 10^{-2}	2.89 x 10^{-2}	2.42 x 10^{-2}	2.02×10^{-1}	2.68 x 10^{-2}
MOFSA	**3.81 x 10^{-3}**	**3.92 x 10^{-3}**	**4.34 x 10^{-3}**	**3.08×10^{-3}**	**6.26 x 10^{-2}**	**5.11 x 10^{-3}**

Table 3.5 shows the IGD metric values for each algorithm, where the bolded font is the optimal value under each test function. Compared with NSMFO, NSGA-II and MOPSO algorithms, MOFSA algorithm proposed in this thesis obtains the optimal IGD values in all the test functions, which indicates that MOFSA has the best convergence, and the NSMFO algorithm's IGD value under the F4 test function is too large, which is not of the same order of magnitude as that obtained by the MOFSA algorithm, which indicates that the NSMFO algorithm has poor convergence, and it falls into local optimality and cannot find the Pareto optimal solution. NSMFO algorithm has poor convergence and it falls into local optimality and cannot find the Pareto optimal solution set. The MOFSA algorithm proposed in this chapter is able to obtain the Pareto optimal solution set in the test functions F1 to F6 with optimal IGD values, which indicates that compared with other multi-objective optimization algorithms, the proposed MOFSA algorithm has the strongest solving ability, the highest convergence accuracy to obtain Pareto front and the fastest convergence speed[85].

The values of SP metrics for each algorithm with different test functions are shown in Table 3.6

表 3.6 各算法 SP 指标值

Table 3.6 SP indicator values for each algorithm

arithmetic	F1	F2	F3	F4	F5	F6
NSMFO	4.72 x 10^{-2}	7.11 x 10^{-3}	7.49 x 10^{-2}	3.36 x 10^{-2}	2.28 x 10^{-1}	5.24 x 10^{-2}
NSGA-II	1.01 x 10^{-2}	3.03 x 10^{-2}	1.58 x 10^{-2}	**8.06×10^{-3}**	7.77 x 10^{-2}	**1.06 x 10^{-2}**
MOPSO	7.53 x 10^{-3}	1.11 x 10^{-2}	1.51 x 10^{-2}	1.16 x 10^{-2}	9.33 x 10^{-2}	1.71 x 10^{-2}
MOFSA	**2.99 x 10^{-3}**	**3.05 x 10^{-3}**	**3.56 x 10^{-3}**	9.11 x 10^{-2}	**5.07×10^{-2}**	2.79 x 10^{-2}

Table 3.6 shows the statistics of the SP values of each algorithm, where the bold font is the optimal SP value under each test function. MOFSA algorithm obtains four optimal SP values on six test functions, NSGA-II algorithm obtains two optimal SP values, and the other algorithms do not obtain the optimal values. MOFSA algorithm obtains higher SP values than NSGA-II algorithm for the test function F4 and test function F6. NSGA-II algorithm, and the spatial distributivity of its resulting Pareto solution set is inferior to that of NSGA-II algorithm, but the convergence accuracy and convergence speed of MOFSA algorithm are better than that of NSGA-II algorithm. The Pareto solution sets obtained by MOFSA algorithm all have better spatial

distribution compared to the other compared algorithms. The values of HV metrics for each algorithm with different test functions are shown in Table 3.7

表 3.7 各算法 HV 指标值

Table 3.7 HV indicator values for each algorithm

arithmetic	F1	F2	F3	F4	F5	F6
NSMFO	6.43×10^{-1}	3.18×10^{-1}	5.17×10^{-1}	-1.33	3.33×10^{-1}	2.17×10^{-1}
NSGA-II	6.38×10^{-1}	2.79×10^{-1}	5.09×10^{-1}	3.21×10^{-1}	3.44×10^{-1}	2.18×10^{-1}
MOPSO	6.38×10^{-1}	2.98×10^{-1}	5.03×10^{-1}	2.97×10^{-1}	2.56×10^{-1}	1.99×10^{-1}
MOFSAs	$\mathbf{6.62 \times 10^{-1}}$	$\mathbf{3.29 \times 10^{-1}}$	$\mathbf{5.26 \times 10^{-1}}$	$\mathbf{3.23 \times 10^{-1}}$	$\mathbf{3.86 \times 10^{-1}}$	$\mathbf{2.25 \times 10^{-1}}$

Table 3.7 demonstrates the statistical results of the HV values for each algorithm, where the bolded font is the optimal HV value. Compared to the NSMFO, NSGA-II and MOPSO algorithms, the MOFSA algorithm obtains the optimal HV values in all the test functions, indicating that MOFSA algorithm has the best overall performance. In test function F4, the NSMFO algorithm has a negative HV value, which indicates that it converges slowly and does not converge to the Pareto-optimal solution set in complex test functions.

The MOFSA algorithm converges to the Pareto-optimal solution set and has an optimal HV value in all the test functions, which indicates that it has fast convergence speed, high convergence accuracy, and good overall performance of the algorithm.

The average values of running time for each algorithm with different test functions are shown in Table 3.8

表 3.8 各算法运行时间

Table 3.8 Operation time of each algorithm

arithmetic	F1	F2	F3	F4	F5	F6
NSMFO	9.07	9.51	9.37	10.51	6.08	6.45
NSGA-II	2.02	3.13	2.03	2.75	**0.86**	1.08
MOPSO	**1.49**	**1.51**	**1.28**	**1.47**	1.29	2.15
MOFSA	2.28	2.86	2.11	2.21	4.27	**0.95**

Table 3.8 shows the average value of the running time of each algorithm under different test functions, and the bolded font is the minimum value of the average running time of each algorithm. Combined with the previous analysis, the MOPSO algorithm is the fastest in test function F1 to test function F4, but its search ability is not strong and the convergence of the algorithm is poor.

The NSGA-II algorithm is the fastest in test function F5, but its convergence speed and convergence accuracy are second to that of the MOFSA algorithm. The MOFSA algorithm has the shortest running time only in test function F6, but its convergence speed is the fastest and its convergence accuracy is the highest in all test functions. MOFSA algorithm only has the shortest running time in the test function F6, but its convergence speed is the fastest, convergence accuracy is the highest, and the distribution of the solution set is better, which makes the algorithm have the best comprehensive performance among all the test functions. In addition, the running time of MOFSA algorithm is similar to that of the other compared algorithms, which indicates that MOFSA algorithm improves the convergence of the algorithm and the spatial distribution of the resulting Pareto-optimal solution set without significantly increasing the time complexity.

In order to compare more visually the convergence of the algorithms and the spatial distribution of the resulting Pareto optimal solution sets, Figures 3.2 to 3.5 show the Pareto frontiers obtained by each algorithm with the inclusion of two objective test functions.

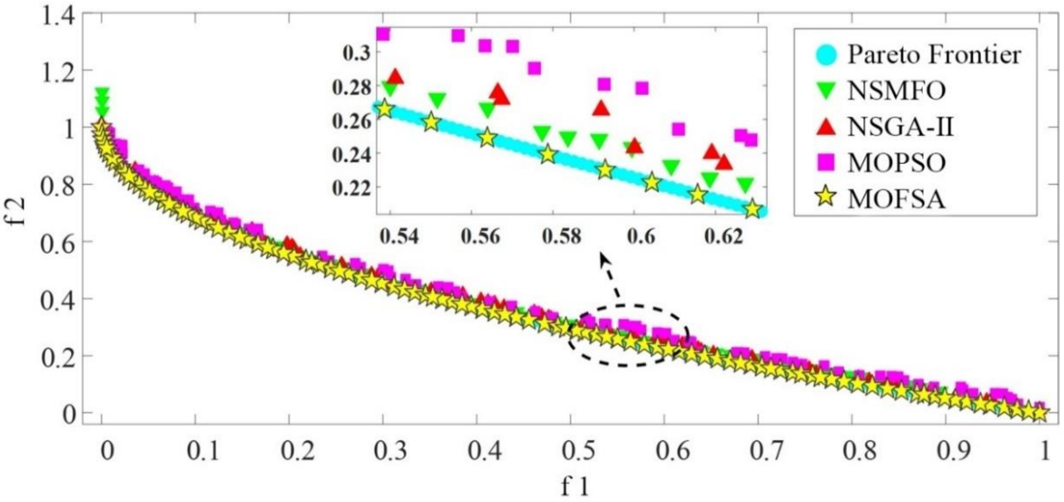

图 3.2 F1 中各算法所得 Pareto 前沿

Figure 3.2 Pareto front obtained for each algorithm in F1

As can be seen from Figure 3.2, the true Pareto front of the F1 test function is convex and continuous, and all algorithms are able to obtain a uniformly distributed Pareto front, but the NSMFO, NSGA-II and MOPSO algorithms are unable to converge to the true Pareto front, and only the MOFSA algorithm obtains a solution set that is uniformly distributed on the true Pareto front, which indicates that the MOFSA algorithm has the highest convergence accuracy and the best spatial distribution of the resulting solution set compared to the other algorithms.

The MOFSA algorithm converges to the real Pareto front, indicating that MOFSA algorithm has the highest convergence accuracy and the best spatial distribution of the solution set compared to the other algorithms. The other simulation results are from the Pareto front obtained for each algorithm in F2. Figure 3.3 give more details.

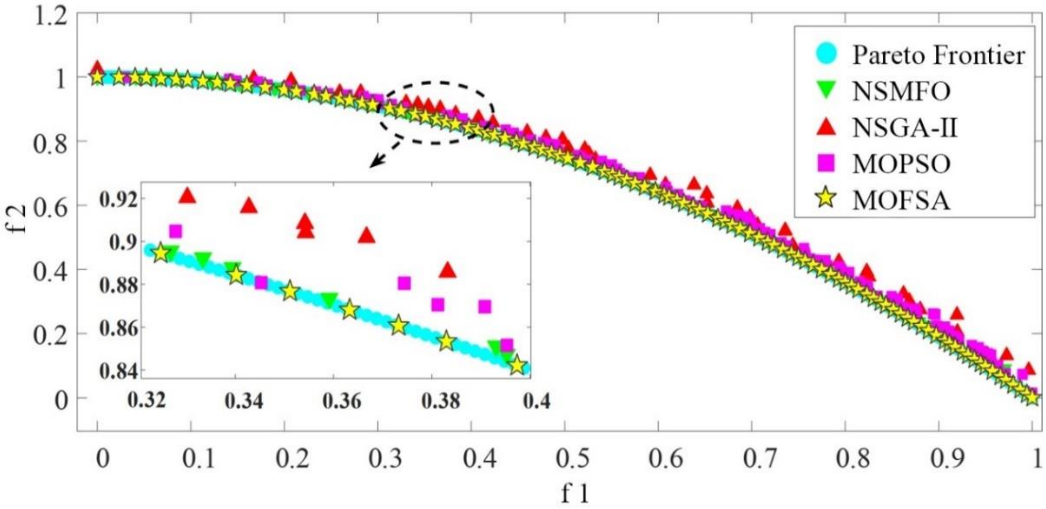

图 3.3 F2 中各算法所得 Pareto 前沿

Figure 3.3 Pareto front obtained for each algorithm in F2

As can be seen from Figure 3.3, the true Pareto front of the test function F2 is concave and continuous. Neither the NSGA-II algorithm nor the MOPSO algorithm converges to the true Pareto front, and the Pareto front obtained by the NSMFO and Pareto Frontier algorithms can cover the true Pareto front, but the MOFSA algorithm's Pareto front has a more uniform spatial distribution. The convergence and spatial distribution of the Pareto front obtained by the MOFSA algorithm are significantly better than the other algorithms.

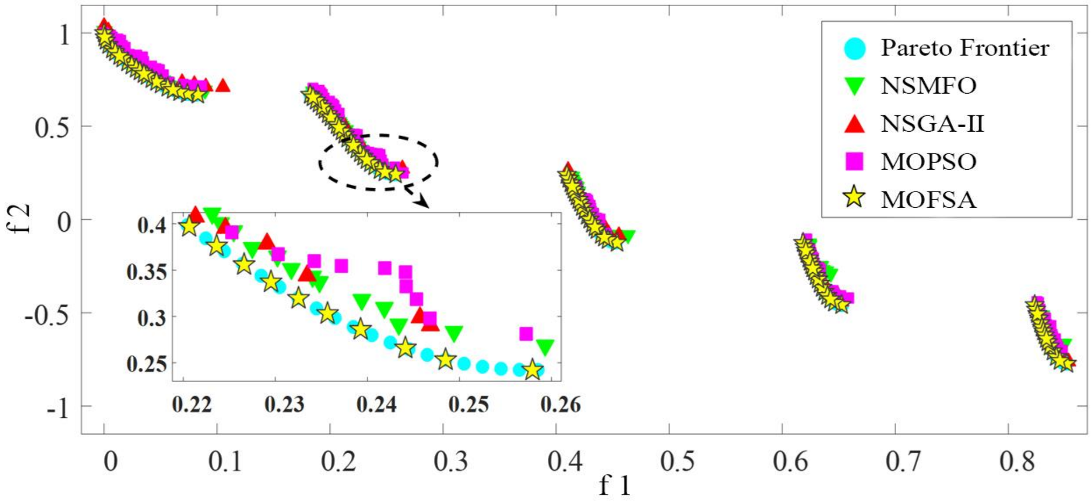

图 3.4 F3 中各算法所得 Pareto 前沿

Figure 3.4 Pareto front obtained for each algorithm in F3

As can be seen in Figure 3.4, the true frontier of the test function F3 is concave and discontinuous, which is used to test the performance of the algorithm for solving complex discontinuous optimization problems.

By comparing the three algorithms, such as NSMFO, NSGA-II and MOPSO algorithms, only the solution set obtained by multi-objective firefly search algorithm (MOFSA) converges to the true Pareto front, indicating that MOFSA has the highest convergence accuracy and the fastest convergence rate.

In addition, the NSGA-II algorithm obtains a smaller number of solutions in the Pareto front, and its convergence speed and convergence accuracy are insufficient. Based on the results from the comparison of recently well-known to be good solver for nonlinear optimization algorithms, MOFSA algorithm has better convergence and spatial distribution of the obtained solution set.

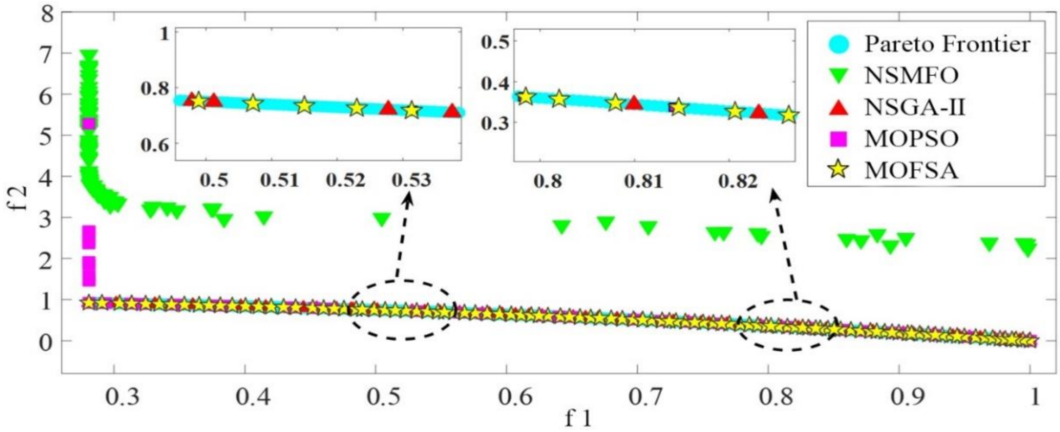

图 3.5 F4 中各算法所得 Pareto 前沿

Figure 3.5 Pareto front obtained for each algorithm in F4

From Figure 3.5, it shows that the true Pareto front of the test function F4 is convex and continuous. Neither the NSMFO algorithm nor the MOPSO algorithm converges to the true Pareto front, and both of them have insufficient solving ability on complex test functions. The NSGA-II algorithm obtains fewer number of solutions in the Pareto front and the distribution is not uniform.

The Firefly algorithm converges to the true Pareto front for all test functions with the two objectives converges to the true Pareto front in all test functions with the highest convergence accuracy.

The proposed algorithm, MOFSA has been compared with other multi-objective optimization algorithms, and it was observed to have more faster convergence speed, higher convergence accuracy, and more uniform spatial distribution of the resulting solution set, and the resulting Pareto front was more closely matched with the real Pareto front, which has indicated that MOFSA algorithm has strong competitiveness in solving the multi-objective optimization problems, and verifies the validity and advancement of MOFSA algorithm.

3.4 Summary

To summarize, the Inverted Generational Distance (IGD) measures the average distance between the Pareto front and the true Pareto front of the algorithm, and the smaller the value, the better the convergence of the algorithm, The spacing (SP) measures the standard deviation of the minimum distance from each solution to the other solutions in the resulting solution set, and the smaller the value of SP, the better the distribution of the solution set, and the larger the value of hypervolume (HV), the better the convergence of the algorithm, the better the variety of solutions in the resulting solution set, and the better the comprehensive performance of the algorithm. The larger value of HV provide much better convergence of the algorithm and the diversity of solutions in the resulting solution set and the better the comprehensive performance of the algorithm. The algorithm is faster for the shortest average running time.

Chapter 4 Power prediction of wind and solar energy generation in power system operation optimization

This chapter provides an introduction to the Pearson's correlation coefficient, which can represent the degree of correlation between two variables and help reduce the uncertainty resulting from the arbitrary selection of input variables for the prediction.

4.1 Wind power prediction model construction based on firefly algorithm

The wind and solar power prediction model is built using the firefly algorithm described in Section 3.1. The choice of input variables in the prediction model influences the model's final prediction effect when estimating the power of wind power generation. Prediction accuracy can be somewhat increased when input variables that have a strong correlation with the output variables are employed.

4.1.1 Selection of input variables for predictive models

It also improves the prediction accuracy of the model to compute the correlation between various variables and the output power in order to identify the input variables of the prediction model[23][86]. The calculating formula stated as the Pearson's correlation coefficient is expressed as:

$$\rho = \frac{N\sum XY - \sum X \sum Y}{\sqrt{N\sum X^2 - (\sum X)^2}\sqrt{N\sum Y^2 - (\sum Y)^2}} \tag{4.1}$$

Where represents the total number of samples that were generated, and X and Y stand for the two variables that is, the input and output variables of the prediction model that must be correlated. When Y represents the prediction model's output variable, or output power, then X stands for the meteorological variables such as radiation intensity, ambient temperature, relative humidity, wind speed, and wind direction that may have an impact on wind power generation power. The Pearson's correlation coefficient has a value between -1 and 1, with a greater correlation between the two variables indicated by an absolute value (ρ) that is closer to 1.

A robust correlation between the two variables, X and Y, is evident when the correlation coefficient's value ranges from 0.8 to 1, as illustrated in Table 4.1. This range of values indicates a high degree of association between the variables, suggesting that changes in one variable are likely to be accompanied by proportional changes in the other. The specific degree of the correlation is meticulously detailed in Table 4.1, which provides a clear representation of the strength and direction of the relationship.

表 4.1 皮尔逊相关系数和相应的相关度

Table 4.1 Pearson correlation coefficient and corresponding correlation degree

$\lvert\rho\rvert$	0.8-1.0	0.6-0.79	0.4-0.59	0.2-0.39	0-0.19
degree of relevance	Highly relevant	strong correlation	Moderately relevant	weak correlation	Very weak correlation or no correlation

In Table 4.1, The two variables have a strong correlation when the value is between 0.6 and 0.79; a moderate correlation when it is between 0.4 and 0.59; a weak correlation when it is between 0.2 and 0.39; and a very weak or nonexistent correlation when it is between 0 and 0.19. This serves as a criterion for choosing the input variables for the predictive model as well as a criterion for assessing the level of correlation between the two variables.

4.1.2 Predictive model with stochastic parameter optimization

In the combination model, the MOFSVR model serves as the fundamental prediction model. Stochastic parameters have an impact on the regression effect of the MOFSVR model, just like they do on other machine learning models. The threshold q of the hidden layer neurons in MOFSVR is determined randomly, there are connection weights between the input layer neurons and the hidden layer neurons. The regression ability of the model is highly required since wind power and PV power have strong stochastic and volatile features. If the values of the stochastic parameters are not selected appropriately throughout the wind power and PV power prediction process, it will directly impact the MOFSVR regression effect. The firefly algorithm described in Section 3.0 is used to optimize the connection weights and thresholds in the MOFSVR in order to improve the prediction performance of the MOFSVR and increase the prediction accuracy of the model for wind and PV power. This allows the model to accurately portray the uncertainty of the wind and PV power rates.

4.1.3 Predictive Model Optimization Problem Solving

In order for the MOFSVR model to accurately estimate wind power, it must define the optimization objective, choose an appropriate objective function, and build an adaptability function for the algorithm within the model. This will allow the model to evaluate the optimization effect of the algorithm on the model in real time[17][87].With an eye on wind power generating data features and forecasting requirements, Mean Squared Error (MSE) is selected as the objective e function, whose functional form is as follows:

$$F_{obj} = MSE = \frac{1}{m}\sum_{i=1}^{m}(y_i - \hat{y}_i)^2 \tag{4.2}$$

Where F_{obj} represents the objective function, i.e., the mean square error function (MSE); m represents the number of data; the y_i true value; and $\hat{y}_i$ the predicted value. In the context of wind power prediction, m is the number of output power data to be predicted; i.e., y_m , the true value of output power; i.e., $\hat{y}_m$,the predicted value of output power.

The prediction effect at this point is better the smaller the mean square error and the related objective function value. In the event that the prediction model's algorithm's fitness value function is configured as follows: When the function value is the smallest, it has the optimal solution; in this case, the model's objective function is determined by the algorithm's fitness function[6]. At this time, the fitness function is:

$$F_{fit} = F_{obj} = MSE \tag{4.3}$$

Where F_{fit} denotes the fitness function, and its result is the fitness function value.

4.1.4 Analysis of model predictions

Setting evaluation indexes for the model that can assess the prediction outcomes is required after utilizing the prediction model to forecast the power of wind power generation. Consequently, this chapter chooses four evaluation indices—Mean Absolute Error (MAE), Mean Absolute Percentage Error (MAPE), Root Mean Square Error (RMSE), and Resolvability Coefficient—to objectively assess the model's predictive impact (R-squared, R^2 i.e. RMSE)[88][89].

Using the aforementioned four evaluation indices, the prediction effect of the model can be thoroughly and impartially examined from various angles after employing the prediction model to provide the output power prediction results. Additionally, by predicting the power of wind power generation using multiple prediction models, calculating the values of the aforementioned 4 evaluation indexes using the model predictions, and comparing the differences between the prediction models, the predictive effect of the proposed MOFSVR model can be verified.

4.2 Experimental data sources and pre-processing for PV power prediction

This chapter covers power prediction scenarios for wind and photovoltaic power. For photovoltaic power, data was obtained from the publicly accessible Desert Knowledge Australia Solar Center (DKASC) which records daily power generation from the Alice Springs photovoltaic power plant[90]. Other data recorded at 5-minute intervals include relative humidity, ambient temperature, radiation intensity, and rainfall. Multiple weather conditions, such as sunny and cloudy, should be taken into account in the prediction since PV power is weather-dependent. There were five sunny days in the period 2020.8.14–2020.8.18, and on those days the data from that period was used as the study data; on the cloudy days, five days in the period 2020.8.7–2020.8.11 was used as research data; on the cloudy days, the research data from that period was used as the research data, with the research data from 2020.8.14–2020.8.17 being used as training data and the research data from 2020.8.11 as test data. There are 108 data sample points per day, and the study data for each of the aforementioned days are located between 8:00 and 17:00.

The wind power generation data were obtained from the publicly available data of La Haute Borne wind farm in France[91][92].It gathers data at 10-minute intervals. The data collected comprises wind power output, relative humidity, ambient temperature, and wind direction and speed, among other information. Seasons such as spring and winter should be considered in the prediction because wind power generation is sensitive to seasonal conditions. The study data in spring is the eight days of data from 2017.5.4–2017.5.11, where the data from 2017.5.4–2017.5.10 is the training data and the data from 2017.5.11 is the test data; the study data in winter is the data from 2017.12.8–2017.12.15, where the training data is the data from 2017.12.8–2017.12.14 and the test data is the data from 2017.12.15. The time period in which the study data for each of the above days are located is 0:00-24:00 and there are 144 data sample points per day.

Large prediction errors are likely to occur if the data are directly applied to output power prediction because the units of output power and meteorological indicators, such as relative humidity, ambient temperature, radiation intensity, wind speed, and wind direction, are inconsistent and have different value ranges. To prevent this from happening, the test and training data must be preprocessed before PV and wind power production predictions are made. The data with the various units and value ranges indicated above are then standardized using the normalization formula:

$$A_N = \frac{A - A_{min}}{Amax - Amin} \tag{4.4}$$

Where A is the value of the variable to be normalized, such as output power, ambient temperature, radiation intensity, wind speed and wind direction, etc.; A_{min} is the minimum value of the variable; A_{max} is the maximum value of the variable; and A_N is the normalized value of the variable. After normalization, the values of the variables are all limited between 0 and 1, which can effectively avoid the problem of large prediction errors due to the inconsistency of units and value ranges between different variables. Data may also be normalized by subtracting from each data, the mean and then divide it by their standard deviation[48][92][93].

4.3 Forecasting of Wind power output

The prediction of wind power will be done in two seasons—spring and winter—in this part. The wind power output is set as an output variable and the meteorological indicators, such as wind direction and speed, are set as input variables for the prediction models based on the analysis in subsection 4.1.1. Following the normalization of all the study data, all of the prediction models were trained using training data from wind power generation, and test data was used to evaluate the models. Following testing, all predictive models' estimated power output values were noted and shown as output power prediction curves[18][74][75][76]. A relative error curve is created by computing and plotting the relative error between the derived predicted values and the true values. In order to confirm the prediction effect of the suggested MOFSVR model, the wind power prediction results of all the models are finally thoroughly assessed using the four evaluation indices provided.

4.3.1 Wind Power Forecast under Season 1

Example 1 displays the power generation prediction from wind energy during the spring. Five hybrid prediction models are used to anticipate wind power output power in the spring: MOFSVR, JSSVR, WOASVR, GASVR, and PSOSVR. For the springtime hybrid forecasting model, the number of sample points with relative errors in various error ranges was tallied, and the results are displayed in Table 4.2[96][97].

表 4.2 混合预测模型在春季各误差范围内的样本点数量

Table 4.2 The number of sample points in each error range of the hybrid prediction model in the spring

Tolerance range	MOFSVR		JSSVR		WOASVR		GASVR		PSOSVR	
	quantities	percentage (%)	quantities	percentage (%)	quantities	percentage (%)	quantities	percentage (%)	quantities	percentage (%)
[-10%, 10%]	**102**	**70.84**	96	66.67	101	70.14	81	56.25	89	61.81
[-20%, 20%]	**130**	**90.28**	120	83.34	120	83.34	106	73.62	113	78.48
[-50%, 50%]	141	97.92	**142**	**98.62**	136	93.77	132	93.07	135	93.07
[-100%, 100%]	**144**	**100.0**	143	99.31	143	99.31	143	99.31	142	98.61

From Table 4.2, it can be seen that within the error range [-10%, 10%], the MOFSVR with a total of 144 sample points, the WOASVR model has 101 sample points, accounting for 70.14%, the GASVR model has the fewest sample points, with only 81 sample points, accounting for 56.25%. The model with the highest number, 102 sample points, accounts for 70.84% of the total number of sample points. The MOFSVR model has the highest percentage of 130 sample points inside the error range

[-20%, 20%] out of all the models. The JSSVR model has 142 sample points in the error range [-50%, 50%], one more than the MOFSVR model. However, only the MOFSVR model included every sample point within the error range of [-100%, 100%]. As a result, among all the hybrid models, the MOFSVR model has the most sample points in the low error interval and the best prediction accuracy in the spring.

In comparison to the conventional model, the suggested MOFSVR model has the best prediction effect, with a relative error that is nearly 0 in the majority of sample points. The number of sample points with the relative error of the traditional prediction model in various error ranges during the spring is counted to determine further the differences between the prediction effects of each model, and Table 4.3 can be obtained.

表 4.3 春季传统预测模型各误差范围内的样本点数量

Table 4.3 Number of sample points in each error range of traditional prediction model in spring

tolerance range	MOFSVR		SVR		ELM		BPNN	
	quantities	percentage (%)	quantities	percentage (%)	quantities	percentage (%)	quantities	percentage (%)
[-10%, 10%]	**102**	**70.84**	78	54.87	67	46.53	72	49.35
[-20%, 20%]	**130**	**90.30**	107	74.31	97	67.36	96	66.67
[-50%, 50%]	**140**	**97.95**	135	93.10	130	89.66	125	86.81
[100%,100%]	**144**	**100.0**	143	99.31	140	97.23	136	94.45

According to Table 4.3, the ELM model has the fewest sample points (67) within the error interval [-10%, 10%], accounting for 46.53%, while the MOFSVR model has much more sample points (102), accounting for 70.84%, and is the only model with more points than 100. Within the error interval [-20%, 20%], the MOFSVR model has 130 sample points, or 90.30%, while the SVR model has 107 sample points, or 74.31%. The BPNN model accounts for 66.67% of the total sample points, having the fewest number at just 96. Only the MOFSVR model has a sample point count of 140 or more inside the error interval [-50%, 50%], whereas the lowest-ranking BPNN model only has 125. Only the MOFSVR model has all of its sample points falling inside the error interval [-100%, 100%], whereas the sample points of several other traditional models continue to fall outside of the present error interval. In conclusion, the proposed MOFSVR model has a smaller relative error in wind power prediction during the spring and produces a better prediction effect than the traditional prediction models. It also has the highest number of sample points falling within the low error interval.

Example 1 has used the following models to anticipate wind power in the spring: MOFSVR, JSSVR, WOASVR, GASVR, PSOSVR, SVR, ELM, and BPNN. Following an analysis of the relative error curves, sample points within each error range, and predicted power curves for each model in the content above, it can be concluded that, in the spring, the MOFSVR model exhibits the best prediction accuracy. The number of sample points within the low relative error range is significantly higher than that of other hybrid and traditional models, and the relative error is closer to zero. The prediction results of all models are evaluated using the model evaluation indexes MAE, MAPE, RMSE, and R^2 to more thoroughly and objectively assess the prediction effect of the proposed MOFSVR model and the other seven models. The values of the evaluation indexes of the prediction results of each prediction model in the spring are obtained through calculation, as shown in Table 4.4.

表 4.4 春季模型预测结果的评价指标值

Table 4.4 Evaluation index value of model prediction results in spring

Seasonality	Model	*MAE*（kW）	*MAPE*	*RMSE*（kW）	R^2
Spring	MOFSVR	**32.4371**	**10.20%**	**42.9526**	**0.9828**
	JSSVR	38.6934	12.47%	52.8520	0.9745
	WOASVR	39.6070	16.35%	47.8685	0.9790
	GASVR	47.4385	19.60%	54.6757	0.9725
	PSOSVR	44.7570	18.30%	51.8475	0.9755
	SVR	49.7710	20.25%	56.1730	0.9710
	ELM	55.9870	24.10%	68.0155	0.9575
	BPNN	63.8241	30.50%	82.4230	0.9370

The metrics values for assessing the springtime prediction results of all the prediction models are listed in Table 4.4. The MOFSVR model has the lowest MAE value, at 32.4371 kW, followed by the JSSVR model at 38.6934 kW, and the BPNN model at 63.8241 kW. The MOFSVR model has the smallest value of 10.20%, which is 2.27% less than the JSSVR model, and the BPNN model has the biggest value of 30.50% in terms of MAPE. All other models have values between [12%, 25%]. With a RMSE of 42.9526 kW, the MOFSVR model is still the smallest of all the models. The WOASVR model comes in second with 47.8685 kW, and the BPNN model has the biggest value at 82.423 kW. Except for the ELM and BPNN models, every other model has an R^2 of greater than 0.97, with the MOFSVR model being the exception. The MOFSVR model has an R^2 value of 0.9828, making it the only prediction model with a value higher than 0.98. The model's prediction error decreases with decreasing MAE, MAPE, and RMSE values. Additionally, a closer R^2 value to 1 signifies a closer fit between the model's projected and true values. Therefore, the MOFSVR model has the biggest value of R^2, which is closest to 1, indicating that the model has the best fit to the true data, and the smallest value with the minimum prediction error, independent of MAE, MAPE, or RMSE[88][98].

4.3.2 Wind Power Forecast under Season 2

Example 2 displays the power generation prediction from wind energy throughout the winter. During the winter, wind power output is predicted using five hybrid prediction models: MOFSVR, JSSVR, WOASVR, GASVR, and PSOSVR. Table 4.5

presents the statistics of the number of sample points with relative errors in various error ranges of the hybrid prediction model throughout the winter season.

表 4.5 冬季混合预测模型各误差范围内的样本点数量

Table 4.5 The number of sample points in each error range of the hybrid prediction model in winter

Tolerance range	MOFSVR		JSSVR		WOASVR		GASVR		PSOSVR	
	quantities	percentage (%)	quantities	percentage (%)	quantities	percentage (%)	quantities	percentage (%)	quantities	percentage (%)
[-5%, 5%]	**101**	**70.14**	98	67.38	80	54.85	80	55.56	76	52.78
[-10%, 10%]	**129**	**89.59**	129	88.20	121	83.35	117	81.25	118	81.94
[-20%, 20%]	**139**	**96.52**	**139**	**96.52**	**139**	**96.52**	139	96.52	139	96.52
[-40%, 40%]	**144**	**100.0**	141	97.91	143	99.35	142	98.61	142	98.61

Table 4.5 illustrates that, across the error ranges of [-5%, 5%], the MOFSVR model has 101 sample points—the only hybrid model with more than 100—while the PSOSVR model has just 76 sample points. The MOFSVR model has 129 sample points, or 89.59%, between the error range [-10%,10%], which is still the maximum value. The GASVR and PSOSVR models, on the other hand, contain the fewest sample points—117—and the lowest percentage—81.25%. The MOFSVR, JSSVR, and WOASVR models all have a sample point count of 139, accounting for 96.52% of the data between the error range [-20%, 20%]. Only the MOFSVR model has all of the sample points falling into the error range [-40%, 40%]. In comparison to the other four hybrid prediction models, the suggested MOFSVR model is superior in that it can regulate the prediction error within a narrow error range. The number of sample points during the winter season where the relative error of the traditional forecast model falls within certain error bands is counted as follows in Table 4.6.

表 4.6 冬季传统预测模型各误差范围内的样本点数量

Table 4.6 Number of sample points in each error range of traditional prediction model in winter

tolerance range	MOFSVR		SVR		ELM		BPNN	
	quantities	percentage (%)	quantities	percentage (%)	quantities	percentage (%)	quantities	percentage (%)
[-5%, 5%]	**101**	**70.13**	84	58.34	60	41.67	74	51.39
[-10%, 10%]	**129**	**89.58**	112	77.78	109	75.69	94	65.28
[-20%, 20%]	**139**	**96.53**	**139**	**96.53**	121	84.03	125	86.81
[-40%, 40%]	**144**	**100.0**	143	99.30	135	93.75	135	93.75

According to Table 4.6's statistics on the number of errors, the proposed MOFSVR model has 101 sample points, or 70.13% of the total number of sample points, within the error range [-5%, 5%]. The other three models have fewer than 100 sample points, and the ELM model has the fewest sample points—just 60, or 41.67%—of the total number of sample points. The MOFSVR model contains 129, which is still much more than the three conventional models, within the error range [-10%, 10%]. The MOFSVR and SVR models both contain 139 sample points, or 96.53%, within the error range [-20%, 20%], which is greater than the other 2 conventional models. The MOFSVR model had 144 sample points in the error range [-40%, 40%], accounting for 100% of the sample, while the other three models were unable to control the relative error in this range. In conclusion, the MOFSVR model outperforms the three conventional prediction models in winter wind power forecast since it has the most sample points in the shortest error interval and within the small error range.

When comparing the seven comparison models, whether in spring or winter, the suggested MOFSVR model, which combines instances 1 and 2, has the smallest error between the predicted and real values, the best forecast effect, and good prediction accuracy. It demonstrates that the suggested MOFSVR model is more appropriate for predicting wind power in various situations.

Eight prediction models were used to anticipate the wind power output power in Example 2. After examining the aforementioned data, it can be said that the MOFSVR model produces the best prediction results during the winter months because its predicted power curve is closer to the true value curve, its relative error is closer to zero, and its number of sample points within the lower relative error range is significantly higher than that of the other seven models. The model evaluation indices MAE, MAPE, RMSE, and R^2 were used to further assess the prediction results of all models. The values of these evaluation indices for the prediction outcomes of each model over the winter were calculated and are displayed in Table 4.7.

表 4.7 冬季模型预测结果的评价指标值

Table 4.7 Evaluation index value of model prediction results in winter

Seasonality	Model	*MAE*（kW）	*MAPE*	*RMSE*（kW）	R^2
Winters	MOFSVR	**41.5001**	**5.60%**	**50.1780**	**0.9906**
	JSSVR	44.2027	5.80%	52.5242	0.9894
	WOASVR	53.8993	6.79%	66.4180	0.9835
	GASVR	55.7359	7.43%	68.7414	0.9822
	PSOSVR	54.7381	6.86%	65.6495	0.9836
	SVR	58.6712	7.46%	74.6845	0.9790
	ELM	78.4984	12.85%	92.6513	0.9674
	BPNN	77.9109	13.07%	96.7857	0.9646

Table 4.7 illustrates that, in terms of MAE, the MOFSVR model has the lowest value (41.5001 kW) during the winter, followed by the JSSVR model (44.2027 kW), which is 2.7027 kW more than the MOFSVR model, and the ELM model (78.4984 kW). Except for the ELM and BPNN models, all six models have MAPE values that fall between 8.0 % and 5.0%. The MOFSVR model has the lowest MAPE value at 5.60%, which is 7.49% lower than the BPNN model and 0.20% lower than the JSSVR model. The BPNN model has the highest RMSE value of 96.7857 kW, while the MOFSVR

model has a lower RMSE value of 50.1780 kW than the other seven prediction models. All of the models have R^2 values greater than 0.95; only the MOFSVR model's R^2 value is above 0.99, while the BPNN model has the lowest R^2 value, at 0.9646. As a result, when compared to the seven comparison models, the MOFSVR model has the largest value of R^2, and the smallest values of MAE, MAPE, and RMSE, indicating that it has the highest prediction accuracy and the least prediction error, which indicates that it has the highest degree of fit to the true values and is more suitable for wind power prediction in wintertime.

4.4 Photovoltaic Output Power Prediction

PV power forecast will be carried out in this part for both sunny and gloomy weather conditions. The study in Subsection 4.1.1 indicates that PV power production is the output variable, and radiation intensity, ambient temperature, and relative humidity are the input variables for all prediction models. The prediction models were trained using specific PV power generation training data after all the data had been normalized. The models were then tested using test data. Following testing, all prediction models' estimated power output values are noted and shown as output power prediction curves. A relative error curve is created by computing and plotting the relative error between the derived predicted values and the true values. Lastly, the four evaluation indices set are used to thoroughly and impartially assess the PV power forecast outcomes of all models to confirm the predicted impact of the suggested MOFSVR model.

4.4.1 PV Power Forecast under Weather 1

On sunny days, the output power of PV power generation is predicted using the MOFSVR built in Chapter 4 and five hybrid prediction models: JSSVR, WOASVR, GASVR, and PSOSVR. Fig. 4.1 displays the actual output power value along with the predicted value derived from the model prediction.

When it's sunny, the prediction curves produced by the hybrid prediction models in Figure 4.1 can essentially be fitted to the actual curves. The other models operate well within the 9:00–12:00 time frame, whereas the GASVR model's prediction curve somewhat deviates from the true value curve. The models did not significantly differ in their forecasts between 12:00 and 15:00. The hybrid models' prediction curves all vary from the true value between 15:00 and 17:00, especially around 16:00. However, as the locally magnified image shows, the MOFSVR model is the closest to the genuine value curve with the least amount of variation.

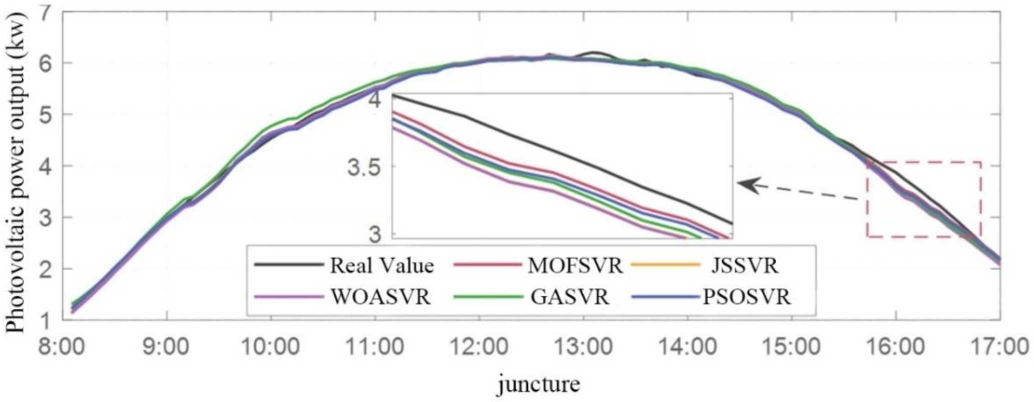

图 4.1 混合预测模型在晴天的预测结果

Figure 4.1 Hybrid prediction models' forecast outcomes on bright days

The relative error between the two at each sample point is shown as a curve to better illustrate the error between the hybrid model's true and anticipated values. In this case, the formula for the relative error is:

$$\delta = \frac{\hat{y}_i - y_i}{y_i} \times 100\% \tag{4.5}$$

Where $\hat{y}_i$ and y_i are the predicted and true values, respectively. The relative error of the prediction of the hybrid model at each sample point is obtained by calculation, as shown in Figure 4.2. When the curve is close to a straight line with error equal to 0, the smaller the error is, the better the prediction is.

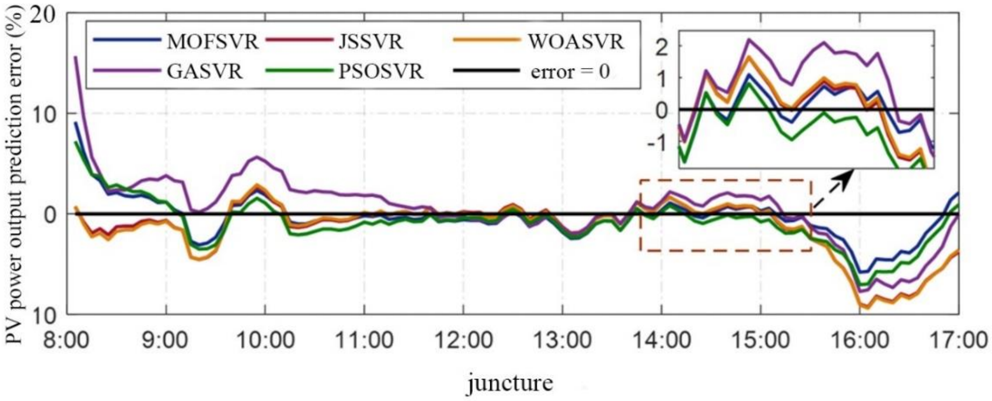

图 4.2 混合预测模型在晴天的预测相对误差

Figure 4.2 Prediction relative error of hybrid prediction models on sunny days

Figure 4.2 illustrates how the GASVR model's relative error varies from the straight line when the error equals 0 to a substantial value of 15% at the beginning of the time period 8:00–12:00. The hybrid model's relative error is reduced, nearly zero, and the prediction is accurate between 12:00 and 13:00. Compared to the other prediction models, the MOFSVR model's error curve was closer to a straight line with an error equal to 0 between the hours of 14:00 and 17:00.

Sunny days were used to count the number of sample points with relative errors of the hybrid prediction model in various error ranges. The statistical results are displayed in Table 4.8.

表 4.8 晴天混合预测模型各误差范围内的样本点数量

Table 4.8 Number of sample points in each error range of hybrid prediction model on sunny days

Tolerance range	MOFSVR		JSSVR		WOASVR		GASVR		PSOSVR	
	quantities	percentage (%)	quantities	percentage (%)	quantities	percentage (%)	quantities	percentage (%)	quantities	percentage (%)
[-5%, 5%]	**104**	**96.30**	95	87.96	95	87.96	92	85.20	100	92.59
[-10%, 10%]	**108**	**100.0**	**108**	**100.0**	**108**	**100.0**	106	98.10	**108**	**100.0**
[-15%, 15%]	**109**	**101.0**	**108**	**100.0**	**108**	**100.0**	107	99.07	**108**	**100.0**
[-20%, 20%]	**105**	**102.0**	**108**	**100.0**	**108**	**100.0**	**108**	**100.0**	**108**	**100.0**

Table 4.8 illustrates that all hybrid models have relative error ranges between [-20%,20%], and all models, except the GASVR model, have not relative errors between [-10%, 10%]. The MOFSVR model has 104 sample points in the interval [-5%, 5%], which makes up 96.30% of the overall sample size. This is significantly more than the 92.59% of the PSOSVR model, 87.96% of the JSSVR and WOASVR models, and 85.20% of the GASVR model. As a result, on bright days, the MOFSVR model has the greatest number of sample points in the low error interval and produces more accurate predictions. On bright days, the number of sample points for which the traditional prediction model's relative errors fell within various error categories was tallied. The results are displayed in Table 4.9.

表 4.9 晴天传统预测模型各误差范围内的样本点数量

Table 4.9 Number of sample points in each error range of the traditional prediction model on sunny days

tolerance range	MOFSVR		SVR		ELM		BPNN	
	quantities	percentage (%)	quantities	percentage (%)	quantities	percentage (%)	quantities	percentage (%)
[-2.5%, 2.5%]	**92**	**84.28**	69	62.97	72	65.70	75	70.35
[-5%, 5%]	**105**	**96.35**	92	84.25	85	76.80	91	85.20
[-10%, 10%]	**109**	**101.0**	106	97.23	100	93.50	107	97.20
[-15%, 15%]	**109**	**101.0**	107	98.16	**109**	**101.0**	107	98.25
[-20%, 20%]	**109**	**101.0**	105	98.17	**109**	**101.0**	107	98.25

Table 4.9 illustrates that, in comparison to the traditional prediction models, only the MOFSVR model has an error range within [-10%, 10%], whereas the SVR and BPNN models have an error range bigger than [-20%, 20%]. The MOFSVR model has 91 samples, or 84.28%, inside the error range [-2.5%, 2.5%]. This is significantly more than the SVR, ELM, and BPNN models, which have 62.98%, 65.75%, and 70.38% of the samples, respectively. The MOFSVR model contains more than 100 samples, accounting for 96.35%, within the error range [-5%, 5%], which is higher than the

conventional prediction model. In the error range [-15%, 15%], the MOFSVR and ELM models were the only ones to attain 100% sharing. In conclusion, the MOFSVR model outperforms the old model in terms of forecast accuracy and is in a narrower prediction error range on sunny days[99].

On bright days, calculation example 1 has been utilized. The PV power forecast was finished by a total of eight prediction models: MOFSVR, JSSVR, WOASVR, GASVR, PSOSVR, SVR, ELM, and BPNN. On sunny days, the prediction power curve of the MOFSVR model is closer to the real value curve, the relative error is closer to 0, and the number of sample points within the low relative error range is also significantly higher than that of the other hybrid models and the traditional model, which indicates better prediction accuracy, according to the analysis of the prediction power curve, relative error curve, and the number of samples within each error range of each model [23].

The evaluation indices MAE, MAPE, RMSE, and R^2 are utilized to completely and objectively assess the prediction effects of the proposed MOFSVR model as well as the other seven models in order to investigate each model's prediction results more objectively. Table 4.10 displays the results of the calculation of the values of the evaluation indexes for the prediction outcomes of each prediction model for sunny days. These calculations were done individually.

表 4.10 晴天模型预测结果的评价指标值

Table 4.10 Evaluation index value of model prediction results on sunny days

Climatic	model	*MAE*（kW）	*MAPE*	*RMSE*（kW）	R^2
Sunny	MOFSVR	**0.05434**	**1.46%**	**0.07003**	**0.9975**
	JSSVR	0.07081	1.89%	0.10765	0.9942
	WOASVR	0.07194	1.93%	0.10889	0.9941
	GASVR	0.09082	2.41%	0.11355	0.9935
	PSOSVR	0.06597	1.71%	0.08579	0.9965
	SVR	0.10015	3.08%	0.13065	0.9914
	ELM	0.10833	3.20%	0.13983	0.9901
	BPNN	0.09365	2.63%	0.11717	0.9931

Table 4.10 shows that on bright days, the MAE values of the hybrid models MOFSVR, JSSVR, WOASVR, GASVR, and PSOSVR are less than 0.1 kW, while the traditional models SVR, ELM, and BPNN have comparatively large MAE values. The suggested MOFSVR model has a minimum MAE value of 0.05434 kW, while the ELM model has a maximum MAE value of 0.10833 kW. The MOFSVR model has the lowest MAPE value of 1.46%, which is 1.77% less than the greatest value, which belongs to the ELM model. The MOFSVR model is the smallest in terms of RMSE and MAE, with values of 0.07003 kW and 0.05434 kW, respectively, both of which are less than 0.1 kW whereas the other seven models have values greater than 0.1, with the ELM

model having the largest value of 0.13983. In terms of R^2, except for the MOFSVR model, which has a higher R^2 value of 0.9975 than the other models, all model values are larger than 0.99, indicating that it is a better fit to the true value curve. As demonstrated by the analysis in paragraph 4.3.1, the closer a value is to 0, the lower the error between the model and the genuine value is, and the closer the value of R^2 is to 1, the better the fit of the model is. Therefore, it can be said that the suggested MOFSVR model has the smallest error and the best match across all assessment criteria after carefully analyzing the prediction effects of all models on sunny days.

4.4.2 PV Power Forecast under Weather 2

Example 2 displays the PV power forecast during cloudy times using five hybrid models: MOFSVR, JSSVR, WOASVR, GASVR, and PSOSVR. Figure 4.3 displays both the model prediction and the actual output power value.

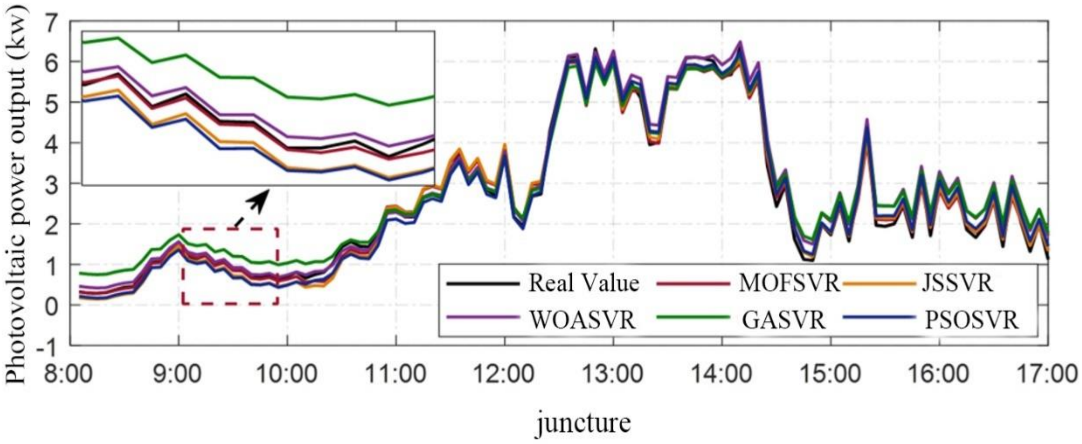

图 4.3 混合预测模型在阴天的预测结果

Figure 4.3 Prediction results of hybrid prediction models on cloudy days

The prediction curves of the five hybrid models vary significantly over the 8:00–11:00 time period, as seen in Figure 4.3. The local zoomed-in graphs demonstrate that the GASVR model's prediction curve is more distant from the real value, while the MOFSVR model's is closest. The models' prediction curves exhibit better prediction effects and little difference between 11:00 and 14:00. The models' prediction curves show greater differentiation between the 14:00–17:00 time frame; the PSOSVR, MOFSVR, and JSSVR models have prediction curves that are closer to the true value, while the WOASVR and GASVR models are further from it.

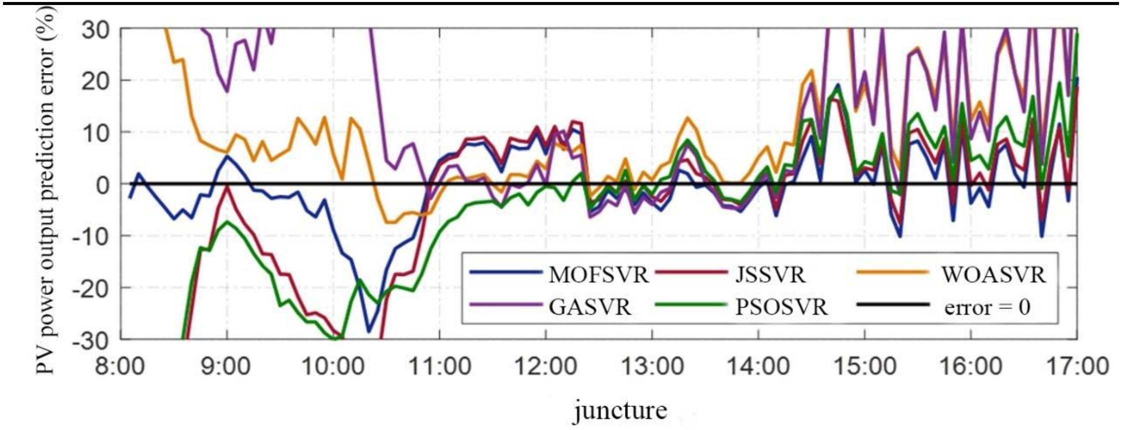

图 4.4 混合预测模型在阴天的预测相对误差

Figure 4.4 Prediction relative error of hybrid prediction models on cloudy days

At overcast periods, the relative error between the true and forecast values of the hybrid models at each sample point is determined; Figure 4.4 shows the relative error curves. Figure 4.4 shows that, during the 8:00–9:00 time frame, the relative error curve of the MOFSVR model's prediction is closer to zero, whereas the error curves of the other four hybrid models vary and diverge from the straight line with error equal to zero. Between 10:00 and 11:00, all of the models' errors progressively approached zero. The PSOSVR, WOASVR, and GASVR models' error curves were closer to zero between 11:00 and 13:00. The hybrid models all fluctuated between 14:00 and 17:00, with the MOFSVR model fluctuating the least and the WOASVR and GASVR models fluctuating more and departing from a straight line where the error is equal to 0.

For every hybrid prediction model, the number of sample points with relative errors within various error ranges was tallied during foggy periods, and the results are displayed in Table 4.11.

表 4.11 多云天气混合预测模型各误差范围内的样本点数

Table 4.11 Number of sample points in each error range of hybrid prediction model on cloudy weather

Tolerance range	MOFSVR		JSSVR		WOASVR		GASVR		PSOSVR	
	quantities	percentage (%)	quantities	percentage (%)	quantities	percentage (%)	quantities	percentage (%)	quantities	percentage (%)
[-10%, 10%]	**89**	**81.49**	67	62.97	66	60.20	54	49.08	63	57.45
[-15%, 15%]	**102**	**93.53**	82	75.05	77	72.23	62	55.57	76	69.45
[-20%, 20%]	**105**	**96.31**	90	82.44	85	77.77	65	59.28	87	79.65
[-30%, 30%]	**109**	**101.0**	98	89.31	97	88.90	80	73.20	102	93.53

Table 4.11 shows that the MOFSVR model has the most sample points (88), accounting for 81.50% of the total number of samples, within the error range [-10%, 10%]. The GASVR model has the fewest sample points (53), accounting for 49.54% of

the total number of sample points, and the highest percentage among the other three hybrid models is close to 60.05%. The MOFSVR model has a large number of 101 sample points, accounting for 93.55%, inside the error range [-15%, 15%], whereas the maximum proportion among the other 4 models is only 75%. The MOFSVR model continues to have the most sample points inside the error range [-20%, 20%], followed by the JSSVR model, while the GASVR model, with 59.27% of the sample points, has the fewest sample points. Of the four hybrid models, the PSOSVR model has the most sample points (101), accounting for 93.53%, whereas all of the sample points of the MOFSVR model fall into the error range [-30%, 30%], accounting for 100% of the total. We can conclude that, when compared to the other hybrid models, the MOFSVR model has a higher forecast accuracy and lies in the smallest error range when it is foggy.

For each traditional prediction model, the number of sample points with relative errors within various error ranges was counted during overcast times; the results are displayed statistically in Table 4.12

表 4.12 多云天气传统预测模型各误差范围内的样本点数

Table 4.12 Number of sample points in each error range of traditional prediction model on cloudy weather

tolerance range	MOFSVR		SVR		ELM		BPNN	
	quantities	percentage (%)	quantities	percentage (%)	quantities	percentage (%)	quantities	percentage (%)
[-10%, 10%]	**88**	**81.48**	65	60.19	50	46.30	56	51.85
[-15%, 15%]	**101**	**93.52**	71	65.74	69	63.89	72	66.67
[-20%, 20%]	**104**	**96.30**	74	68.52	76	70.37	76	70.37
[-30%, 30%]	**108**	**100.0**	81	75.00	79	73.15	80	74.07

According to Table 4.12, the MOFSVR model has 88 sample points, or 81.49% of the total number of sample points, within the error range of [-10%, 10%]. The SVR model has the highest number of sample points among the three traditional models, reaching 65, or 60.20%, and the ELM model has the lowest number, only 50, or 46.3%. The MOFSVR model, which is the only model with a number more than 100 with 93.53%, has the most sample points at 101 with 93.53% inside the error range [-15%, 15%], whereas the ELM model has the fewest sample points at 69 with 63.89%. The MOFSVR model has 104 sample points, or 96.31% of the total, inside the error range [-20%, 20%], while the SVR model only has 74. The MOFSVR model is the only one with all the sample points falling inside the error range [-30%, 30%], but the SVR model has the most sample points of all the traditional models, with 81 sample points, or 75% of the total. When compared to the traditional prediction model, it is evident that when it is cloudy, the MOFSVR model's relative error has more points falling within the low error interval and its prediction error is smaller, demonstrating a better prediction effect.

Furthermore, when comparing the evaluation metrics on sunny and cloudy days, it is discovered that practically all of the models predict more accurately on sunny days than on cloudy ones. This is because cloudy days have a lot of output power fluctuation, which makes it harder for the models to predict. Nonetheless, the MOFSVR models' MAE, MAPE, and RMSE values are minimized regardless of the weather, showing that the error is minimized; also, the R^2 value is greater than 0.99, indicating a high degree of goodness of fit. In conclusion, the suggested MOFSVR model outperforms the other seven comparison models in terms of prediction accuracy and may be used to forecast PV power in a range of situations[23][102].

Example 2 uses three standard models and five hybrid models to predict PV power during cloudy conditions. Analysis reveals that the MOFSVR model has the best prediction accuracy out of the seven comparison models; its predicted power curve is closer to the true value, its relative error is smaller, and its number of sample points within the low relative error range is significantly higher than that of the other hybrid and traditional models. Four evaluation indices were computed using each model's true and predicted values in order to more objectively assess the prediction effect of each model, and the calculation results are shown in Table 4.13.

表 4.13 阴天时模型预测结果的评价指标值

Table 4.13 Evaluation index value of model prediction results on cloudy days

Climatic	model	*MAE*（kW）	*MAPE*	*RMSE*（kW）	R^2
Cloudy	MOFSVR	**0.12565**	**6.05%**	**0.15920**	**0.9921**
	JSSVR	0.15868	11.60%	0.17998	0.9899
	WOASVR	0.20546	12.10%	0.26876	0.9773
	GASVR	0.26567	24.08%	0.31265	0.9693
	PSOSVR	0.15673	11.25%	0.17692	0.9902
	SVR	0.27267	27.79%	0.32748	0.9663
	ELM	0.38611	36.86%	0.46795	0.9311
	BPNN	0.33048	38.15%	0.41740	0.9455

The MOFSVR model has the smallest result for MAE in cloudy conditions in Table 4.13, at 0.12563 kW, followed by the PSOSVR model at 0.15672 kW. Only the MOFSVR model, with the biggest value for the ELM model at 36.87%, has a value of less than 10% for MAPE, at 6.03%, which is 5.56% less than that of the JSSVR model. The MOFSVR model has the smallest RMSE value, at 0.15919 kW, which is 0.30877 kW less than the greatest value, which belongs to the ELM model. Only the MOFSVR and PSOSVR models, with respective values of 0.992 and 0.9901, had values of R^2 of 0.99 or higher than the other six models, with the ELM model having the lowest value of 0.931. The suggested MOFSVR model continues to have the best prediction effect out of all the models in cloudy weather, according to a thorough evaluation of the prediction effects of all the prediction models in cloudy weather[100][101].

4.5 Summary

This chapter looks at the MOFSVR model's predictions for wind and PV power. It also uses seven comparison prediction models with four assessment indices to confirm the predicted power of the suggested MOFSVR model. The results are outlined below:

(1) This chapter does PV power prediction under two weather conditions: sunny and cloudy, and wind power prediction under two seasons: spring and winter. It also provides a detailed description of the sources of data utilized in the study and the preprocessing techniques[30][101].

(2) According to the prediction results of PV power prediction examples 1 and 2, the proposed MOFSVR model has an average absolute error (MAE) of 0.05434 kW in sunny weather, an average absolute percentage error (MAPE) of 1.45%, which is 1.76% lower than that of the ELM model with the maximum value, and a root-mean-square error (RMSE) of 0.07003 kW in cloudy weather; in cloudy weather, the proposed MAE, MAPE, and RMSE of the MOFSVR model are 0.12563 kW, 6.03%, and 0.15919 kW, respectively, where the MAPE value of the MOFSVR model is 5.56% lower than that of the JSSVR model; The MOFSVR model's three error evaluation indices mentioned above are lower than those of the other seven models under comparison. Furthermore, the MOFSVR model fits the data better than the seven comparison models, with an R^2 value of 0.9975 for sunny days and 0.9920 for overcast days for the decidability coefficient. It demonstrates that the MOFSVR model is more suited for predicting PV power on bright and overcast days due to its higher forecast accuracy and fitting degree[93].

(3) Based on the wind power prediction results for Example 1 and Example 2, it can be observed that during the spring, the MOFSVR model's evaluation index values for MAE, MAPE, and RMSE are 32.4371 kW, 10.17%, and 42.9526 kW, respectively. The MOFSVR model's MAPE value is 2.25% lower than the JSSVR model's; the evaluation index R^2 value is 0.9828, making it the only prediction model with a value greater than 0.98. It has been demonstrated that the suggested MOFSVR prediction model is more appropriate for wind power prediction in the spring since it has a smaller prediction error and a greater goodness of fit than the other seven models. The suggested MOFSVR model's wintertime MAE, MAPE, and RMSE are 41.5001 kW, 5.59%, and 50.1780 kW, respectively; its R^2 value is 0.9905; compared to the seven models that were examined, the MOFSVR model has a smaller prediction error and a greater degree of fit. It demonstrates that wind power forecast in the spring and winter can be done using the suggested MOFSVR model.

(4) With a broader range of applications, the suggested MOFSVR prediction model can be used to estimate wind power in various scenarios. When it comes to forecasting PV power under sunny and cloudy conditions, as well as wind power in the spring and winter, the proposed MOFSVR model outperforms the four hybrid models and the three traditional models in terms of prediction performance. This can effectively increase the accuracy of wind power prediction[94].

Chapter 5 Optimal Analysis of Reactive Power Compensation with distributed generations

The large-scale grid connection of distributed generation represented by wind power and photovoltaics has changed the original operation mode and system structure of distribution networks, posing challenges to the stability and economy of distribution network operation. Therefore, research on optimization of distribution network operation with distributed generation is particularly important. The optimization methods for distribution network operation include static restructuring and reactive power compensation. Among them, static restructuring, at a fixed time section, adjusts the network topology by changing the switching status to reduce power losses, balance loads, and improve power quality in the distribution network. However, static restructuring only improves the operation of the distribution network by optimizing the network topology without providing on-site compensation for reactive power in the system. Reactive power compensation is an optimization method in reactive power optimization of distribution networks, which compensates the reactive power of the distribution network by controlling reactive power compensation devices, reducing the reactive power flowing in the distribution network, thereby improving power quality, increasing energy efficiency, and reducing active power losses[103]. However, distribution network reactive power compensation does not change the system topology and cannot effectively handle power loss problems caused by line overloads. In conclusion, both static restructuring and reactive power compensation can improve the operation of distribution networks with some limitations. Therefore, this chapter combines static restructuring and reactive power compensation, taking into account the grid connection of distributed generation, to conduct comprehensive static optimization research on distribution networks with distributed generation[85][86].

Static comprehensive optimization of distribution networks with distributed generation based on static restructuring and reactive power compensation is an important optimization approach. It combines static restructuring and reactive power compensation to optimize the network topology and reactive power output of compensation devices at a fixed time section, aiming to obtain the optimal network topology and the optimal compensation scheme for reactive power devices in the distribution network[1][4][5]. This optimization approach aims to improve the power quality, economic efficiency, and energy efficiency of distribution networks.

In the context of promoting the grid connection of renewable energy generation, exploring static comprehensive optimization of distribution networks with distributed generation is of significant practical importance.

This chapter aims to improve the economic efficiency, energy efficiency, and power quality of distribution networks with distributed generation. It combines the Firefly Optimization Algorithm (FA) proposed in Chapter 3 to develop and solve a static comprehensive optimization model for distribution networks with distributed generation. The objective is to achieve safe, economical, and stable operation of distribution networks with distributed generation.

5.1 Integrated Static Optimization Model for power distribution network

This chapter combines reactive power compensation and static restructuring as optimization methods to construct a static comprehensive optimization model for distribution networks with distributed generation. It comprehensively considers the economic cost, power losses, and voltage fluctuation of the distribution network, aiming to explore the static comprehensive optimization solution that maximizes the overall benefits of the distribution network.

5.1.1 Objective Function and Constraints for Static Optimization Model

(1) Construction of the optimization variables for the static optimization model

The optimization variables for the static comprehensive optimization model include the switching status of the distribution network with distributed generation, the reactive power output of the static VAR compensator, and the number of parallel-connected capacitor banks. These variables are used to obtain the optimal network topology and the best reactive power compensation scheme for the distribution network with distributed generation, aiming to maximize its overall benefits[36],[106],[108]–[110]. The expression for the optimization variables in the static comprehensive optimization model is as follows:

$$Z = [Z_1^S, \dots, Z_a^S, Z_1^{SVC}, \dots, Z_b^{SVC}, Z_1^{SC}, \dots, Z_c^{SC}] \tag{5.1}$$

The fundamental role played by the components in Z.

(a) Switches(S), responsible for open/close circuits within the distribution network. They are used for reconfiguring the network topology, isolating faults, and managing load distribution.

(b) Static VAR compensators (SVC): they are used for fast-acting reactive power compensation. They can dynamically adjust the reactive power flow, thereby controlling and stabilizing voltage levels within the network.

(c) Parallel connected capacitor banks (SC): These are used to inject reactive power into the system while improving the power factor and thus reducing reactive power losses. They are favorable for steady state reactive power compensation compared to dynamically compensation provided by SVCs.

In the equation (5.1), Z represents the set of optimization variables; S, SVC, and SC represent the switches, static VAR compensators, and parallel-connected capacitor banks in the distribution network respectively; Z_1^S and Z_a^S represent the first and ath switches to be either opened or closed. The state of these switches affects how power is distributed and how the network is configured; Z_1^{SVC} and Z_b^{SVC} represent the reactive power output of the first and bth static VAR compensators. By adjusting these outputs permits for control over the voltage and reactive power levels within the network; Z_1^{SC} and Z_c^{SC} represent the number of groups for the first and cth parallel-connected capacitor banks. Due to these SCs, the reactive power compensation provided by each capacitor bank is determined.

(2) Construction of the objective function for the static optimization model.

To enhance the economic efficiency, energy efficiency, and power quality of distribution networks with distributed generation, the objective function of the static comprehensive optimization model aims to minimize the economic costs, active power losses, and node voltage deviations of distribution networks with distributed generation.

（a）Objective function for economic cost.

The economic cost of distribution networks with distributed generation includes energy loss cost, switch operation cost, and operation cost of the distribution network[70], [110]-[114]. Its expression is:

$$f_{cost} = c_a \sum_{k=1}^{n_b} p_{loss}^k + c_b n_S + c_r \tag{5.2}$$

Where f_{cost} represents the objective function for economic cost; c_a , n_b and p_{loss}^k represent the energy loss coefficient, the number of branches, and the active power loss on the kth branch respectively; n_S and c_b represent the number of switch operations and the cost per operation; c_r represents the operation cost of the distribution network with distributed generation, including the cost of purchasing electricity and the investment cost of reactive power compensation equipment. Its expression is:

$$c_r = c_e(p_{load} - p_{DG}) + c_s \times \sum_{j=1}^{ns} n_j + p \times \sum_{j=1}^{nc} q_j \times c_j \tag{5.3}$$

Where p_{DG} and p_{load} represent the active power output of the distributed power source and the total load of the distribution network; q_j represents the reactive power output of the j-th reactive power compensation device; c_e, c_s, and c_j represent the electricity price, the cost of a single group of parallel-connected capacitor banks, and the unit capacity investment cost of the static VAR compensator; n_c and n_S represent the number of groups of parallel-connected capacitor banks and the number of static

VAR compensators; p is the investment cost recovery factor, expressed as:

$$p = \frac{(1+a)^y \times a}{(1+a)^y - 1} \tag{5.4}$$

Where y and a represent the equipment's service life and interest rate, typically with $a = 0.06$.

（b） Objective function for active power loss

Active power loss quantifies the energy efficiency of distribution networks with distributed generation, and its expression is:

$$f_{loss} = \sum_{k=1}^{n_b} r_k \frac{p_k^2 + q_k^2}{u_k^2} \tag{5.5}$$

Where f_{loss} represents the objective function for active power loss; k, r_k and n_b represent the branch number, impedance of the kth branch, and the total number of system branches; p_k and q_k represent the active power and reactive power flowing into the first node of the kth branch; u_k represents the node voltage at the first node of the kth branch.

（c） Objective function for node voltage deviation

Node voltage deviation can measure the level of power quality in distribution networks with distributed generation. A larger value indicates lower power quality in the system. The mathematical expression is:

$$f_{dev} = \frac{1}{n_n} \sum_{i=1}^{n_n} \left| u_i^2 - u_r^2 \right| \tag{5.6}$$

Where f_{dev} represents the objective function for node voltage deviation; n_n, u_r, and u_i represent the total number of system nodes, reference voltage, and voltage magnitude at the i-th node respectively.

(a) Construction of constraints for the static optimization model

(1) Power balance constraint

The sum of the output powers of various distributed energy sources in the distribution network and the system injection power should be equal to the sum of the load demand and the system power loss. The mathematical expression is:

$$\begin{cases} p_Z + p_{DG} = p_{load} + p_{loss} \\ q_Z + q_{DG} = q_{load} + q_{loss} \end{cases} \tag{5.7}$$

Where p_Z and q_Z represent the active power and reactive power flowing into the distribution network from the balancing node; p_{DG} and q_{DG} represent the active output power and reactive output power of the distributed energy sources; p_{load} and q_{load} represent the active power demand and reactive power demand of the load; p_{loss} and q_{loss} represent the active power loss in the distribution network and the reactive power absorbed by the line impedance.

（2）Inequality constraints

The inequality constraints of the static comprehensive optimization model include constraints on the reactive power output of static VAR compensators, node voltage constraints, and constraints on the number of groups of parallel-connected capacitor banks[107]. It can be formulated as follows:

$$\begin{cases} u_{i,min} \le u_i \le u_{i,max} \\ q_{SVC,min} \le q_{SVC} \le q_{SVC,max} \\ n_{SC,min} \le n_{SC} \le n_{SC,max} \end{cases} \tag{5.8}$$

Where u_i, $u_{i,max}$, and $u_{i,min}$ represent the node voltage, upper limit, and lower limit of the node voltage at the ith node respectively; $q_{SVC,min}$, q_{SVC} , and $q_{SVC,max}$ represent the lower limit, actual value, and upper limit of the reactive power output of the static VAR compensator; n_{SC} , $n_{SC,min}$, and $n_{SC,max}$ represent the number of groups of parallel-connected capacitor banks, lower limit, and upper limit of the number of groups of parallel-connected capacitor banks.

（3）Topological structure constraints

$$h \in H \tag{5.9}$$

Where h and H represent the reconstructed distribution network's topological structure and the set of topological structures that satisfy the radial network configuration of the distribution network.

5.1.2 Construction of the static optimization model

$$\begin{cases} \min \begin{cases} f_{cost}=c_a \sum_{k=1}^{n_b} p_{loss}^{k} + c_b n_S + c_e (p_{load} - p_{DG}) + c_s \sum_{j=1}^{n_S} n_j + p \sum_{j=1}^{n_C} q_j c_j \\ f_{loss}=\sum_{k=1}^{n_b} r_k \frac{p_k^2+q_k^2}{u_k^2} \\ f_{dev}=\frac{1}{n_n} \sum_{i=1}^{n_n} \left| u_i^2 - u_r^2 \right| \end{cases} \\ \text{s.t.} \begin{cases} p_Z + p_{DG} = p_{load} + p_{loss} \\ q_Z + q_{DG} = q_{load} + q_{loss} \\ h \in H \\ u_{i,min} \le u_i \le u_{i,max} \\ q_{SVC,min} \le q_{SVC} \le q_{SVC,max} \\ n_{SC,min} \le n_{SC} \le n_{SC,max} \end{cases} \end{cases} \tag{5.10}$$

The mathematical model of the static comprehensive optimization model for distribution networks with distributed energy sources can be obtained by combining the objective function and constraints[89][95][98][99][100].

The parameters for the economic cost objective function f_{cost}, active power loss objective function f_{loss}, and node voltage deviation objective function f_{dev} are given in equations (5.2) to (5.6). The specific parameters for the constraints are given in equations (5.7), (5.8), and (5.9).

5.2 Objective Function and Constraints Formulation for Static Optimization model

5.2.1 Process design for solving the model based on Firefly algorithm

The static comprehensive optimization model takes into account the economic benefits, energy benefits and power quality of the distribution network at the same time, and takes minimizing the economic cost, voltage deviation and power loss of the distribution network as the objective function, so it needs to be solved through a multi-objective optimization algorithm.

5.3 Analyzing Solution to Static Optimization in Distribution network

5.3.1 Designing Static Optimization Systems with Wind and Solar power

In this section, a static comprehensive optimization test system is established based on the IEEE 33-bus system. The system includes photovoltaic (PV) units, wind turbines (WT), static var compensators (SVC), and shunt capacitor banks (SC). The total load of the system is 3715+j2350 kVA, with a base capacity of 10 MVA and a base voltage of 12.66 kV. The system has 32 feeder branches and 5 tie branches. As the distribution network operates in an open-loop state, the system forms a radial distribution network consisting of 32 branches under normal operation. The topology structure of the static comprehensive optimization test system is shown in Figure 5.1.

The load flow calculation precision is set to 10^{-6}. The system's base voltage is 12.66 kV, and it demands the strictest standards for power quality. The upper and lower voltage limits for system nodes are set at 1.05 p.u and 0.95 p.u, respectively[2][10][14]–[19][122].

The installation locations, power factors, control methods, and installed capacities of different types of distributed energy resources in the system are shown in Table 5.1.

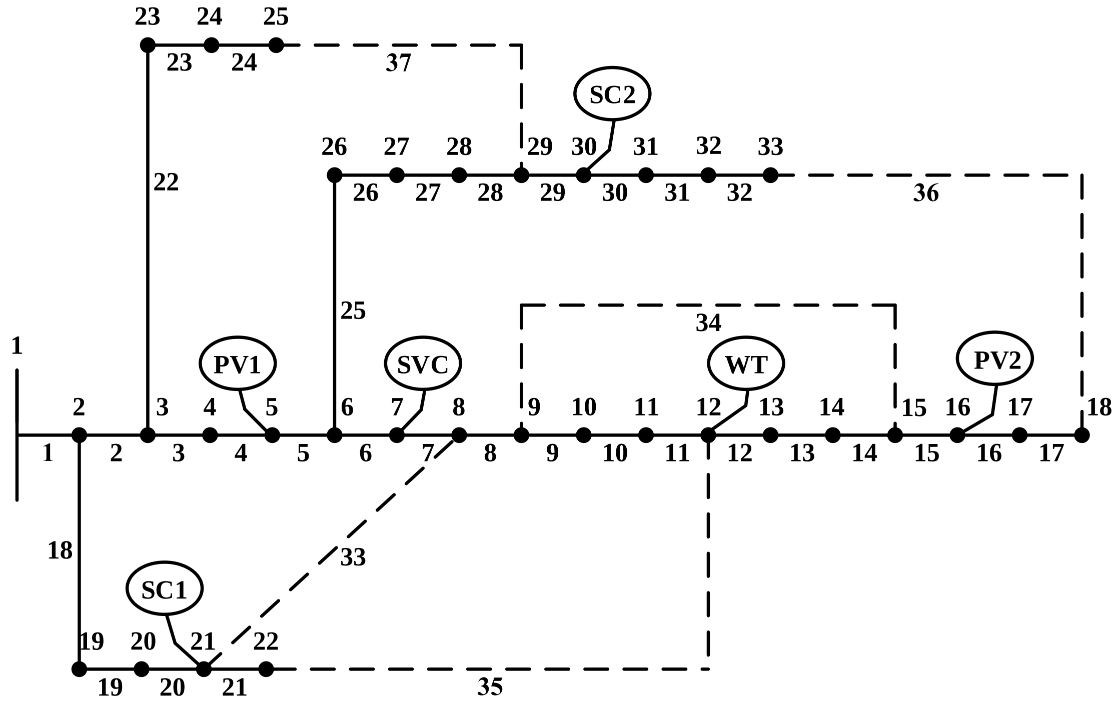

图 5.1 静态综合优化测试系统拓扑图

Figure 5.1 Topology diagram of static integrated optimization test system

From Figure 5.1, it can be seen that the first node of the test system is the balanced node. The fifth node has a photovoltaic power station (PV1) connected, the sixteenth node has another photovoltaic power station (PV2) connected, and the twelfth node has a wind turbine (WT) connected. Additionally, a static var compensator (SVC) is installed at the seventh node with an upper limit of 0.5 MVAr for reactive power output and a regulation accuracy of 0.01 MVar. A shunt capacitor bank (SC1) is installed at the twenty-first node, and another shunt capacitor bank (SC2) is installed at the thirtieth node. Each group of shunt capacitors has a rated capacity of 0.02 MVAr, with a maximum number of 50 groups that can be activated.

表 5.1 IEEE 33 节点系统中各分布式发电的安装位置和容量

Table 5.1 Installation location and capacity of each distributed generation in IEEE 33 node system

Type	Location	Capacity (MW)	Power Factor	Control Method
WT	Node 12	0.5	0.9（Lagging）	Constant Power Factor Control
PV1	Node 5	0.5	0.85（Lagging）	Constant Power Factor Control
PV2	Node 16	0.5	0.85（Lagging）	Constant Power Factor Control

5.3.2 Analyzing Static Optimization Model Impact

To verify the effectiveness of the static comprehensive optimization model for distribution networks with distributed generation, this section designs five comparative scenarios with specific settings as follows:

Scenario 1:

Without considering the integration of distributed generation and without optimization, the distribution network operates normally.

Scenario 2:

Based on Scenario 1, distributed generation is integrated, but without optimization, and the distribution network operates normally.

Scenario 3:

On the basis of Scenario 2, only static reconfiguration is used for optimization.

Scenario 4:

Based on Scenario 2, only reactive power compensation is employed for optimization.

Scenario 5:

Building upon Scenario 2, a combination of static reconfiguration and reactive power compensation is applied to perform comprehensive optimization using the static comprehensive optimization model established in this chapter.

As mentioned earlier, the FA algorithm has been verified to be effective in solving the static comprehensive optimization model for distribution networks with distributed generation. Therefore, this section adopts the FA algorithm for solving in each scenario. The economic cost (f_{cost}), active power loss (f_{loss}), and node voltage deviation (f_{dev}) of the distribution networks with distributed generation in each scenario are presented in Table 5.2.

表 5.2 在各种情况下采用分布式发电的配电网的经济成本、有功功率损耗和节点电压偏差

Table 5.2 Economic cost, active power loss and node voltage deviation of the distribution network with distributed generation in each scenario

Scenario	Objective Function		
	f_{cost} (\$)	f_{loss} (kW)	f_{dev} (p.u.)
Scenario1	2451.87	202.67	9.953×10^{-2}
Scenario2	1317.84	83.19	4.977×10^{-2}
Scenario3	**1078.74**	55.29	2.983×10^{-2}
Scenario4	1196.24	51.75	3.182×10^{-2}
Scenario5	1167.68	**32.71**	$\mathbf{1.877\times10^{-2}}$

Table 5.2 demonstrates that Scenario 1 represents an unoptimized distribution network, where the economic cost, voltage deviation, and power loss are all at their highest values, specifically 2451.87$, 9.953×10^{-2} p.u., & 202.67kW. This indicates

significant room for improvement in terms of system economic, efficiency, energy efficiency, and power quality.

Scenario2 incorporates distributed generation based on Scenario1, resulting in a reduction of 1134.03$ in economic cost, 119.48 kW in active power loss, and 4.976×10^{-2} p.u. in node voltage deviation compared to Scenario 1. This demonstrates that the integration of distributed generation can reduce system economic costs, minimize energy losses, and enhance power quality.

Compared to Scenario 2, Scenario 3 achieves a 18.14% reduction in economic cost, a 33.54% decrease in active power loss, and a 40.06% improvement in node voltage deviation. This indicates that both objectives have been improved. Similarly, Scenario 4, when compared to Scenario 2, demonstrates a 9.23% reduction in economic cost, a 37.79% decrease in active power loss, and a 36.07% improvement in node voltage deviation. This suggests that both static reconfiguration and reactive power compensation alone can enhance the system's economic efficiency, energy efficiency, and power quality, although there is still room for further improvement.

When comparing Scenario 3 to Scenario 4, the system economic cost and node voltage deviation in Scenario 3 are reduced by 9.82% and 6.25%, respectively, while the active power loss increases by 6.84%. This indicates that static reconfiguration is more effective in reducing economic costs and improving power quality compared to reactive power compensation.

Scenario 5, which incorporates the static comprehensive optimization model developed in this chapter based on Scenario 2, achieves a 11.39% reduction in economic cost, a 60.68% decrease in active power loss, and a 62.29% improvement in node voltage deviation compared to Scenario 2. Among all scenarios, Scenario 5 has the lowest active power loss and node voltage deviation. While Scenario 3 has the lowest economic cost of 1078.74$, Scenario5 with economic cost of 1167.68$ is only slightly higher. However, Scenario 5 achieves a 40.84% reduction in active power loss and a 37.08% improvement in node voltage deviation compared to Scenario 3. This demonstrates that, compared to static reconfiguration or reactive power compensation alone, the static comprehensive optimization model developed in this chapter can maximize system energy efficiency and improve power quality while maintaining system economics.

5.3.3 Performance analysis based on Firefly Algorithm for static problem

To demonstrate the effectiveness of the FA algorithm, the MOMVO, FOA, GWO, and FA algorithms were all employed to solve the constructed static comprehensive optimization model. The Pareto-fronts and the optimal compromise solutions selected through the ideal solution of similarity ranking technique are presented in Figure 5.2

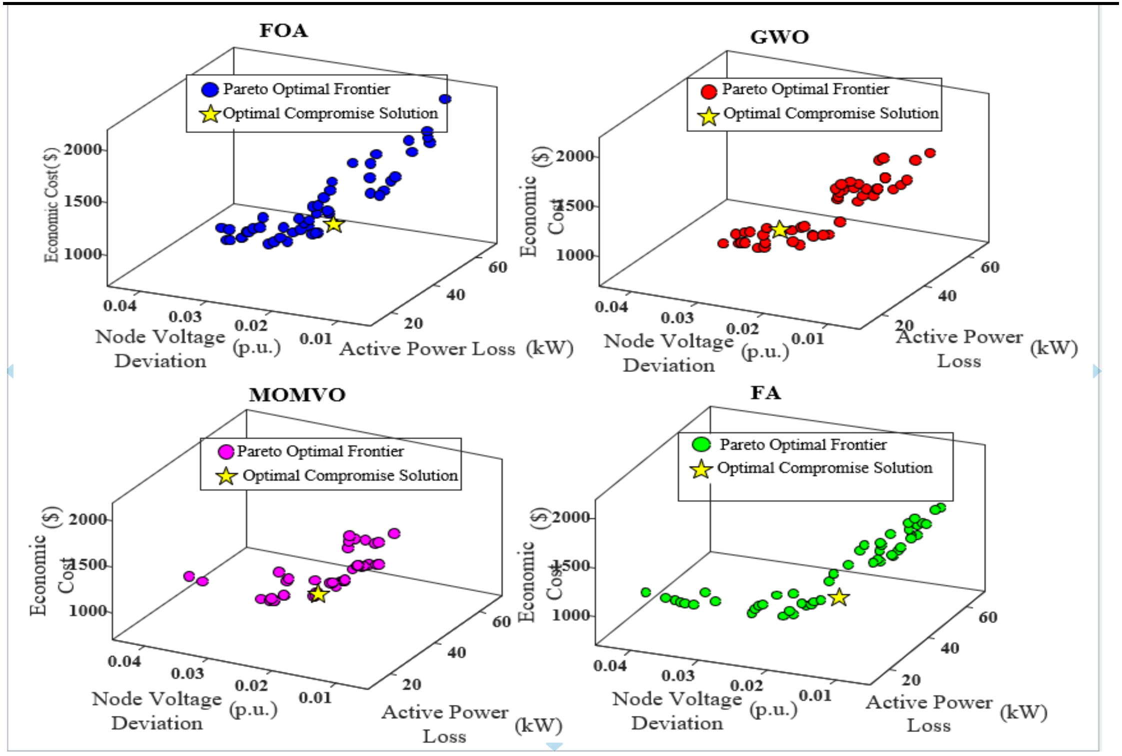

图 5.2 各算法得到的静态综合优化模型的帕累托前沿

Figure 5.2 Pareto front of the static integrated optimization model obtained by each algorithm

As shown in Figure 5.2, compared to the FOA, GWO, and MOMVO algorithms, the FA algorithm exhibits a more extensive distribution range and a more uniform distribution of the Pareto frontier in the solution space. The MOMVO algorithm produces a relatively small number of solutions in its Pareto frontier, indicating its poorer performance in solving the static comprehensive optimization model. In contrast to other multi-objective optimization algorithms, the FA algorithm is more suitable for handling the complexity of the static comprehensive optimization model, with a wider, more uniform, and more complete coverage of the Pareto frontier. This suggests a higher likelihood of obtaining solutions that maximize the overall system benefits.

To provide a more intuitive comparison of the optimal compromise solutions obtained by each algorithm, Table 5.3 presents the economic cost (f_{cost}), active power loss (f_{loss}), and node voltage deviation (f_{dev}) for the distribution networks with distributed generation corresponding to the optimal compromise solutions found by each algorithm. The optimal values for each objective function are boldfaced for emphasis.

Table 5.3 shows the high performance of the multi-objective optimization algorithms based on firefly search algorithm. FOA algorithm achieves the lowest active power loss among all the algorithms considered. Although the active power loss obtained by the FA algorithm is slightly higher than that of the FOA, its economic cost and node voltage deviation are significantly lower.

表 5.3 各算法获得的最优折中方案对应的经济成本、有功功率损耗和节点电压偏差

Table 5.3 The economic cost, active power loss and node voltage deviation corresponding to the optimal compromise solution obtained by each algorithm

Objective Function	Multi-objective Optimization Algorithm			
	MOMVO	FOA	GWO	FA
f_{cost} (\$)	1185.11	1210.73	1212.06	**1167.68**
f_{loss} (kW)	31.40	**29.07**	29.29	32.71
f_{dev} (p.u.)	2.018×10^{-2}	2.427×10^{-2}	2.346×10^{-2}	$\mathbf{1.877\times10^{-2}}$

In terms of economic cost, the FA algorithm outperforms the others, achieving a cost reduction of 17.43, 43.05, and 44.38 $ compared to the MOMVO, FOA, and GWO algorithms, respectively. For the node voltage deviation objective, the FA algorithm also performs best, achieving a deviation that is 1.41×10^{-3} p.u., 5.5×10^{-3} p.u., and 4.69×10^{-3} p.u. lower than those obtained by the MOMVO, FOA, and GWO algorithms, respectively.

Compared to the other algorithms, the FA algorithm achieves a maximum reduction of 3.6% in active power loss and 22.7% in node voltage deviation. These results demonstrate that, compared to other multi-objective optimization algorithms, the optimization scheme obtained by the FA algorithm can maximize system economic efficiency and power quality while ensuring energy benefits in distribution networks with distributed generation.

To further analyze the impact of the optimization solutions obtained by each algorithm on system voltage stability, Figure 5.3 presents the distribution of system node voltages obtained by each algorithm.

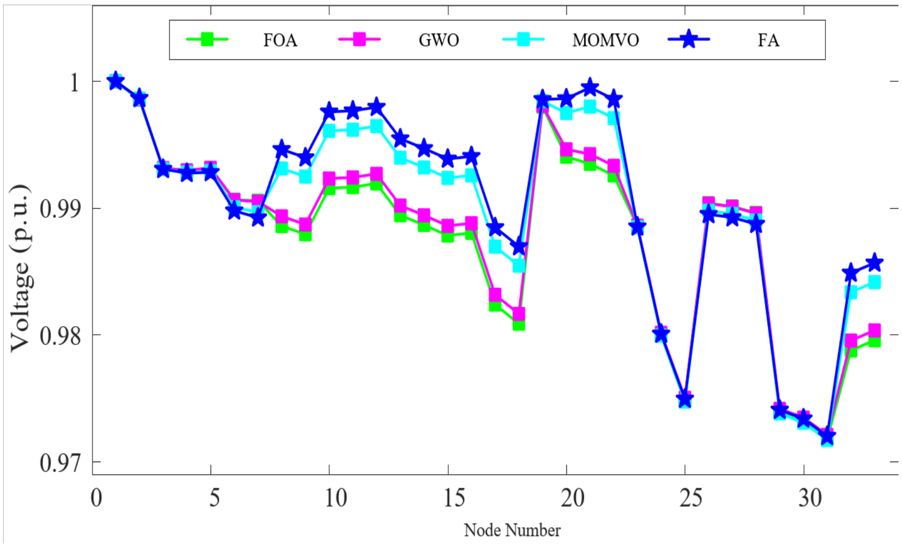

图 5.3 各算法得出的系统节点电压分布图

Figure 5.3 Node voltage distribution of system obtained by each algorithm

As shown in Figure 5.3, the system node voltages obtained by all algorithms are greater than 0.95 p.u., satisfying the node voltage constraints. Compared to the GWO algorithm, the FA algorithm results in node voltages that are further away from the reference value at nodes 6,7,26,27 and 28, resulting in slightly larger voltage fluctuations than GWO. However, these fluctuations are still better than those obtained by the FOA and MOMVO algorithms. Additionally, at other nodes, the voltages obtained by the FA algorithm are closer to the reference value, with the smallest voltage fluctuations and the best voltage stability. This demonstrates that the optimization scheme obtained by the FA algorithm can effectively suppress node voltage fluctuations and improve the power quality of the system to the greatest extent[106].

5.4 Summary

To improve the economic efficiency, energy benefits, and power quality of distribution networks with distributed generation, this chapter combines static reconfiguration and reactive power compensation to establish a static comprehensive optimization model for distribution networks with distributed generation. The model is then solved using the FA algorithm proposed in Chapter 3, and the effectiveness of both the model and the proposed solution method is validated. The specific conclusions are summarized as follows:

(1) By minimizing the economic cost, node voltage deviation, and active power loss of the distribution network as objective functions, a static comprehensive optimization model for distribution networks with distributed generation is established, combining both static reconfiguration and reactive power compensation. The model is solved using the proposed FA algorithm to obtain a Pareto set of optimal solutions. Finally, a compromise solution is selected from the Pareto set using the ideal solution similarity ranking technique.

(2) The effectiveness and advancement of the proposed FA algorithm in solving the static comprehensive optimization model are verified in a test system. The results show that compared to the FOA, GWO, and MOMVO algorithms, the FA algorithm achieves a wider, more uniform, and more complete coverage of the Pareto front. The optimal compromise solution obtained by the FA algorithm is the most competitive, with power losses and node voltage deviations reduced by up to 3.6% and 22.7%, respectively, compared to other algorithms.

(3) Five comparison scenarios are designed to verify the effectiveness of the static comprehensive optimization model. The results demonstrate that optimizing using the static comprehensive optimization model proposed in this chapter can maximize system energy benefits and improve power quality while ensuring system economy.

Specifically, the economic cost, active power loss, and node voltage deviation of the system are reduced by 11.39%, 60.68%, and 62.29%, respectively, compared to the original system. Additionally, the static comprehensive optimization model established in this chapter serves as the foundation for the dynamic comprehensive optimization model developed in Chapter 6.

Chapter 6 Dynamic Optimization of Power distributions network

6.1 Dynamic Optimization Model for distributed energy resources and reactive power compensation

This chapter relies on the previously developed static comprehensive optimization model, combining two optimization methods: dynamic reconfiguration and reactive power compensation. It considers the economic benefits, energy efficiency, and power quality of the distribution network that uses dispersed energy resources. In addition, it takes into account the coupling between different time sections as well as the limits on the number of switch operations in the distribution network to provide a dynamic complete optimization model for the distribution network with distributed energy resources.

6.1.1 Objective Function Construction for Dynamic Optimization

The original static comprehensive optimization model was created to improve the system's structure and regulate the reactive power output from compensation devices within a specific time frame. However, this approach fails to account for the dynamic and complicated nature of real-world engineering projects. In practice, the starting condition of the distribution network for the following timeframe is influenced by the preceding period's optimization results, demonstrating the interdependence of multiple time segments. Furthermore, it is necessary to include concerns such as time-of-use power, variability pricing in outputs from distributed energy resources, constraints on the frequency of switching operations within the network, and changes in load needs[50][72][123]. This highlights the necessity for research into dynamic comprehensive optimization of distribution networks that include distributed energy resources.

Dynamic reconfiguration, which involves adjusting the network's topology across consecutive time periods to enhance operational efficiency, does not significantly affect the reactive power flow within the network[124][125].While reactive power compensation can alleviate some issues by balancing the system's reactive power needs[105], it is insufficient for addressing problems like line overloads comprehensively. The limitations of both dynamic reconfiguration and reactive power compensation underline the need for their integration in achieving a holistic optimization solution[105]. Additionally, frequent switching operations can cause premature equipment wear and potentially impact system stability[126]. By incorporating time-segmentation into the dynamic comprehensive optimization process, it's possible to substantially improve the effectiveness of dynamic reconfiguration and reduce the frequency of switch operations[87].Dynamic comprehensive optimization of the distribution network, which encompasses dynamic reconfiguration and reactive power compensation, aims to achieve the optimal system topology and the most effective reactive power compensation scheme for reactive power compensation devices over a future period, under various constraints[127]. This optimization approach accounts for the interplay between different time sections, fluctuations in distributed energy resource outputs, time-of-use electricity prices, constraints on switch operations, and changes in load demand[10][11]. Its primary objective is to maximize power quality, economic benefits, and energy efficiency within the distribution network integrating distributed energy resources. Time-segment division plays a crucial role by breaking down the optimization period into multiple sections, allowing for more efficient optimization of the distribution network under each segment. This strategy effectively reduces the optimization cycle and the number of switch operations[130]. In the context of large-scale grid integration of distributed energy resources like photovoltaics and wind power, research on dynamic comprehensive optimization of distribution networks with distributed energy resources considering time-segment division holds significant importance[131]. This chapter investigates on the economic benefits, energy efficiency, and power quality of distribution networks using distributed energy resources. It combines dynamic reconfiguration and reactive power compensation optimization methods, bringing together the solution algorithm described in Chapter 3 and the static comprehensive optimization model built in Chapter 4. Additionally, it investigates the effect of time-segment division on dynamic comprehensive optimization in distribution networks with scattered energy supplies[132].

(1) Economic Cost Objective Function

The economic cost of a distribution network with distributed energy resources includes the energy loss cost, investment cost of static var compensators, switching operation cost, shunt capacitor switching cost, and operational cost of the distribution network over an optimization period. The mathematical expression for the economic cost of the distribution network with distributed energy resources is as follows:

$$\begin{cases} F_{cost} = \sum_{t=1}^{T} E_{cost}^{t} \\ E_{cost}^{t} = C_a \sum_{k=1}^{N_b} P_{t,loss}^{k} + C_b N_S^t + C_r^t \end{cases} \tag{6.1}$$

Where， F_{cost} represents the economic cost objective function， T denotes the optimization period， E_{cost}^{t} represent the system’s economist cost in period t.C_a is the energy loss cost coefficient， C_b represent the cost of a single switch operation，

N_b represents the number of branches， P_{loss}^{k} represents the active power loss on the kth branch， N_S^t represents the number of switch operations in period,t. C_r^t represents the total operating cost of the distribution network with distributed generation in period t, including the cost of purchasing electricity, the operation cost of parallel capacitor banks, and any other relevant costs.

And the investment cost of static var compensators,with its specific expression as follows:

$$C_r^t = C_e^t(P_{load}^t - P_{DG}^t) + C_s N_S^t + P \times \sum_{j=1}^{N_C} Q_j^t \times C_j \tag{6.2}$$

Including (6.2) into (6.1), result in extended function of the economic cost objective function,

$$\begin{cases} F_{cost} = \sum_{t=1}^{T}\left(C_a \sum_{k=1}^{N_b} P_{t,loss}^{k} + C_b N_S^t + C_r^t\right) \\ C_r^t = C_e^t(P_{load}^t - P_{DG}^t) + C_s N_S^t + P \times \sum_{j=1}^{N_C} Q_j^t \times C_j \end{cases} \tag{6.3}$$

Where $\mathrm{C_a}$, $\mathrm{C_b}$, $\mathrm{N_b}$, $\mathrm{P_{loss}^{k}}$, N_S^t are defined as above, P_{load}^t represents the load power demand in period t. P_{DG}^t represent the distributed generation power in period t. C_e^t is the cost coefficient for energy consumption. C_r^t represents the total operating cost of the distribution network with distributed generation in period t .C_s represent the cost associated with other system operations.N_c is the number of additional cost factor,Q_j^t represents the quantity of the jth additional cost factor in period t. C_j represents the cost per unit of the jth addidtional cost factor.

The equation 6.3 now captures the total operating cost of the distribution network considering energy consumption, switch operations, and other additional cost factors.

In the intricate realm of electricity distribution networks, the balance between demand and supply is paramount, not only for ensuring reliability and stability but also for optimizing economic efficiency. As the energy sector evolves, integrating distributed generation and enhancing load management have become critical challenges that require innovative solutions. Among these, the strategic deployment of Static Var Compensators (SVCs) and capacitor banks plays a pivotal role in managing reactive power, a key factor in maintaining voltage stability and reducing transmission losses.

However, the financial implications of such technological interventions cannot be overlooked. The active power output of distributed generation (P_{DG}), the active power load demand of the distribution network (P_D), and the reactive power output of SVCs ($Q_{SVC,j}$) Represents the operational backbone of these systems. Concurrently, the economic landscape is defined by the electricity price (P_t), the investment in equipment like SVCs (C_j), and the overarching need for an efficient investment recovery strategy.

$$C_r^t = C_e^t(P_{load}^t - P_{DG}^t) + C_s N_S^t + P \times \sum_{j=1}^{N_C} Q_j^t \times C_j + N_{cap}^t C_s + C_s \tag{6.4}$$

Where other parameters have explained as above, N_{cap}^t represent the number of capacitor bank groups switched on during period t.N_C represent the number of SVCs involved in reactive power compensation.

This is where the concept of the equipment investment recovery factor (P) becomes indispensable. The equipment investment recovery factor (P) is a nuanced formula that encapsulates the essence of financial planning in the electricity distribution sector. It provides a method to calculate the annual payments needed to recover the investment in infrastructure over a specified period, taking into account the interest rate (a) and the duration (y) of the investment. This formula not only underscores the financial viability of deploying advanced technologies in the distribution network but also offers a blueprint for sustainable economic management in the face of growing energy demands and the imperative for grid modernization. The following discussion delves into the intricacies of energy balance, exploring how the calculated approach to investment recovery can illuminate pathways to a more resilient and economically viable electricity distribution network.

$$P = \frac{(1+a)^y \times a}{(1+a)^y - 1} \tag{6.5}$$

In this context, y and a respectively represent the equipment's service life and the interest rate.

(2) Active Power Loss Objective Function

The dynamic integrated optimization model uses the sum of active power losses in the distribution network with distributed generation over an optimization period as the objective function. The active power loss is used to measure the energy efficiency of the distribution network; the higher its value, the lower the energy efficiency of the distribution network[133]. Its expression is as follows:

$$\begin{cases} F_{loss} = \sum_{t=1}^{T} P_{loss}^t \\ P_{loss}^t = \sum_{k=1}^{N_b} R_k \frac{P_{k,t}^2 + Q_{k,t}^2}{U_{k,t}^2} \end{cases} \tag{6.6}$$

In this context, F_{loss} and represent the active power loss objective function and P_{loss}^t is the system's active power loss in period t, respectively; T, k, R_k, and $N_b$respectively denote the optimization period, branch identifier, impedance of the k^th^ branch, and the number of branches in the distribution network; $P_{k,t}$ and $Q_{k,t}$ respectively represent the active power and reactive power injected at the head node of the k^{th} branch in period (t); $U_{k,t}$ represents the voltage at the head node of the k^th^ branch in period (t).

(3) Node Voltage Deviation Objective Function

The Node Voltage Deviation Objective Function is a critical concept in the study and management of power system distribution. It plays a significant role in ensuring the quality and reliability of the electrical power supply. This objective function is used to minimize the deviation of node voltages from their nominal or desired values, which is essential for the stable and efficient operation of the power system. By focusing on minimizing these deviations, power system operators can reduce the risk of voltage collapse, improve the overall system stability, and enhance the power quality delivered to the end-users[65][133]. Greater node voltage deviation indicates larger voltage fluctuations at various nodes in the distribution network, implying lower electric energy quality. Conversely, a smaller value indicates higher electric energy quality. Its mathematical expression is as follows:

$$\begin{cases} F_{dev} = \sum_{t=1}^{T} V_{dev}^{t} \\ V_{dev}^{t} = \left(\frac{1}{N_n} \sum_{i=1}^{N_n} \left| U_{i,t}^{2} - U_{r}^{2} \right| \right) \end{cases} \tag{6.7}$$

In this context, $\mathrm{F}_{dev}(t)$ represent the node voltage deviation objective function, (t) and (T) respectively denote the operation period and optimization period.$\mathrm{U}_{\mathrm{i,t}}$ represent the voltage magnitude at node (i) in period(t).N_n represent the total number of nodes,U_r is the reference voltage.

6.1.2 Constraint Construction for Dynamic Optimization

The dynamic integrated optimization model considers power balance constraints, node voltage constraints, reactive power output constraints of static var compensators, switching group number constraints of parallel capacitor banks, distribution network topology constraints, and switch operation number constraints within an optimization period for the distribution network.

(1) Power Balance Constraint

Within the optimization period, the sum of distributed generation output and system injected power at each node for each time period should equal the sum of the load demand and line power losses at each node for each time period. The expression is as follows:

$$\begin{cases} P_{i}^{t} + P_{wt,i}^{t} + P_{pv,i}^{t} = P_{load,i}^{t} + U_{i}^{t} \sum_{j=1}^{n} U_{j}^{t} (G_{ij} \cos\theta_{ij} + B_{ij} \sin\theta_{ij}) \quad i = 1,2，\ldots, N_n \\ Q_{i}^{t} + Q_{wt,i}^{t} + Q_{pv,i}^{t} = Q_{load,i}^{t} + U_{i}^{t} \sum_{j=1}^{n} U_{j}^{t} (G_{ij} \sin\theta_{ij} - B_{ij} \cos\theta_{ij}) \quad i = 1,2，\ldots, N_n \end{cases} \tag{6.8}$$

In this context, (*i*) and (*j*) respectively represent the starting node number and the ending node number of branch (*ij*); N_n, (n), (wt), (pv), and (load) respectively denote the total number of nodes in the distribution network, the total number of branches, wind turbine generators, photovoltaic power stations, and loads;(P_i^t),($P_{wt,i}^t$),($P_{pv,i}^t$), and ($P_{load,i}^t$)respectively represent the injected active power at node (i) in period (t), the active power output of wind turbine generators, the active power output of photovoltaic power stations, and the active power demand of system load in period (t); (Q_i^t), ($Q_{wt,i}^t$), ($Q_{pv,i}^t$), and ($Q_{load,i}^t$) respectively represent the injected reactive power at node (i) in period (t), the reactive power output of wind turbine generators, the reactive power output of photovoltaic power stations, and the reactive power demand of system load in period (t); (U_i^t) and (U_j^t) respectively represent the node voltage at node (i) and node (j) in period (t); (G_{ij}), (θ_{ij}), and (B_{ij}) respectively represent the real part of the admittance, the impedance angle, and the imaginary part between node (i) and node (j).

(2) Node Voltage Constraint

$$U_{i,min}^t \leq U_i^t \leq U_{i,max}^t \tag{6.9}$$

In this context, $U_{i,max}^t$, U_i^t, and $U_{i,min}^t$ respectively represent the upper limit of the node voltage, the value of the node voltage, and the lower limit of the node voltage at node (i) in period (t).

(3) Reactive Power Output Constraint of Static Var Compensator (SVC)

$$Q_{svc,min}^t \leq Q_{svc}^t \leq Q_{svc,max}^t \tag{6.10}$$

In this context, SVC represents Static Var Compensator; $Q_{svc,min}^t$, Q_{svc}^t, and $Q_{svc,max}^t$ respectively denote the lower limit, output, and upper limit of reactive power output of the Static Var Compensator in period (t).

(4) Number of Switching Actions Constraint for Parallel Capacitor Units

$$N_{SC,min}^t \leq N_{SC}^t \leq N_{SC,max}^t \tag{6.11}$$

In this context, SC represents the parallel capacitor unit group; (N_{SC}^trepresents the number of parallel capacitor units switched on in period (t); ($N_{SC,min}^t$) and ($N_{SC,max}^t$) respectively represent the lower and upper limits of the number of parallel capacitor units switched on in period (t).

(5) Topological Structure Constraint of Distribution Network with Distributed Energy Resources

$$h_t \in H_t \tag{6.12}$$

In this context, (h_t) and (H_t) respectively represent the topological structure of the distribution network after network reconfiguration in period (t) and the set of topological structures of the distribution network that satisfy radial operation.

(6) Switching Operation Count Constraint

$$\sum_{t=1}^{T} N_S^t \leq N_{S,max} \tag{6.13}$$

In this context, (T) is an optimization period; (N_S^t) represents the number of switching actions in period (t); ($N_{S,max}$) represents the upper limit of the number of switching actions within one optimization period.

By integrating the objective function and constraints of the dynamic comprehensive optimization model of distribution networks with distributed energy resources established in this chapter, the specific mathematical model is obtained as follows:

$$\begin{cases} min \begin{cases} F_{cost} = \sum_{t=1}^{T} E_{cost}^t \\ F_{loss} = \sum_{t=1}^{T} P_{loss}^t \\ F_{dev} = \sum_{t=1}^{T} V_{dev}^t \\ E_{cost}^t = C_a \sum_{k=1}^{N_b} P_{t,loss}^k + C_b N_S^t + C_e^t (P_{load}^t - P_{DG}^t) + C_s N_S^t + P \times \sum_{j=1}^{N_C} Q_j^t C_j \\ P_{loss}^t = \sum_{k=1}^{N_b} R_k \frac{P_{k,t}^2 + Q_{k,t}^2}{U_{k,t}^2} \\ V_{dev}^t = \left(\frac{1}{N_n} \sum_{i=1}^{N_n} \left| U_{i,t}^2 - U_r^2 \right| \right) \end{cases} \\ s.t. \begin{cases} P_i^t + P_{wt,i}^t + P_{pv,i}^t = P_{load,i}^t + U_i^t \sum_{j=1}^{n} U_j^t (G_{ij} \cos\theta_{ij} + B_{ij} \sin\theta_{ij}) \\ Q_i^t + Q_{wt,i}^t + Q_{pv,i}^t = Q_{load,i}^t + U_i^t \sum_{j=1}^{n} U_j^t (G_{ij} \sin\theta_{ij} - B_{ij} \cos\theta_{ij}) \\ h_t \in H_t \\ U_{i,min}^t \leq U_i^t \leq U_{i,max}^t \\ Q_{svc,min}^t \leq Q_{svc}^t \leq Q_{svc,max}^t \\ N_{SC,min}^t \leq N_{SC}^t \leq N_{SC,max}^t \\ \sum_{t=1}^{T} N_S^t \leq N_{S,max} \end{cases} \end{cases} \tag{6.14}$$

In this context, the specific parameters for the economic cost objective function (F_{cost}), active power loss objective function (F_{loss}), and node voltage deviation objective function (F_{dev}) can be found in equations (6.1) to (6.7), and the specific parameters for the constraints can be found in equations (6.8) to (6.13) and thus resulting in the overall minimization problem of (6.14).

6.2 Design of Dynamic Optimization Model Solution by using Time-Segment Division method

Dynamic comprehensive optimization of distribution networks with distributed energy resources must consider constraints on the number of switching actions to maintain system stability and prolong the lifespan of switchgear[131][125].

6.2.1 Time-Segment Method Based on Euclidean Distance

Frequent switching actions in distribution networks can accelerate switchgear aging and jeopardize system stability [120].Segmenting time periods offers a solution by reducing the number of optimizations through period merging, thereby decreasing the frequency of switching actions in the distribution network and improving operational stability and economic efficiency[134].This chapter proposes a novel time period segmentation method based on Euclidean distance for dynamic segmentation of optimization periods. The objective here is to effectively manage switching actions while optimizing operational performance and economic benefits[135][136].

(1) Fundamental Concept of Euclidean Distance

Euclidean distance, also known as Euclidean metric, is a commonly used distance definition that refers to the actual distance between two points in Euclidean space. In three-dimensional space, the Euclidean distance between two points is the straight-line distance between them. The formula for calculating the Euclidean distance between two points in three-dimensional space is:

$$D_{A,B} = \sqrt{(a_1 - b_1)^2 + (a_2 - b_2)^2 + (a_3 - b_3)^2} \tag{6.15}$$

In this context, $D_{A,B}$ is the Euclidean distance between point A and point B; the spatial coordinates of point A are $(a_1,\ a_2,\ a_3)$; and the spatial coordinates of point B are $(b_1,\ b_2,\ b_3)$.

Generalizing to n-dimensional space, the formula for calculating the Euclidean distance between two points has been given by:

$$D_{C,D} = \sqrt{\sum_{i=1}^{n}(c_i - d_i)^2} \tag{6.16}$$

In this context, $D_{C,D}$ is the Euclidean distance between point C and point D; the spatial coordinates of point C are $(c_1,\ c_2, ...,\ c_n)$; and the spatial coordinates of point D are $(d_1,\ d_2, ..., d_n)$.

(2) Procedure of Time Period Segmentation Method Based on Euclidean Distance

In dynamic comprehensive optimization, the initial state of the system in the next time period is the optimization result of the previous time period, indicating coupling between different time sections. Without time period segmentation, conducting comprehensive optimization in each time period would require continuous switching actions, which can accelerate equipment aging. Therefore, this chapter proposes a time period segmentation method based on Euclidean distance to dynamically segment optimization periods and reduce the number of switching actions. The time period segmentation method based on Euclidean distance merges two adjacent time periods with target function deviations within a certain range, effectively reducing the number of switching actions and improving optimization efficiency.

The specific steps of the time period segmentation method based on Euclidean distance proposed in this chapter are as follows:

Step 1: Normalize the objective function values obtained from the given model. Since the dynamic comprehensive optimization model includes three objective functions: economic cost, voltage deviation, and power loss, and the values of each objective function are not on the same scale, in order to eliminate the influence of different scales, normalize the values of each objective function. The expression for normalizing each objective function is defined as:

$$\begin{cases} Z_{cost}^{t} = \frac{F_{cost}^{t}}{f_{cost,o}^{t}} \\ Z_{loss}^{t} = \frac{F_{loss}^{t}}{f_{loss,o}^{t}} \\ Z_{dev}^{t} = \frac{F_{dev}^{t}}{f_{dev,o}^{t}} \end{cases} \tag{6.17}$$

In this context, (Z_{cost}^{t}), (Z_{loss}^{t}), and (Z_{dev}^{t}) respectively represent the normalized economic cost, active power loss, and node voltage deviation of the distribution network in time period t;$\widehat{C_t}$,$\widehat{P_t}$, and $\widehat{V_t}$ respectively represent the economic cost, active power loss, and node voltage deviation of the distribution network after dynamic comprehensive optimization with distributed generation in time period t; C_t,P_t, and V_t respectively represent the economic cost, active power loss, and node voltage deviation of the distribution network in time period t without optimization.

These equations serve to normalize the values of economic cost, active power loss, and node voltage deviation by dividing the observed values by a function of these values with respect to some optimization objective at a given time. This normalization allows for a standardized comparison over time or between different scenarios, such as before and after the application of dynamic comprehensive optimization with distributed generation.

Step 2: Calculate the Euclidean distance ($D_{t,t-1}$) between the normalized objective functions of time period t and time period t-1, with the following mathematical expression:

$$D_{t,t-1} = \sqrt{(Z_{cost}^{t} - Z_{cost}^{t-1})^2 + (Z_{loss}^{t} - Z_{loss}^{t-1})^2 + (Z_{dev}^{t} - Z_{dev}^{t-1})^2} \tag{6.18}$$

In this context, $D_{t,t-1}$ represents the Euclidean distance between the normalized objective functions of time periods t and t-1; ($\bar{C}_{t-1}$ and $\bar{C}_t$) denote the normalized economic costs for time periods t-1 and t, respectively; ($\bar{P}_{t-1}$ and $\bar{P}_t$) represent the normalized active power loss of the distribution network in time period t-1 and time period t, respectively; ($\bar{V}_{t-1}$ and $\bar{V}_t$) represent the normalized node voltage deviations of the distribution network in time period t-1 and time period t, respectively.

Step 3: Set a threshold value D_{max} for the Euclidean distance of the objective functions and segment the time periods based on the comparison between $D_{t,t-1}$ and

D_{max}. The specific segmentation method is as follows:

1) When ($D_{t,t-1} < D_{max}$), it indicates that the variation between the objective function values of time period t and time period t-1 is within the specified range. In this case, merge time period t with time period t-1, and optimization result for the merged period is based on the more recent period (t).

2) When ($D_{t,t-1} \geq D_{max}$), it indicates that the variation between the objective function values of time period t and time period t-1 exceeds the specified range. In this case, we do not merge time period t with time period t-1, and keep the optimization results of time period t and time period t-1 separately.

Step 4: Check if the total number of switching actions in the distribution network satisfies the constraints. If the constraints are not satisfied, dynamically adjust the threshold value (D_{max}) by setting ($D_{max} = D_{max} + 0.1$), and then re-optimize the system. If the constraints are satisfied, output the optimized solutions for each time period after segmentation, including the set of switches to be turned off in each time period and the reactive power compensation scheme for each time period.

6.2 Dynamic Optimization via Time-Segment Division

This chapter builds a dynamic comprehensive optimization test system based on the IEEE 69-node system, and conducts comprehensive optimization for the next day with a time interval of 1 hour.

6.2.1 Dynamic Optimization Test System Design with Wind and Solar

The system has included the Static Var Compensator (SVC), Shunt Capacitor (SC) banks, Photovoltaic (PV) stations, and Wind Turbine (WT) generator units. The total load, base capacity, and base voltage of the test system are 3802.2+j2694.6 kVA, 10 MVA, and 12.66 kV, respectively. The initial system has 73 branches, including 5 tie-switch branches and 68 breaker branches, with a total of 69 nodes numbered from 1 to 69. The distribution network operates in an open-loop state and functions as a radial distribution network during normal operation. The installation locations and capacities of various distributed energy resources are shown in Table 6.1.

表 6.1 各分布式发电的安装地点和容量

Table 6.1 Installation location and capacity of each distributed generation

Type	Installation location	Installed capacity (MW)	Power factor	Control method
WT	Node 64	0.5	0.9（lag）	Constant PF control
PV1	Node 38	0.5	0.85（lag）	Constant PF control
PV2	Node 53	0.5	0.85（lag）	Constant PF control

The topological structure of the dynamic comprehensive optimization test system is shown in Figure 6.1, including the connection of distributed energy sources and reactive power compensation devices.

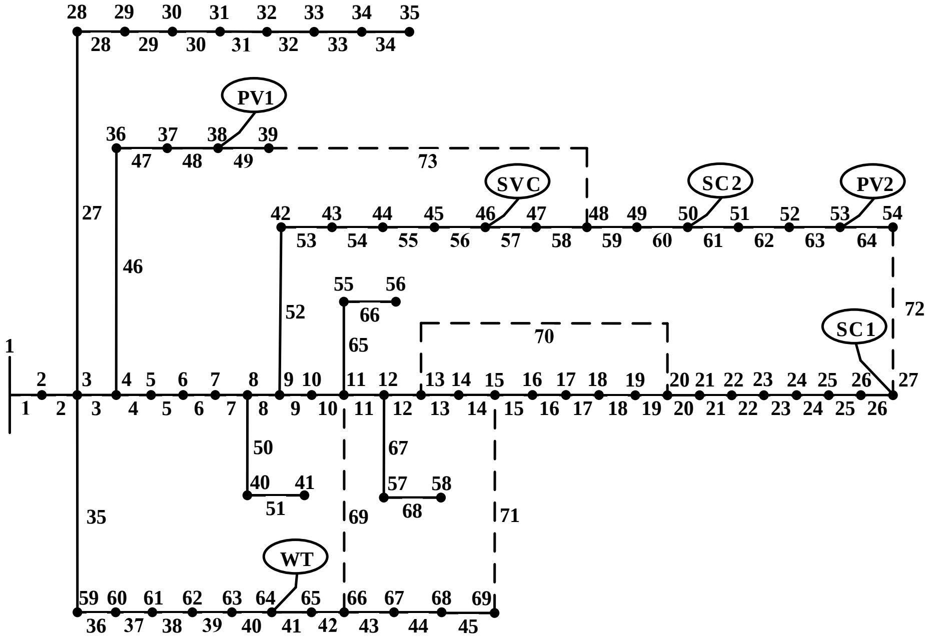

图 6.1 动态综合优化测试系统拓扑图

Figure 6.1 Topology diagram of dynamic integrated optimization test system

From Figure 6.1, it can be seen that the system has a total of 73 branches. The dashed lines in the figure represent tie-switch branches, with a total of 5 tie-switch branches.

During normal operation, the tie-switch branches are in the open state to ensure the radial operation of the distribution network. Node 1 is the balance node, nodes 38 and 53 have Photovoltaic (PV) connections, and node 64 has a Wind Turbine (WT) generator unit connection. Node 46 is equipped with a Static Var Compensator (SVC) with a reactive power output limit of 0.5 MVAr and a regulation accuracy of 0.01 MVar. Nodes 27 and 50 are installed with Shunt Capacitor banks (SC1 and SC2), each with a rated capacity of 0.02 MVar and a maximum number of units that can be switched on is 50.

Additionally, following the reference[138], the system parameters include energy loss cost coefficient Ca = \$10/kW, Static Var Compensator unit investment cost Cd = \$12.5/kVar, breaker operation cost Cb = \$5/time, and Shunt Capacitor bank unit switching cost CS = \$3/unit. The service life of the SVC is set to 15 years, the investment recovery rate is 0.06, and the maximum number of breaker operations for the dynamic comprehensive optimization test system is set at 30 times. The base voltage of the system is 12.66 kV, aiming for high-quality power supply. The upper voltage limit at each node during different time periods is set to 1.05p.u., while the lower voltage limit is set to 0.95p.u. The initial value of the objective function Euclidean distance threshold D_{max} in the time period division is set to 0.1, and the convergence precision of the power flow calculation is set to 10^{-6}. The active load of the system in different time periods is illustrated in Figure 6.2.

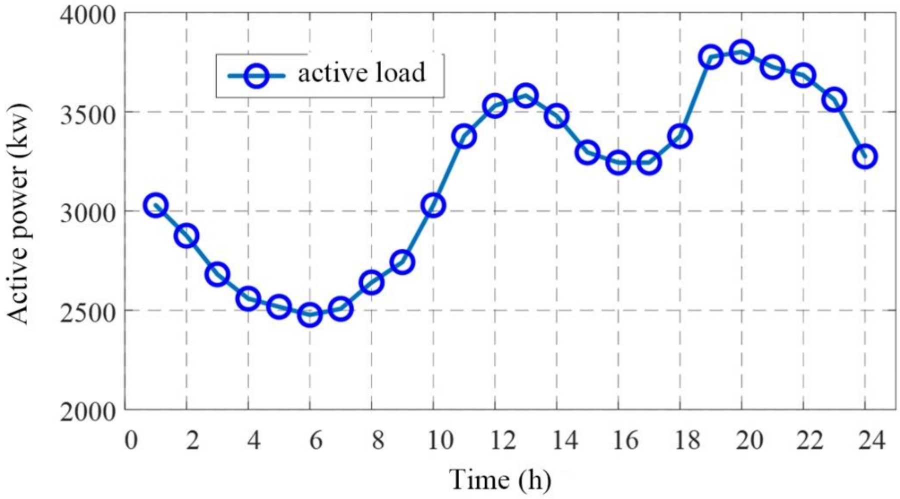

图 6.2 各时段系统的有功负载

Figure 6.2 Active load of the system for each time period

The output power of the wind turbine is derived from the power prediction of wind power generation. Meteorological indicators such as wind speed and wind direction are set as input variables for the prediction model, while the output variable is set as the output power of wind power generation. After normalizing all research data and training all prediction models using wind power generation training data, the models are tested using test data. Following the testing, the power prediction values outputs by all prediction models are recorded, and an output power prediction curve is plotted. The relative error between the calculated prediction values and the actual values is computed, and a curve of the relative errors is plotted.

The wind power generation power prediction during winter is shown in Figure 6.3 In winter, five hybrid prediction models (MOFSVR, JSSVR, WOASVR, GASVR, and PSOSVR) are used for wind power generation output power prediction. The figure shows the true values of the output power as well as the predicted values obtained from the models.

From Figure 6.3, it can be observed that none of the five hybrid models completely fit the true values in the interval of 0:00-4:00. However, it can still be seen that the deviation of the prediction curves for the MOFSVR and JSSVR models is smaller. In the interval of 4:00-12:00, the prediction curves of the MOFSVR and JSSVR models are closer to the true values at the peak. In the interval of 12:00-16:00, the GASVR and PSOSVR models exhibit larger deviations at some sample points. From the local magnification in the interval of 20:00-24:00, it can be observed that the MOFSVR model fits better with the true value curve, while the PSOSVR model deviates further from the true values.

Combining the above figure 6.3, it is not apparent to distinguish the differences in prediction performance among the models. Therefore, further verification using relative errors is necessary.

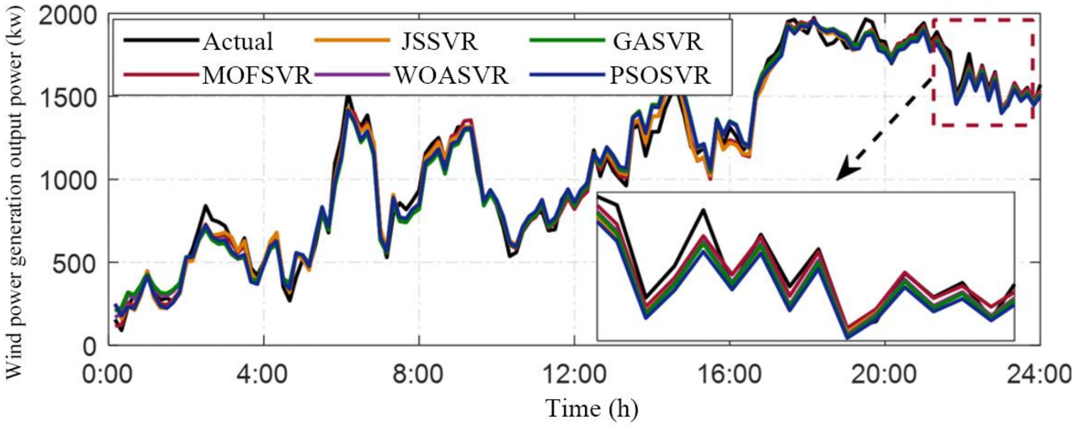

图 6.3 混合预测模型在冬季的预测结果

Figure 6.3 Prediction results of hybrid prediction models in winter

In figure 6.3, whether in spring or winter, compared to the 7 contrast models, the error between the predicted values and the true values of the proposed MOFSVR model is the smallest, demonstrating optimal predictive performance and good prediction accuracy. This proves that the proposed MOFSVR model is more suitable for wind power generation power prediction in different scenarios.

6.2.2 Performance Analysis of Multi-Objective Optimization Algorithm

The system economic cost (F_{cost}), active power loss (F_{loss}), and node voltage deviation (F_{dev}) obtained by each algorithm for solving the dynamic integrated optimization model are shown in Table 6.2, with the optimal values for each indicator highlighted in bold font.

表 6.2 各算法对动态综合优化模型的求解结果

Table 6.2 The solution results of the dynamic integrated optimization model obtained by each algorithm

Objective function	Multi-objective optimization algorithm			
	MOMVO	NSMFO	NSGA-II	MOFSA
F_{cost} ($)	2.1129×10^4	2.1659×10^4	2.0328×10^4	**2.0326×10^4**
F_{loss} (kW)	6.8523×10^2	6.2154×10^2	6.4257×10^2	**6.0597×10^2**
F_{dev} (p.u.)	**0.2467**	0.2612	0.2567	0.2697

As can be seen from Table 6.2 compared to other algorithms, the MOFSA algorithm achieves the lowest economic cost and active power loss, which are $20,326 and 605.97 kW respectively. This represents a reduction of up to 6.15% and 11.6% compared to the highest figures among other algorithms. In terms of power quality, the MOMVO algorithm results in the lowest node voltage deviation, at 0.2467 p.u. The node voltage deviation obtained by the MOFSA algorithm is 0.2697 p.u., slightly higher than that of the MOMVO algorithm, with an increase of 0.023 p.u. However, the economic cost and active power loss solved by the MOFSA algorithm are significantly lower than those of the MOMVO algorithm, reduced by $803 and 79.26 kW respectively. This indicates that the optimization scheme obtained by the MOFSA algorithm can maximize system energy efficiency and economic benefits while ensuring the quality of electric power. The power losses of the system at different times obtained by the different algorithms are shown in Figure 6.4.

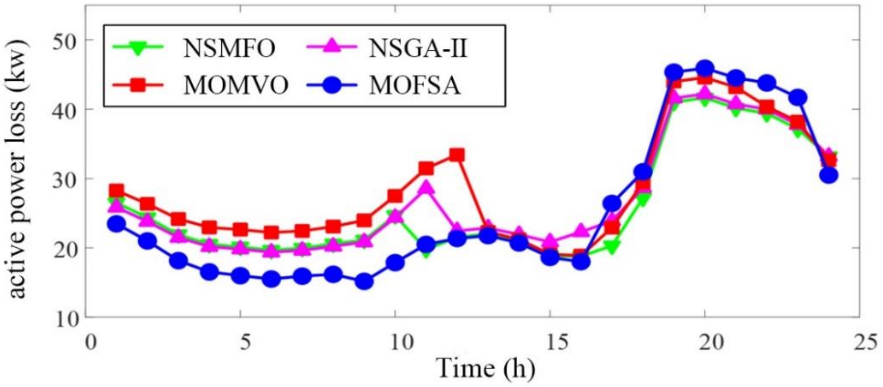

图 6.4 不同算法得出的各时段系统功率损耗

Figure 6.4 System power loss for each time period obtained by different algorithms

As can be seen from Figure 6.4, between 1 AM and 10 AM, the active power loss of the system obtained by the MOFSA algorithm is significantly lower than that of other algorithms, with the maximum difference reaching 9.62 kW. From 11 AM to 4 PM, the difference in active power loss between the MOFSA algorithm and other algorithms is smaller, but it remains the lowest. During other periods, the active power loss obtained by the MOFSA algorithm is slightly higher than that of other algorithms, but the difference is small. Furthermore, throughout the entire optimization period, compared to other algorithms, the total active power loss of the system obtained by the MOFSA algorithm is the lowest, indicating that the optimization scheme obtained by the MOFSA is the most competitive in improving the energy efficiency of the system.

6.2.3 Analysis of Dynamic Optimization Model with Time-Segment Division

This section has constructed the four scenarios to compare and verify the effectiveness of the proposed dynamic comprehensive optimization model. The specific settings for each scenario have been defined as follows:

Scenario 1: The system has stayed in its initial state, not optimized, including the normal operation of the distributed power supply in distribution network.

Scenario 2: Involved the dynamic restructuring and time period division of the distributed power supply distribution network.

Scenario 3: Involved both the reactive power compensation and time period division of the distributed power supply in distribution network;

Scenario 4: Combined the dynamic restructuring and reactive power compensation, using the dynamic comprehensive optimization model proposed in this chapter for optimization and time period division. Based on the previous validation of the effectiveness and advancement of the MOFSA algorithm in solving the dynamic comprehensive optimization model, this section has used the MOFSA algorithm to solve for each scenario. The 24-hour active power loss F_{loss}, node voltage deviation F_{dev} and economic cost F_{cost} for each scenario were shown in Table 6.3

表 6.3 各方案的 24 小时功率损耗、电压偏差和经济成本

Table 6.3 The 24-hour power loss, voltage deviation and economic cost of each scenario

Scenario	F_{loss}(kW)	F_{dev}(p.u.)	F_{cost}($)
Scenario 1	3.1372×10^3	0.9668	3.9423×10^4
Scenario 2	8.2774×10^2	0.4444	$\mathbf{1.6458\times10^4}$
Scenario 3	2.0701×10^3	0.5398	3.2595×10^4
Scenario 4	$\mathbf{6.0597\times10^2}$	**0.2697**	2.0326×10^4

From Table 6.3, it is apparent that the data which has been bolded represents the optimal values of various objective functions. Compared to Scenario 1, where no optimization was performed, in Scenario 2, which only involved dynamic restructuring, the power loss, voltage deviation, and economic cost were reduced by 73.62%, 54.03%, and 58.25%, respectively. Scenario 2 has the lowest economic cost indicator among all scenarios, indicating that solely performing dynamic restructuring, without considering the investment cost of reactive power compensation devices, can significantly reduce economic costs, though there is still considerable room for improvement in active power loss and node voltage deviation. Compared to Scenario 1, Scenario 3, which only involved reactive power compensation, saw reductions in active power loss, node voltage deviation, and economic cost by 34.01%, 44.17%, and 17.32%, respectively.

The objective function of Scenario 3 did not achieve the optimal value in any scenario, indicating that solely performing reactive power compensation can still enhance the system's economic benefits, energy efficiency, and power quality. Compared to Scenario 1, Scenario 4 combines dynamic restructuring with reactive power compensation for dynamic comprehensive optimization, reducing active power loss, node voltage deviation, and economic cost by 80.68%, 72.10%, and 48.44%, respectively. Among all scenarios, Scenario 4 has the lowest active power loss and node voltage deviation, at 6.0597×10^2 kW and 0.2697 p.u. respectively. The economic cost of Scenario 4, at 2.0326×10^4 \$, is only higher than that of Scenario 2 and shows a reduction of 26.79% and 39.31% in active power loss and node voltage deviation, respectively, compared to Scenario 2. Compared to only performing dynamic restructuring in Scenario 2 and only reactive power compensation in Scenario 3, combining both strategies in Scenario 4 for dynamic comprehensive optimization results in the highest reductions in economic cost, node voltage deviation, and power loss by 37.64%, 50.04%, and 70.73%, respectively. This demonstrates that adopting a dynamic comprehensive optimization model for optimization can significantly improve the system's energy efficiency and power quality while ensuring economic benefits, thereby verifying the effectiveness of the proposed model.

6.2.4 Analysis of Time-Segment Division Method Using Euclidean Distance

To verify the effectiveness of the proposed time-segmentation method based on Euclidean distance, this section sets up two models for comparative analysis:

Model A: A dynamic integrated optimization model for distributed generation power distribution networks without time segmentation.

Model B: A dynamic integrated optimization model for distributed generation power distribution networks with time segmentation using the proposed method based on Euclidean distance.

The dynamic integrated optimization without time segmentation refers to optimizing each time period of the power distribution network without considering the constraints on the number of switch operations, and solving for the optimization scheme of each time period in the power distribution network through the MOFSA algorithm. Using this as a baseline, the extent of improvement in the number of switch operations, power loss, node voltage deviation, and economic cost by employing the time segmentation method in the power distribution network is analyzed comparatively. Moreover, given the previous verification of the MOFSA algorithm's effectiveness and advancement in solving the dynamic integrated optimization model for distributed generation power distribution networks, the MOFSA algorithm is used to solve both comparative analysis models A and B.

To compare the improvement levels of the optimization solutions obtained from the two models in terms of economic benefits, energy efficiency, power quality, and reduction in the number of switch operations, Table 6.4 displays the economic cost

F_{cost}, active power loss F_{loss}, node voltage deviation F_{dev}, and the number of switch operations N_S for each model solution, with the optimal values of each indicator being highlighted in bold.

表 6.4 各模型的求解结果

Table 6.4 Each model solving results

Objective Function	Optimization	
	Model A	Model B
N_S (times)	94	**20**
F_{cost}(\$)	2.2031×10^4	$\mathbf{2.0326\times10^4}$
F_{loss} (kW)	6.3624×10^2	$\mathbf{6.0597\times10^2}$
F_{dev} (p.u.)	$\mathbf{2.5186\times10^{-1}}$	2.6972×10^{-1}

As shown in Table 6.4, compared to Model A, Model B has the lowest number of switch operations, economic cost, and active power loss, with reductions of 78.72%, 7.74%, and 4.76% respectively. The node voltage deviation obtained by Model B is increased by 1.786×10^{-2} p.u. compared to Model A. However, although the node voltage deviation of Model B has increased by 7.09% compared to Model A, all other indicators are significantly better than those of Model A. Specifically, the number of switch operations obtained by Model B is only 20 times, which is 74 times less than that of Model A, with a reduction rate of 78.72%. This indicates that the time division method based on Euclidean distance can effectively reduce the number of system switch operations while ensuring the system's economic cost, energy efficiency, and power quality, thus verifying the effectiveness of the proposed time period division method.

6.3 Summary

This chapter builds upon the static comprehensive optimization model, taking into account factors such as the coupling between different time sections and the number of switch operations, and combines dynamic restructuring and reactive power compensation as optimization approaches. It establishes a dynamic comprehensive optimization model for distributed generation in distribution networks and solves it using the Hybrid search strategy-based firefly Algorithm (MOFSA) proposed in Chapter 3. Additionally, to address the issue of frequent switching operations in the distribution network, a time-period segmentation method based on Euclidean distance is proposed to dynamically adjust the system optimization periods, thereby reducing the number of switch operations. The effectiveness of the proposed time-period segmentation method, the established dynamic comprehensive optimization model, and the proposed solution algorithm are verified through a test system, with the following specific summaries:

(1) Based on the static comprehensive optimization model, considering the coupling between different time sections and constraints on the number of switch operations, with the goal of minimizing the economic cost of the distribution network, node voltage deviation, and power loss, and combining dynamic restructuring and reactive power compensation as optimization methods, a dynamic comprehensive optimization model for a distribution network with distributed generation is established. The model is solved using the MOFSA algorithm proposed in Chapter 3. Results show that compared to the NSGA-II, MOMVO, and NSMFO algorithms, the MOFSA algorithm achieves the most competitive optimization scheme, reducing the system's economic cost and active power loss by up to 6.15% and 11.6% respectively, proving the effectiveness and advancement of the MOFSA algorithm in solving dynamic comprehensive optimization models.

(2) Four comparative scenarios were designed, and the effectiveness of the established model was verified in a test system. Results indicate that compared to other scenarios, the dynamic comprehensive optimization model that combines dynamic restructuring and reactive power compensation achieves the lowest node voltage deviation and active power loss, at 0.2697 p.u. and 6.0597×10^2 kW respectively. Moreover, compared to just dynamic restructuring or reactive power compensation alone, the combined dynamic comprehensive optimization model reduces active power loss, node voltage deviation, and economic cost by up to 70.73%, 50.04% and 37.64% respectively. This demonstrates that optimizing with the model established in this chapter can significantly improve system energy efficiency and power quality while ensuring economic benefits, verifying the effectiveness of the established model.

(3) A time-period segmentation method based on Euclidean distance is proposed, which dynamically segments optimization periods under the constraint of the number of switch operations. Test results show that compared to not segmenting time periods, optimizing with the proposed time-period segmentation method achieves the lowest number of switch operations, economic cost, and active power loss, reducing them by 78.72%, 7.74%, and 4.76% respectively. Specifically, the number of switch operations in the distribution network is reduced from 94 to 20, a reduction of 74 operations, representing a decrease of 78.72%, proving the effectiveness of the proposed time-period segmentation method.

Chapter 7 Conclusions, innovations and outlook

7.1 Conclusion

This thesis was focused on the integration challenges of distributed power sources within the power grid, with the aim of enhancing power quality, economic efficiency, and energy efficiency. The combined optimization methods of network reconfiguration and reactive power compensation were explored, models for wind turbine output and photovoltaic power plants were developed, and intelligent algorithms capable of solving complex multi-objective, multi-variable, non-linear optimization problems were formulated. Through example analysis, the effectiveness of these algorithms, models, and time division methods was demonstrated, also considering the integration of energy storage units to assist in electricity generation and grid connection. The key results and conclusions from this investigation are as follows:

(1) Development of the MOFSA Algorithm: A Mixed-Strategy-Based Multi-Objective Firefly Search Algorithm (MOFSA) was introduced to overcome the limitations of conventional firefly algorithms, particularly in multi-objective optimization. This algorithm was enhanced to improve solution distribution, facilitate escape from local optima, increase population diversity, and strengthen search capability through strategic improvements such as third-order chaotic mapping, Cauchy variation, stochastic perturbation, and a nonlinearly decreasing population proportion factor. It incorporated a non-dominated ordering mechanism and an external archiving mechanism for effective multi-objective optimization.

(2) Performance Evaluation of the MOFSA Algorithm: The MOFSA algorithm was validated against other multi-objective optimization algorithms across six test functions, displaying superior hypervolume indexes of 0.662, 0.329, 0.526, 0.323, 0.386, and 0.225. This performance has illustrated its exceptional capability in generating solutions with broader and more uniform distribution, indicating its advancement and effectiveness.

(3) Improvements in System Performance: The application of the MOFSA algorithm to a static integrated optimization model, which has combined network reconfiguration and reactive power compensation, resulted in significant advancements. The generated Pareto front was more comprehensive and uniformly distributed, achieving reductions in power loss and node voltage deviation by up to 3.6% and 22.7%, respectively. Through specific scenario analysis, the model demonstrated its efficacy by significantly reducing economic cost (11.39%), power loss (60.68%), and voltage deviation (62.29%) compared to baseline measures.

(4) Dynamic Optimization Model Advancements: The extension to a dynamic optimization model that has included time slot divisions was made, and the MOFSA algorithm proved to be highly competitive, reducing the system's economic cost and power loss by up to 6.15% and 11.6%, respectively. When compared to methods employing only dynamic reconfiguration or reactive power compensation, the integrated approach achieved greater reductions in economic cost, voltage deviation, and power loss by 37.64%, 50.04%, and 70.73%, respectively. The introduction of a time slot division method significantly reduced the number of switching operations by 78.72%, from 94 to 20.

The findings from this thesis affirmed the potential and effectiveness of the proposed optimization methods for enhancing the operation of power systems with distributed power sources. The research highlighted substantial improvements in system operations, economic efficiency, and energy utilization, offering robust evidence and insights for the development of future optimization strategies in economic power distribution power networks, thereby contributing valuable solutions to the existing challenges.

7.2 Innovation Points

Several innovative contributions to the field of distributed power systems were introduced in this thesis, focusing on optimizing their integration and management through advanced modeling and algorithmic solutions. The key innovations are as follows:

(1) Development of the MOFSA Algorithm: The limitations of traditional firefly search algorithms, particularly their insufficient search capability and inability to handle multi-objective optimization, were addressed. A Multi-Objective Firefly Search Algorithm (MOFSA) employing a hybrid strategy was proposed to tackle the complex optimization challenges inherent in distributed power systems.

(2) Static Comprehensive Optimization Model: A new model for the static comprehensive optimization of distributed power systems was developed. The MOFSA algorithm was applied to this model to identify optimal compromise solutions using the ideal solution similarity ranking technique. The effectiveness of both the algorithm and the model was validated through empirical testing, showcasing improvements in system performance.

(3) Dynamic Comprehensive Optimization Model: A dynamic comprehensive optimization model was established, building upon the static model and incorporating dynamic reconfiguration and reactive power compensation. This model took into

account the practical constraints of switching actions and the interplay between different time sections, offering a more nuanced approach to system optimization.

These innovations collectively contributed to the advancement of distributed power system optimization, providing new tools and strategies for improving the integration, management, and performance of these systems.

7.3 Outlook

This thesis presented the distributed power system as the research object and conducted research from the perspectives of model construction and algorithmic solutions, leading to the operation optimization of the distributed power system. The research aimed to improve the economic efficiency, energy efficiency, and power quality of the power system. However, there are still identified deficiencies that necessitate further research and improvement, as detailed below:

(1) The static and dynamic integrated optimization models developed in this thesis were primarily intended for the grid connection of photovoltaic and wind power. It was acknowledged that the potential for grid connection of other types of renewable energy generation may be considered in future research.

(2) The multi-objective firefly algorithm based on a hybrid strategy, proposed in this thesis, was recognized for its strong problem-solving capabilities. However, it was suggested that further improvements could enhance the convergence accuracy and solving efficiency of the algorithm, enabling it to address more complex power system optimization models.

(3) In this thesis, the study of power system operation optimization was carried out under the condition of predetermined power output from distributed power sources. It was proposed that the next step could involve considering the stochastic nature of the power output of distributed power sources to improve the model's applicability.

References

[1] D. Zhang, G. M. Shafiullah, C. K. Das, and K. Wai, "A systematic review of optimal planning and deployment of distributed generation and energy storage systems in power networks," *J. Energy Storage*, vol. 56, no. PA, p. 105937, 2022.

[2] A. Alzahrani *et al.*, "Multi-Objective Energy Optimization with Load and Distributed Energy Source Scheduling in the Smart Power Grid," *Sustain.*, vol. 15, no. 13, pp. 1–21, 2023.

[3] S. Singh and A. Kumar, "Economic dispatch for multi heat-electric energy source based microgrid," *PIICON 2020 - 9th IEEE Power India Int. Conf.*, 2020.

[4] D. Xia, "Day-ahead Optimal Scheduling of Power System Considering Uncertainty of New Energy and Load," *Asia-Pacific Power Energy Eng. Conf. APPEEC*, vol. 2020-Septe, pp. 1–6, 2020.

[5] M. Wolsink, "Distributed energy systems as common goods: Socio-political acceptance of renewables in intelligent microgrids," *Renew. Sustain. Energy Rev.*, vol. 127, no. April, p. 109841, 2020.

[6] S. O. Muhanji, A. Muzhikyan, and A. M. Farid, "Distributed Control for Distributed Energy Resources: Long-Term Challenges and Lessons Learned," *IEEE Access*, vol. 6, pp. 32737–32753, 2018.

[7] I. Marouani *et al.*, "Integration of Renewable-Energy-Based Green Hydrogen into the Energy Future," *Processes*, vol. 11, no. 9, 2023.

[8] K. Potter, J. Oloyede, and H. Klaus, "Renewable Energy: A Catalyst for Sustainable Development and Climate Resilience," *Energy Sources*, no. December, 2023.

[9] J. Li, M. S. Herdem, J. Nathwani, and J. Z. Wen, "Methods and applications for Artificial Intelligence, Big Data, Internet of Things, and Blockchain in smart energy management," *Energy AI*, vol. 11, no. October 2022, p. 100208, 2023.

[10] M. Laimon and T. Yusaf, "Towards energy freedom: Exploring sustainable solutions for energy independence and self-sufficiency using integrated renewable energy-driven hydrogen system," *Renew. Energy*, vol. 222, no. January, p. 119948, 2024.

[11] X. Ma, C. Liang, X. Dong, and Y. Li, "Multi-objective reactive power optimization strategy of power system considering large-scale renewable integration," *Front. Energy Res.*, vol. 11, no. June, pp. 1–10, 2023.

[12] N. Kefif, B. Melzi, M. Hashemian, M. E. H. Assad, and S. Hoseinzadeh, "Feasibility and optimal operation of micro energy hybrid system (hydro/wind) in the rural valley region," *Int. J. Low-Carbon Technol.*, vol. 17, pp. 58–68, 2022.

[13] A. M. Nassef, M. A. Abdelkareem, H. M. Maghrabie, and A. Baroutaji, "Review of Metaheuristic Optimization Algorithms for Power Systems Problems," *Sustain.*, vol. 15, no. 12, pp. 1–27, 2023.

[14] N. U. I. Hossain, S. A. Fazio, J. M. Lawrence, E. D. Santibanez Gonzalez, R. Jaradat, and M. S. Alvarado, "Role of systems engineering attributes in enhancing supply chain resilience: Healthcare in context of COVID-19 pandemic," *Heliyon*, vol. 8, no. 6, p. e09592, 2022.

[15] D. Razmi, T. Lu, B. Papari, E. Akbari, G. Fathi, and M. Ghadamyari, "An Overview on

Power Quality Issues and Control Strategies for Distribution Networks With the Presence of Distributed Generation Resources," *IEEE Access*, vol. 11, no. February, pp. 10308–10325, 2023.

[16] J. Andruszkiewicz, J. Lorenc, and A. Weychan, "Determination of the Optimal Level of Reactive Power Compensation That Minimizes the Costs of Losses in Distribution Networks," *Energies*, vol. 17, no. 1, 2024.

[17] U. Pandey, A. Pathak, A. Kumar, and S. Mondal, "Applications of artificial intelligence in power system operation, control and planning: a review," *Clean Energy*, vol. 7, no. 6, pp. 1199–1218, 2023.

[18] A. K. Ozcanli, F. Yaprakdal, and M. Baysal, "Deep learning methods and applications for electrical power systems: A comprehensive review," *Int. J. Energy Res.*, vol. 44, no. 9, pp. 7136–7157, 2020.

[19] N. Hosseinzadeh, A. Aziz, A. Mahmud, A. Gargoom, and M. Rabbani, "Voltage stability of power systems with renewable-energy inverter-based generators: A review," *Electron.*, vol. 10, no. 2, pp. 1–27, 2021.

[20] C. Hou, C. Zhang, P. Wang, and S. Liu, "Renewable energy based low-voltage distribution network for dynamic voltage regulation," *Results Eng.*, vol. 21, no. September 2023, p. 101701, 2024.

[21] P. Veers *et al.*, "Grand challenges in the design , manufacture , and operation of future wind turbine systems," pp. 1071–1131, 2023.

[22] T. Ibn-mohammed, S. C. L. Koh, I. M. Reaney, A. Acquaye, G. Schileo, and K. B. Mustapha, "Perovskite solar cells : An integrated hybrid lifecycle assessment and review in comparison with other photovoltaic technologies," *Renew. Sustain. Energy Rev.*, vol. 80, no. November 2015, pp. 1321–1344, 2017.

[23] N. E. Benti, M. D. Chaka, and A. G. Semie, "Forecasting Renewable Energy Generation with Machine Learning and Deep Learning: Current Advances and Future Prospects," *Sustain.*, vol. 15, no. 9, May 2023.

[24] O. Kahouli, H. Alsaif, Y. Bouteraa, N. Ben Ali, and M. Chaabene, "Power system reconfiguration in distribution network for improving reliability using genetic algorithm and particle swarm optimization," *Appl. Sci.*, vol. 11, no. 7, 2021, doi: 10.3390/app11073092.

[25] C. Biswal, B. K. Sahu, M. Mishra, and P. K. Rout, "Real-Time Grid Monitoring and Protection: A Comprehensive Survey on the Advantages of Phasor Measurement Units," *Energies*, vol. 16, no. 10, 2023.

[26] M. J. Lawal, S. U. Hussein, B. Saka, S. U. Abubakar, and I. S. Attah, "Intelligent fuzzy-based automatic voltage regulator with hybrid optimization learning method," *Sci. African*, vol. 19, p. e01573, 2023.

[27] A. A. Al-shamma, H. M. H. Farh, A. M. Noman, A. M. Al-shaalan, and A. Alkuhayli, "Optimal Sizing of a Hybrid Renewable Photovoltaic-Wind System-Based Microgrid Using Harris Hawk Optimizer," vol. 2022, 2022.

[28] S. Hoseinzadeh, M. Hadi Zakeri, A. Shirkhani, and A. J. Chamkha, "Analysis of energy consumption improvements of a zero-energy building in a humid mountainous area," *J. Renew. Sustain. Energy*, vol. 11, no. 1, 2019.

[29] Z. Liu, Y. Lu, J. Kong, J. Gong, and S. Wang, “Multimodal fault-tolerant control for single-phase cascaded off-grid PV-storage system with PV failure using hybrid modulation,” *Microelectron. Reliab.*, vol. 114, Nov. 2020.

[30] K. R. Khalilpour *et al.*, “Design and economics analysis of an off-grid PV system for household electrification,” *Renew. Sustain. Energy Rev.*, vol. 12, no. 1, pp. 1–11, 2020.

[31] International Renewable Energy Agency (IRENA), *Future of solar photovoltaic: Deployment, investment, technology, grid integration and socio-economic aspects*, vol. November. 2019. [Online]. Available: https://www.irena.org/-/media/Files/IRENA/Agency/Publication/2019/Oct/IRENA_Future_of_wind_2019.pdf

[32] M. Upasani *et al.*, “Simulation and performance analysis of a 1kWp photovoltaic system using PVsyst,” *Sol. Energy*, vol. 24, no. 3, pp. 177–184, 2018.

[33] J. Yates *et al.*, “Techno-economic Analysis of Hydrogen Electrolysis from Off-Grid Stand-Alone Photovoltaics Incorporating Uncertainty Analysis,” *Cell Reports Phys. Sci.*, vol. 1, no. 10, p. 100209, 2020.

[34] Q. Hassan, S. Algburi, A. Z. Sameen, H. M. Salman, and M. Jaszczur, “A review of hybrid renewable energy systems: Solar and wind-powered solutions: Challenges, opportunities, and policy implications,” *Results Eng.*, vol. 20, no. September, p. 101621, 2023.

[35] P. Wei *et al.*, “Progress in Energy Storage Technologies and Methods for Renewable Energy Systems Application,” *Appl. Sci.*, vol. 13, no. 9, 2023.

[36] M. I. Mosaad, H. S. M. Ramadan, M. Aljohani, M. F. El-Naggar, and S. S. M. Ghoneim, “Near-Optimal PI Controllers of STATCOM for Efficient Hybrid Renewable Power System,” *IEEE Access*, vol. 9, pp. 34119–34130, 2021.

[37] I. Visa, B. Burduhos, M. Neagoe, M. Moldovan, and A. Duta, “Comparative analysis of the infield response of five types of photovoltaic modules,” *Renew. Energy*, vol. 95, pp. 178–190, 2016.

[38] V. S. B. Kurukuru, A. Haque, M. A. Khan, S. Sahoo, A. Malik, and F. Blaabjerg, “A review on artificial intelligence applications for grid-connected solar photovoltaic systems,” *Energies*, vol. 14, no. 15, pp. 1–35, 2021.

[39] D. T. Cotfas, P. A. Cotfas, and O. M. Machidon, “Study of temperature coefficients for parameters of photovoltaic cells,” *Int. J. Photoenergy*, vol. 2018, p. 12, 2018.

[40] M. Chennaif, H. Zahboune, M. Elhafyani, and S. Zouggar, “Electric System Cascade Extended Analysis for optimal sizing of an autonomous hybrid CSP / PV / wind system with Battery Energy Storage System and thermal energy storage,” *Energy*, vol. 227, p. 120444, 2021.

[41] A. F. M. Nor, S. Salimin, M. N. Abdullah, and M. N. Ismail, “Application of artificial neural network in sizing a stand-alone photovoltaic system: A review,” *Int. J. Power Electron. Drive Syst.*, vol. 11, no. 1, pp. 342–349, 2020.

[42] A. N. Sheta, G. M. Abdulsalam, B. E. Sedhom, and A. A. Eladl, *Comparative framework for AC-microgrid protection schemes: challenges, solutions, real applications, and future trends*, vol. 8, no. 1. Springer Nature Singapore, 2023.

[43] A. S. C. Imene Yahyaoui, *Advances in Renewables Energies and power technologies*. Elsevier Inc., 2018.

[44] A. R. Sudhamshu, M. C. Pandey, N. Sunil, N. S. Satish, V. Mugundhan, and R. K. Velamati, “Numerical study of effect of pitch angle on performance characteristics of a HAWT,” *Eng. Sci. Technol. an Int. J.*, vol. 19, no. 1, pp. 632–641, 2016, doi: 10.1016/j.jestch.2015.09.010.

[45] P. Coelho, “The Betz limit and the corresponding thermodynamic limit,” *Wind Eng.*, vol. 47, no. 2, pp. 491–496, 2023.

[46] C. Zhao and X. Li, “A Novel Real-Time Energy Management Strategy for Grid-Supporting Microgrid: Enabling Flexible Trading Power,” *IEEE Power Energy Soc. Gen. Meet.*, vol. 2021-July, pp. 1–5, 2021.

[47] J.F. Manwell ;J.G MCGowan;A.L.Rogers, *Wind Energy Explained.Theory,design,and Application.Second edition*, Second edi. 2009.

[48] P. Jiang, H. Yang, and J. Heng, “A hybrid forecasting system based on fuzzy time series and multi-objective optimization for wind speed forecasting,” *Appl. Energy*, vol. 235, pp. 786–801, Feb. 2019.

[49] X. Li, J. Zhang, D. Zhou, G. Zhang, and H. Wu, “Structural Optimization and Thermal Management with PCM- Honeycomb Combination for Photovoltaic-Battery Integrated System,” vol. 2022, 2022.

[50] B. Xu *et al.*, “Reactive power optimization of a distribution network with high-penetration of wind and solar renewable energy and electric vehicles,” *Prot. Control Mod. Power Syst.*, vol. 7, no. 1, pp. 1–13, 2022.

[51] M. R. Patel, *Wind and Solar Power Systems:Design,Analysis,and operation*, Second. NW: Taylor& Francis Group, 2006.

[52] Prof.Dr.Manfred stiebler, *Wind energy systems for electric power generation*, vol. 01. Springer Science & Business Media, 2008.

[53] M. Blackwood, “Maximum Efficiency of a Wind Turbine,” *Undergrad. J. Math. Model. One + Two Vol. 6 Iss. 2, Artic. 2*, vol. 6, no. 2, 2016, [Online]. Available: https://digitalcommons.usf.edu/ujmm/vol6/iss2/2

[54] G. Huleihil, M., & Mazor, “Wind turbine power: The betz limit and beyond.,” *Adv. Wind power. IntechOpen*, vol. 11, p. 13, 2012, [Online]. Available: https://www.intechopen.com/books/advanced-biometric-technologies/liveness-detection-in-biometrics

[55] Nur Hasanah, “Wind Turbine Power Calculations RWE npower renewables,” 2015. [Online]. Available: https://www.studocu.com/row/document/mbeya-university-of-science-and-technology/fluid-power-and-control/23-wind-turbine-lecture-notes-1/6019877

[56] R. Chedid, H. Akiki, and S. Rahman, “A decision support technique for the design of hybrid solar-wind power systems,” *IEEE Trans. Energy Convers.*, vol. 13, no. 1, pp. 76–83, 1998.

[57] Vinod, R. Kumar, and S. K. Singh, “Solar photovoltaic modeling and simulation: As a renewable energy solution,” *Energy Reports*, vol. 4, pp. 701–712, 2018.

[58] T. Ma, W. Gu, L. Shen, and M. Li, “An improved and comprehensive mathematical model for solar photovoltaic modules under real operating conditions,” *Sol. Energy*, vol. 184, no. December 2018, pp. 292–304, 2019.

[59] N. Chatterji, A. Antony, and P. R. Nair, “Temperature coefficient of Silicon based carrier selective solar cells,” *IEEE J. Photovoltaics 9.3 583-590.*, vol. 9, no. 3, pp. 583–590, 2019.

[60] H. A. Ramadan, B. Khan, and A. A. Z. Diab, “Accurate Parameters Estimation of Three

Diode Model of Photovoltaic Modules Using Hunter-Prey and Wild Horse Optimizers," *IEEE Access*, vol. 10, no. July, pp. 87435–87453, 2022.

[61] A. Luque and S. Hegedus, *Handbook of Photovoltaic Science and Engineering*. John Wiley& Sons, 2011. [Online]. Available: books.google.com

[62] K. Hachimy *et al.*, "Tie open point relocation as possible replacement for the step voltage regulator nets," pp. 3–8, 2023.

[63] L. Zheng *et al.*, "Solid-State Transformer and Hybrid Transformer With Integrated Energy Storage in Active Distribution Grids: Technical and Economic Comparison, Dispatch, and Control," *IEEE J. Emerg. Sel. Top. Power Electron.*, vol. 10, no. 4, pp. 3771–3787, 2022.

[64] V. Saxena, N. Kumar, and U. Nangia, "Impact Analysis of Demand Response on the Optimal Placement of Solar PV Systems in the Distribution Network," *Brazilian Arch. Biol. Technol.*, vol. 67, 2024, doi: 10.1590/1678-4324-2024230419.

[65] E. Zulu, "Estimation of Hosting Capacity of Photovoltaic Generations in Distribution Networks using Hybrid Particle Swarm and Gradient Descent Optimization.".

[66] X. S. Yang, "Firefly algorithms for multimodal optimization," *Lect. Notes Comput. Sci. (including Subser. Lect. Notes Artif. Intell. Lect. Notes Bioinformatics)*, vol. 5792 LNCS, pp. 169–178, 2009.

[67] J. L. Bei, M. X. Zhang, J. Q. Wang, H. H. Song, and H. Y. Zhang, "Improved Hybrid Firefly Algorithm with Probability Attraction Model," *Mathematics*, vol. 11, no. 2, Jan. 2023.

[68] L. Almuqren, H. Alqahtani, S. S. Aljameel, A. S. Salama, I. Yaseen, and A. A. Alneil, "Hybrid Metaheuristics With Machine Learning Based Botnet Detection in Cloud Assisted Internet of Things Environment," *IEEE Access*, vol. 11, pp. 115668–115676, 2023.

[69] A. Akter *et al.*, "A review on microgrid optimization with meta-heuristic techniques: Scopes, trends and recommendation," *Energy Strateg. Rev.*, vol. 51, no. January, 2024.

[70] H. M. Hussein Farh, "Neural Network Algorithm with Reinforcement Learning for Microgrid Techno-Economic Optimization," *Mathematics*, vol. 12, no. 2, 2024.

[71] W. Li *et al.*, "Firefly Algorithm-Based Semi-Supervised Learning with Transformer Method for Shore Power Load Forecasting," *IEEE Access*, vol. 11, pp. 77359–77370, 2023.

[72] K. Nagarajan, A. Rajagopalan, M. Bajaj, R. Sitharthan, S. A. Dost Mohammadi, and V. Blazek, "Optimizing dynamic economic dispatch through an enhanced Cheetah-inspired algorithm for integrated renewable energy and demand-side management," *Sci. Rep.*, vol. 14, no. 1, pp. 1–22, 2024.

[73] K. Gholami, M. Abbasi, A. Azizivahed, and L. Li, "An efficient bi-objective approach for dynamic economic emission dispatch of renewable-integrated microgrids," *J. Ambient Intell. Humaniz. Comput.*, vol. 14, no. 8, pp. 10695–10714, 2023.

[74] Y. Tian, X. Zhang, R. Cheng, and Y. Jin, "A multi-objective evolutionary algorithm based on an enhanced inverted generational distance metric," *2016 IEEE Congr. Evol. Comput. CEC 2016*, pp. 5222–5229, 2016.

[75] X. Cai, Y. Xiao, M. Li, H. Hu, H. Ishibuchi, and X. Li, "A Grid-Based Inverted Generational Distance for Multi/Many-Objective Optimization," *IEEE Trans. Evol. Comput.*, vol. 25, no. 1, pp. 21–34, 2021.

[76] H. Ishibuchi, H. Masuda, Y. Tanigaki, and Y. Nojima, “Difficulties in specifying reference points to calculate the inverted generational distance for many-objective optimization problems,” *IEEE SSCI 2014 - 2014 IEEE Symp. Ser. Comput. Intell. - MCDM 2014 2014 IEEE Symp. Comput. Intell. Multi-Criteria Decis. Proc.*, pp. 170–177, 2015.

[77] H. Ishibuchi, R. Imada, Y. Setoguchi, and Y. Nojima, “Reference Point Specification in Inverted Generational Distance for Triangular Linear Pareto Front,” *IEEE Trans. Evol. Comput.*, vol. 22, no. 6, pp. 961–975, 2018.

[78] H. Ishibuchi, H. Masuda, and Y. Nojima, “Sensitivity of performance evaluation results by inverted generational distance to reference points,” *2016 IEEE Congr. Evol. Comput. CEC 2016*, vol. 1, pp. 1107–1114, 2016.

[79] O. Schütze, X. Esquivel, A. Lara, and C. A. C. Coello, “Using the averaged hausdorff distance as a performance measure in evolutionary multiobjective optimization,” *IEEE Trans. Evol. Comput.*, vol. 16, no. 4, pp. 504–522, 2012.

[80] M. Khubroo and S. J. Mousavirad, “A levy flight-based decomposition multi-objective optimization based on grey Wolf optimizer,” *2019 9th Int. Conf. Comput. Knowl. Eng. ICCKE 2019*, no. Iccke, pp. 155–161, 2019.

[81] C. M. Fonseca, L. Paquete, and M. López-Ibáñez, “An improved dimension-sweep algorithm for the hypervolume indicator,” *2006 IEEE Congr. Evol. Comput. CEC 2006*, pp. 1157–1163, 2006.

[82] G. Acciarini, D. Izzo, and E. Mooij, “MHACO: A Multi-Objective Hypervolume-Based Ant Colony Optimizer for Space Trajectory Optimization,” *2020 IEEE Congr. Evol. Comput. CEC 2020 - Conf. Proc.*, 2020.

[83] S. Feng and J. Wen, “An Evolutionary Many-Objective Optimization Algorithm Based on IGD Indicator and Region Decomposition,” *Proc. - 2019 15th Int. Conf. Comput. Intell. Secur. CIS 2019*, pp. 206–210, 2019.

[84] J. J. Liang, C. T. Yue, and B. Y. Qu, “Multimodal multi-objective optimization: A preliminary study,” *2016 IEEE Congr. Evol. Comput. CEC 2016*, pp. 2454–2461, 2016.

[85] A. B. Kalita, S. C. Rajbongshi, and G. Trivedi, “Hybrid multi-objective constrained optimization based on feasibility segregation, non-dominated sorting and crowding distance,” *Proc. 10th Int. Conf. Signal Process. Integr. Networks, SPIN 2023*, pp. 7–13, 2023.

[86] V. Zhelezniak, A. Savkov, A. Shen, and N. Y. Hammerla, “Correlation Coefficients and Semantic Textual Similarity,” 2019, p. 12. [Online]. Available: http://arxiv.org/abs/1905.07790

[87] M. B. Altman, W. Wan, A. S. Hosseini, S. Arabi Nowdeh, and M. Alizadeh, “Machine learning algorithms for FPGA Implementation in biomedical engineering applications: A review,” *Heliyon*, vol. 10, no. 4, p. e26652, 2024.

[88] S. Yang, H. C. Chen, C. H. Wu, M. N. Wu, and C. H. Yang, “Forecasting of the prevalence of dementia using the lstm neural network in Taiwan,” *Mathematics*, vol. 9, no. 5, pp. 1–19, Mar. 2021.

[89] C. Nsengimana, “Short-term Photovoltaic Power Forecasting Based on Improved Firefly Algorithm to optimize support vector machine,” pp. 2020–2022, 2020.

[90] A. S. DKASC, “dka solar centre.” [Online]. Available: https://dkasolarcentre.com.au/locations/alice-springs

[91] N. Effenberger and N. Ludwig, “A collection and categorization of open-source wind and wind power datasets,” *Wind Energy*. John Wiley and Sons Ltd, 2022. doi: 10.1002/we.2766.

[92] E. S. Miele, N. Ludwig, and A. Corsini, “Multi-Horizon Wind Power Forecasting Using Multi-Modal Spatio-Temporal Neural Networks,” *Energies*, vol. 16, no. 8, Apr. 2023.

[93] Z. Liu, P. Jiang, L. Zhang, and X. Niu, “A combined forecasting model for time series: Application to short-term wind speed forecasting,” *Appl. Energy*, vol. 259, p. 25, Feb. 2020.

[94] J. M. González-Sopeña, V. Pakrashi, and B. Ghosh, “An overview of performance evaluation metrics for short-term statistical wind power forecasting,” *Renew. Sustain. Energy Rev.*, vol. 138, Mar. 2021.

[95] Y. Wang, R. Zou, F. Liu, L. Zhang, and Q. Liu, “A review of wind speed and wind power forecasting with deep neural networks,” *Appl. Energy*, vol. 304, Dec. 2021.

[96] R. Ahmed, V. Sreeram, Y. Mishra, and M. D. Arif, “A review and evaluation of the state-of-the-art in PV solar power forecasting: Techniques and optimization,” *Renewable and Sustainable Energy Reviews*, vol. 124. Elsevier Ltd, May 01, 2020.

[97] K. A. Kader, M. A. Mannan, and M. R. Hazari, “Impacts of GA and PSO on Loss Minimization in Distribution Networks with DG Incorporation: A Comparative Study,” *2023 Int. Conf. Network, Multimed. Inf. Technol. NMITCON 2023*, pp. 1–6, 2023.

[98] C. Voyant *et al.*, “Machine learning methods for solar radiation forecasting : A review,” *Renew. Energy*, vol. 105, pp. 569–582, 2017.

[99] H. Sheng, J. Xiao, Y. Cheng, Q. Ni, and S. Wang, “Short-Term Solar Power Forecasting Based on Weighted Gaussian Process Regression,” *IEEE Trans. Ind. Electron.*, vol. 65, no. 1, pp. 300–308, 2018.

[100] I. Algaddafi, A., Alshahrani, J., Hussain, S., Elnaddab, K., Diryak, E., & Daho, “Comparing the Impact of the Off-Grid System and on-Grid System on a Realistic Load.,” in *In Proceedings of the 32nd European Photovoltaic Solar Energy Conference and Exhibition, Munich, Germany (pp. 20-24).*, Munich, pp. 20–24.

[101] IRENA, “solar energy.” Accessed: Apr. 05, 2022. [Online]. Available: https://www.irena.org/solar

[102] Z. F. Liu, S. F. Luo, M. L. Tseng, H. M. Liu, L. Li, and A. Hashan Md Mashud, “Short-term photovoltaic power prediction on modal reconstruction: A novel hybrid model approach,” *Sustain. Energy Technol. Assessments*, vol. 45, Jun. 2021.

[103] A. Kwangkaew, S. Skolthanarat, C. Charoenlarpnopparut, and M. Kaneko, “Optimal Location and Sizing of Renewable Distributed Generators for Improving Robust Voltage Stability Against Uncontrollable Reactive Compensation,” *IEEE Access*, vol. 11, no. June, pp. 52260–52274, 2023.

[104] F. E. Inyanga, I. N. Muisyo, and K. K. Kaberere, “Static Transmission Network Expansion Planning Considering Voltage Limits,” *IEEE AFRICON Conf.*, pp. 1–6, 2023.

[105] B. Ismail, N. I. Abdul Wahab, M. L. Othman, M. A. M. Radzi, K. Naidu Vijyakumar, and M. N. Mat Naain, “A Comprehensive Review on Optimal Location and Sizing of Reactive Power Compensation Using Hybrid-Based Approaches for Power Loss Reduction, Voltage Stability Improvement, Voltage Profile Enhancement and Loadability Enhancement,” *IEEE Access*, vol. 8, pp. 222733–222765, 2020.

[106] S. Xue *et al.*, “Collaborative Optimization Allocation of Grid-Forming and Grid-Following Reactive Power Resources Considering Auxiliary Equipment Services,” *IEEE Access*, vol. 11, no. September, pp. 95840–95857, 2023.

[107] S. Yuan, L. Tao, S. Sun, J. Xing, Y. Cheng, and S. Xia, “A Comprehensive Reactive Power Optimization Model for Distribution Grid with Renewables,” *2023 IEEE Int. Conf. Energy Technol. Futur. Grids*, pp. 1–6, 2024.

[108] M. A. Iqbal and R. Zafar, “A Novel Radiality Maintenance Algorithm for the Metaheuristic Based Co-Optimization of Network Reconfiguration with Battery Storage,” *IEEE Access*, vol. 11, no. February, pp. 25689–25701, 2023.

[109] S. Chakraborty, S. Mukhopadhyay, and S. K. Biswas, “Optimal Placement of PV-DSTATCOM Based EV Charging Stations with Dynamic Pricing,” *IEEE Trans. Ind. Appl.*, vol. 59, no. 6, pp. 7092–7102, 2023.

[110] L. Alhmoud and W. Marji, “Optimization of Three-Phase Feeder Load Balancing Using Smart Meters,” *IEEE Can. J. Electr. Comput. Eng.*, vol. 45, no. 1, pp. 9–17, 2022.

[111] S. Gupta, V. K. Yadav, and M. Singh, “Optimal Allocation of Capacitors in Radial Distribution Networks Using Shannon’s Entropy,” *IEEE Trans. Power Deliv.*, vol. 37, no. 3, pp. 2245–2255, 2022.

[112] M. S. Ghole, A. Tiwari, N. Thakkar, P. Paliwal, T. Thakur, and A. Arya, “Optimal Placement of Distributed Generator using BFPSO,” *2nd Odisha Int. Conf. Electr. Power Eng. Commun. Comput. Technol. ODICON 2022*, pp. 1–6, 2022.

[113] W. Huang and C. Zhao, “Deep-Learning-Aided Voltage-Stability-Enhancing Stochastic Distribution Network Reconfiguration,” *IEEE Trans. Power Syst.*, vol. 39, no. 1, pp. 2827–2836, 2023.

[114] S. Paul and N. P. Padhy, “Real-Time Advanced Energy-Efficient Management of an Active Radial Distribution Network,” *IEEE Syst. J.*, vol. 16, no. 3, pp. 3602–3612, 2022.

[115] B. Pournazarian, R. Sangrody, M. Saeedian, O. Gomis-Bellmunt, and E. Pouresmaeil, “Enhancing Microgrid Small-Signal Stability and Reactive Power Sharing Using ANFIS-Tuned Virtual Inductances,” *IEEE Access*, vol. 9, pp. 104915–104926, 2021.

[116] Y. Li and Y. Li, “Security-Constrained Multi-Objective Optimal Power Flow for a Hybrid AC/VSC-MTDC System with Lasso-Based Contingency Filtering,” *IEEE Access*, vol. 8, pp. 6801–6811, 2020.

[117] I. A. Smadi and L. I. Shehadeh, “An Improved Reactive Power Sharing in an Isolated Microgrid with a Local Load Detection,” *Chinese J. Electr. Eng.*, vol. 9, no. 2, pp. 14–26, 2023.

[118] S. R. Shukla, S. Paudyal, and M. R. Almassalkhi, “Efficient Distribution System Optimal Power Flow With Discrete Control of Load Tap Changers,” *IEEE Trans. Power Syst.*, vol. 34, no. 4, pp. 2970–2979, 2019.

[119] G. A. Orcajo, J. R. Diez, J. M. Cano, J. G. Norniella, J. F. Pedrayes Gonzalez, and C. H. Rojas, “Coordinated Management of Electrical Energy in a Steelworks and a Wind Farm,” *IEEE Trans. Ind. Appl.*, vol. 58, no. 4, pp. 5488–5502, 2022.

[120] V. Vijayan, A. Mohapatra, S. N. Singh, and C. L. Dewangan, “An Efficient Modular Optimization Scheme for Unbalanced Active Distribution Networks with Uncertain EV and PV Penetrations,” *IEEE Trans. Smart Grid*, vol. 14, no. 5, pp. 3876–3888, 2023.

[121] V. Vijayan, A. Mohapatra, S. N. Singh, and A. Tiwari, “A Blended Approach to Improve Reliability and Efficiency of Active EDN via Dynamic Feeder Reconfiguration, Demand Response, and VVO,” *IEEE Trans. Autom. Sci. Eng.*, vol. 21, no. 1, pp. 684–695, 2024.

[122] Z. Cheng, L. Wang, S. Zeng, C. Su, R. Zhang, and W. Zhou, “Partition-Global Dual-Layer Collaborative Voltage Control Strategy for Active Distribution Network With High Proportion of Renewable Energy,” *IEEE Access*, vol. 12, no. January, pp. 22546–22556, 2024.

[123] H. Singh, Y. Sawle, S. Dixit, H. Malik, and F. P. García Márquez, “Optimization of reactive power using dragonfly algorithm in DG integrated distribution system,” *Electr. Power Syst. Res.*, vol. 220, no. January, 2023.

[124] N. Nacar Cikan and M. Cikan, “Reconfiguration of 123-bus unbalanced power distribution network analysis by considering minimization of current & voltage unbalanced indexes and power loss,” *Int. J. Electr. Power Energy Syst.*, vol. 157, no. November 2023, p. 109796, 2024.

[125] C. Li, Y. Dai, P. Wang, and S. Xia, “Active and reactive power coordinated optimization of active distribution networks considering dynamic reconfiguration and SOP,” *IET Renew. Power Gener.*, no. July, pp. 1–12, 2023.

[126] X. Xiao, Y. Zhou, W. Zhang, Y. Wang, Z. Zheng, and W. Hu, “Power disturbance waveform analysis and proactive application in power systems,” *Energy Convers. Econ.*, vol. 4, no. 2, pp. 123–136, 2023.

[127] A. Águila Téllez, G. López, I. Isaac, and J. W. González, “Optimal reactive power compensation in electrical distribution systems with distributed resources. Review,” *Heliyon*, vol. 4, no. 8, 2018.

[128] H. Gao, T. Jin, C. Feng, C. Li, Q. Chen, and C. Kang, “Review of virtual power plant operations: Resource coordination and multidimensional interaction,” *Appl. Energy*, vol. 357, no. November 2023, p. 122284, 2024.

[129] G. Liang, Y. Wang, B. Sun, and Z. Zhang, “An Optimization Method for the Distributed Collaborative Operation of Multilateral Entities Considering Dynamic Time-of-Use Electricity Price in Active Distribution Network,” *Energies*, vol. 17, no. 2, 2024.

[130] B. Zhou, Y. Guo, X. Liu, G. Li, P. Gu, and B. Yang, “Optimization strategy of power purchase and sale for electricity retailers in a two-tier market,” *Heliyon*, vol. 10, no. 4, p. e26333, 2024.

[131] S. Chen, W. Hu, and Z. Chen, “Comprehensive Cost Minimization in Distribution Networks Using Segmented-Time Feeder Reconfiguration and Reactive Power Control of Distributed Generators,” *IEEE Trans. Power Syst.*, vol. 31, no. 2, pp. 983–993, 2016.

[132] R. Song, W. Qin, W. Shi, and X. Xue, “Optimizing Freight Vehicle Routing in Dynamic Time-Varying Networks with Carbon Dioxide Emission Trajectory Analysis,” *Sustainability*, vol. 15, no. 21, p. 15504, 2023.

[133] Y. Latreche, H. R. E. H. Bouchekara, F. Kerrour, K. Naidu, H. Mokhlis, and M. S. Javaid, “Comprehensive review on the optimal integration of distributed generation in distribution systems,” *J. Renew. Sustain. Energy*, vol. 10, no. 5, 2018.

[134] V. Khare and P. Chaturvedi, “Design, control, reliability, economic and energy management of microgrid: A review,” *e-Prime - Adv. Electr. Eng. Electron. Energy*, vol. 5, no. August, p. 100239, 2023.

[135] E. Warberg, A. Miksits, and F. S. Barbosa, “Real-Time Line-Based Room Segmentation and Continuous Euclidean Distance Fields,” 2024, [Online]. Available: http://arxiv.org/abs/2402.05236

[136] S. Dolnicar, B. Grün, and F. Leisch, *The Benefits of Market Segmentation: Understanding It, Doing It, and Making It Useful*. 2018. [Online]. Available: http://www.springer.com/series/10101

[137] H. M. A. Ahmed, M. H. Ahmed, and M. M. A. Salama, “A Linearized Multiobjective Energy Management Framework for Reconfigurable Smart Distribution Systems Considering BESSs,” *IEEE Syst. J.*, vol. 16, no. 1, pp. 1258–1269, 2022.

[138] K. Muthukumar and S. Jayalalitha, “Integrated approach of network reconfiguration with distributed generation and shunt capacitors placement for power loss minimization in radial distribution networks,” *Appl. Soft Comput. J.*, vol. 52, pp. 1262–1284, 2017.

Academic research papers

The following are the related research achievements obtained during the study for the degree.

[1] **Nsengimana C**, Li L, Han X. Comparative analysis of reliable, feasible, and low-cost photovoltaic microgrid for a residential load in Rwanda. International Journal of Photoenergy. Nov 21,2020:1-14. SCI

[2] **Nsengimana C**, Li L, et al. Standalone photovoltaic and battery microgrid design for rural areas. Energy Exploration & Exploitation. Nov, 2022;40(6):1617-33. SCI

[3] **Nsengimana C**., Li L. et al. Short-term Photovoltaic Power Forecasting Based on Improved Firefly Algorithm to optimize support vector machine. In 2020 International Symposium on Computer, Consumer and Control (IS3C) (pp.344-346). IEEE (IE)

[4] Bimenyimana, S., Asemota, G.N.O., Niyonteze, J.D.D., **Nsengimana, C**., Ihirwe, P.J. and Li L. Photovoltaic solar technologies: solution to affordable, sustainable, and reliable energy access for all in Rwanda. International Journal of Photoenergy, 2019, pp.1-29.SCI.

Acknowledgments

I would like to express my heartfelt gratitude to my Professor Lingling Li, for her endeavor support, motivation, and the immense opportunities she provided to me. Her guidance and teaching helped me during my research, and while I was writing for this thesis.

I would also like to extend my sincere gratitude to many people I had the pleasure to work closely with during this research. Among those people, I owe my deepest gratitude to Electrical Engineering professors who worked hard for us to increase the research capacities of the topic of our choice. The discussion we had in the early days of my research helped me a lot in framing my research problem.

This thesis would not have been possible without the support of all the team of School of International Education (SIE) teachers for their healthy, morale, and financial support to me in particular. I am deeply indebted to their support, and for the opportunity, they afforded me to conduct some of my research at Home during the pandemic of Covid-19.

I would also like to extend my sincere thanks to the members of Electrical laboratory for helping me settle in China. The humble scientific contributions made through this thesis would not have been possible without their support.

I would also appreciate the patience and moral support of my wife, Rosemary Mutesi for all the time I was busy with my studies abroad and during the moment of writing my thesis.

Finally, and most importantly, I am extremely grateful to the Chinese people, who, through the Government, sponsored the research conducted in this thesis. 谢谢! China will always have a special place in my heart.

博士学位论文 DOCTORAL DISSERTATION